NAUSIVIOS CHORA

A Journal in Naval Sciences and Technology

PART A
MECHANICAL AND MARINE ENGINEERING

Volume 4/2012

ΝΑΥΣΙΒΙΟΣ ΧΩΡΑ

Περιοδική Έκδοση Ναυτικών Επιστημών

ΜΕΡΟΣ Α
ΕΠΙΣΤΗΜΕΣ ΝΑΥΤΙΚΗΣ ΜΗΧΑΝΟΛΟΓΙΑΣ

Τεύχος 4/2012

«ΝΑΥΣΙΒΙΟΣ ΧΩΡΑ» 2012
Περιοδική Έκδοση Ναυτικών Επιστημών
Σχολή Ναυτικών Δοκίμων,
Τέρμα Χατζηκυριακού, Χατζηκυριάκειο,
Πειραιάς 18539, Ελλάδα
http://nausivios.snd.edu.gr
ΤΗΛ+302104581382/FAX+302104581604
nausivios@snd.edu.gr

"NAUSIVIOS CHORA" 2012
Journal in Naval Sciences and Technology
Hellenic Naval Academy
Hatzikiriakio, 18539 Piraeus, Greece
http://nausivios.snd.edu.gr
Tel +302104581382/fax +302104581604
nausivios@snd.edu.gr

ISSN: 1791-4469

TABLE OF CONTENTS

Χαιρετισμός Διοικητή Σχολής Ναυτικών Δοκίμων

Καλωσορίζουμε το 4ο τεύχος της «Ναυσιβίου Χώρας» που αναδεικνύει το έργο που επιτελείται στη ΣΝΔ όσον αφορά τις Ναυτικές Επιστήμες.

Σήμερα, σε μια εποχή οικονομικών και κοινωνικών προβλημάτων η έκδοση της «Ναυσιβίου Χώρας» σηματοδοτεί την προσπάθεια των καθηγητών της ΣΝΔ και άλλων εκπαιδευτικών ιδρυμάτων να δημιουργήσουν με το έργο τους θετικές προσδοκίες και εμπλουτισμό γνώσεων τόσο στους φοιτούντες στα Ανώτατα Στρατιωτικά Εκπαιδευτικά Ιδρύματα όσο και σε όλες τις Πανεπιστημιακές Σχολές που ασχολούνται με τον κλάδο των Ναυτικών Επιστημών. Στόχος τους είναι να ενημερώσουν και να προβάλλουν νέες μεθόδους και εξελιγμένες τεχνικές βασισμένες σε προσωπικές έρευνες και αναλύσεις, με αποτέλεσμα την καλύτερη εκπαίδευση και επιμόρφωση των νέων επιστημόνων.

Ως εκ τούτου, χαιρετίζω την τέταρτη έκδοση της «Ναυσιβίου Χώρας» με την ευχή να αποτελέσει ένα νέο κίνητρο για την εξέλιξη και την πρόοδο της Ναυτικής Επιστήμης τόσο στην Ελλάδα όσο και στο εξωτερικό.

Υποναύαρχος Ι. Μαΐστρος ΠΝ, Διοικητής ΣΝΔ

Welcome Address by the Commandant of the Hellenic Naval Academy

We welcome the 4th edition of the “Nausivios Chora” which illustrates the work of the Hellenic Naval Academy concerning the Naval Sciences.

Nowadays, at a time of economic and social problems, the edition of the “Nausivios Chora” underlines the effort of the staff of the Hellenic Navy Academy and other Institutes to create with their work positive expectations and knowledge enrichment both to the students of the Higher Military Educational Institutions and to other Universities that are engaged with Naval Sciences. They are targeting to inform and display new methods and sophisticated techniques based on personal research and analysis, in order to educate and train the new scientists.

Therefore, I wellcome the fourth edition of the “Nausivios Chora” with the wish for it to be a motive for the development and progress of the Naval Science not only in Greece but also abroad.

Rear-Admiral I. Maistros HN, Commandant of the Hellenic Naval Academy

International Advisory Committee

Editorial Board

Editor's Note

"Nausivios Chora" is a scientific journal published since 2006 by the Hellenic Naval Academy, the Institution that provides academic and professional training to the future officers of the Hellenic Navy. The faculty members of the Hellenic Naval Academy are devoted to the promotion of research and education on a broad range of scientific disciplines.

"Nausivios Chora" is a biannual, peer-reviewed, open access journal that publishes original articles in areas of scientific research and applications directly or indirectly related to the naval sciences and technology. The scope of the Journal is to provide a basis for the communication and dissemination of scientific results obtained in Hellenic or International academic and research institutions that may present a relevance to the sea element.

"Nausivios Chora" hosts articles belonging to various scientific disciplines and is divided in five parts, namely *Mechanical and Marine Engineering*, *Electrical Engineering and Computer Science*, *Natural Sciences and Mathematics*, *Humanities and Political Sciences* and *Naval Operations*. The present 2012 Edition Issue contains 24 articles.

The International Advisory Committee members and the Body of Reviewers, all acknowledged experts in their field of interests, cover a wide range of scientific disciplines ensuring the integrity of the peer-review process and the academic excellence of the published articles in a way that best represents the aims and scope of the Journal.

Prof Dr Elias Ar Yfantis
Editor in chief

Acknowledgments

I wish to express my special thanks to Dr Antonis Tsapalis for his excellent work as the administrator of the “Nausivios Chora” website.
Special thanks to Dr Evangelia Karagianni for her creative work on the “Nausivios Chora” 2012 Edition.

E.Ar.Yfantis

PART A:

MECHANICAL AND MARINE ENGINEERING

A Comparative Study on the Seakeeping Operability Performance of Naval Combatants

Gregory J.Grigoropoulos[a] and George P.Petropoulos[b]

[a]*National Technical University of Athens, School of Naval Architecture and Marine Engineering, 9 Heroon Polytechniou str.,15773 Zografou, Greece*
[b]*Lieutenant Cdr., Hellenic Navy, Salamis Naval Base, gpetrop71@gmail.com*

Abstract. In this paper the seakeeping operability of three naval combatants, including a well documented design available in the literature, are compared. In order to accomplish this task, a new realistic operability index is proposed. The actual vessels under investigation are of different design philosophy. The designs were compared scaled down at the same length taking into account their original design condition. Their operability is examined at selected areas of the Eastern Mediterranean Sea for four missions, two speeds and three heading angles, taking into account given seakeeping criteria. Wind and Wave Atlas provides the necessary sea statistics. Plots were produced to quantify the operability of each hull form in a specified area at constant heading and speed. On the basis of the most probable ship's course in each area a component of the operability index is calculated. These indices are summed up to derive the overall seakeeping operability of each candidate. The derived results are discussed and conclusions are drawn.

Keywords: Seakeeping, operability, naval vessel, mission, criteria.
PACS: 47.35.Lf, 47.85.Gh, 02.30.Nw, 02.50.Fz, 02.70.Hm

INTRODUCTION

During the last century a lot of computational methods to evaluate the seakeeping performance of ships in confused seas have been developed. Furthermore, criteria were established for the affordable dynamic responses that affect the ship integrity, the cargo (merchant ships), the crew and the passengers. As a reasonable consequence the capability of a ship to operate and accomplish her mission in a given sea environment could be quantified. Operability or operational effectiveness associates this capability with the percentage of time in which a ship does not violate any of imposed criteria (NATO, STANAG 4154, 2000).

To restrict ourselves in naval vessels, this capability is assessed by considering the various dynamic responses that affect the ship, the crew and its mission. The responses encompass both the basic ones (mainly heave, pitch and roll) and the derived ones, i.e. vertical and lateral velocities and accelerations along the vessel, as well as random events (slamming, deck wetness, propeller racing etc) at specific positions.

The seakeeping performance of a vessel is mainly affected by its size and its hull form geometrical parameters (main dimensions, block coefficient, prismatic coefficient, waterplane area coefficient, longitudinal and vertical location of the centre of buoyancy, longitudinal position

of the center of waterplane area). It is essential to consider the same size when we compare alternative designs, that are expected to operate in the same areas. In this work the length of the vessel was considered as a size indicator. On the other hand, it is clear that the seakeeping operability should be examined in the preliminary ship design stage (Grigoropoulos, 2004), in order the designer to be able to take any necessary measures to improve it, in case some targets or specifications are not fulfilled. In general, the smaller the vessel is, the more sensitive it is in a specific sea environment. Nowadays, the trend is to build versatile, sophisticated and difficult to detect platforms, keeping their size small to reduce the building and maintenance cost, while innovations are also incorporated to improve specific capabilities, such as STEALTH property (VISBY Corvette, LAFAYETTE Frigate, DDG-1000 ZUMWALT Destroyer). In this paper we compare the seakeeping operability of the three candidate hull forms at the frigate size.

OPERABILITY PERFORMANCE ASSESSMENT

Following NATO STANAG 4154 (2000) the seakeeping operability performance of naval ships is assessed in two ways:

- by comparison of the seakeeping performance of a specific design to another reference design with known (good) performance (Figure 1) or to a database of similar ships (Bales, 1980). This method is known as comparative and it is used extensively for hull form optimization for seakeeping (Grigoropoulos and Loukakis, 1990). This method uses quantitative as well as qualitative criteria.

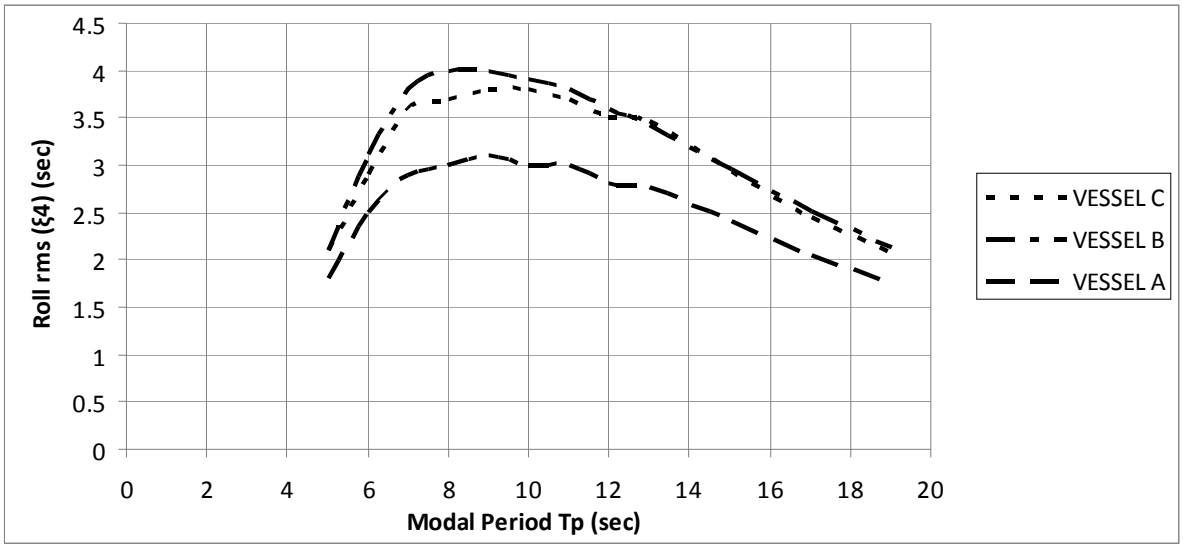

FIGURE 1. Comparative Method of Roll Evaluation. Three vessels sailing at a speed of 15 Kn, encounter beam seas with significant wave height H_S = 3 m. Vessel A has the best performance.

- by direct calculation of the seakeeping performance and implementation of specific criteria. The latter are acceptable limits that are set to ship's responses based on crew and systems degradation. The vessel is evaluated according to these criteria (Figure 2) to derive the sea conditions where the ships is operable. Then, on the basis of the statistical percentage of time these conditions prevail, an operability index is derived (absolute method). This method uses only qualitative criteria.

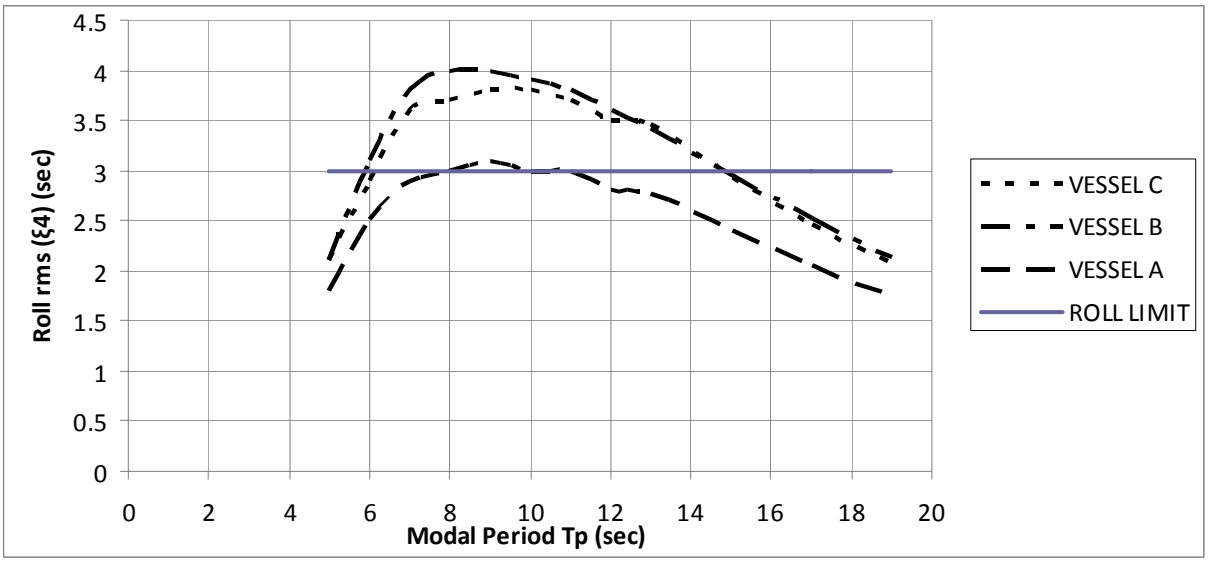

FIGURE 2. Absolute Method of Roll Evaluation. Three vessels sailing at a speed of 15 Kn, encounter beam seas with significant wave height H_S = 3 m. Vessels B and C violate the roll limiting criterion for RMS roll (3 deg) for waves with Modal Period in the 6 to 15 sec range. Vessel A has the best performance, since its roll response exceeds the criterion for Modal Periods in the 8 to 10 sec range.

In the case of direct calculation belong also the polar plots proposed by Comstock and Keane (1980) which are used to derive the operability index of a naval vessel in a specific sea condition. Such a plot extracted from the PNA (1989) is shown in Figure 3. On this plot, which is based on the seakeeping criteria of Table 1, the operating (non-shaded) and non-operating (shaded) areas are depicted. The shaded area is defined by one or more responses that exceed the limiting values (criteria). The operability index in a specified Sea State, assuming that all headings are equally probable and the higher speeds are more probable than the lower ones, is the ratio of the non-shaded area to the whole circular area. In other words, the bigger the non-shaded area the better the seakeeping performance of the vessel. Thus, these plots don't take into account the effect of speed and heading profiles of the vessel in a rational way. Furthermore, they should be derived for all possible sea conditions encountered by a vessel throughout its mission or life to come up with a mission or a through-life operability index.

To be more specific, warships operate in various sea areas performing multiple tasks. Following STANAG (2000) there is long list of mission scenarios, such as Anti-Aircraft Warfare (AAW), Anti-Submarine Warfare (ASW) etc. Thus, in order to derive a realistic overall operability index the following components should be considered:

1. Definition of missions (AAW, ASW etc).
2. Sea environment description (Wind and Wave Atlas).
3. Responses calculation (computer or/ and model simulation).
4. Criteria application (STANAG 4154, NORDIC Project).
5. Data collection and evaluation in order to calculate the operability indices.

These components can only be combined within an absolute method of seakeeping performance evaluation, as the one proposed in this paper, which is also quite robust. Among the data to be collected under (5) in the above list of components is the operational profile of the vessel in accomplishing each of the assigned missions and the probability of encountering a restrictive sea condition with given heading, significant wave height and modal period. This information is not provided in either of Figures 1 or 2.

TABLE 1. Mission criteria sets.

		Roll [deg]	Pitch [deg]	Yaw [deg]	LOCATION-DEPENDENT CRITERIA			
					No.	Vacc [g]	Lacc [g]	Vvel [m/sec]
TAP	Deck Wetness				30			
	Slamming				20			
	Personnel, Bridge	4	1.5			0.2	0.1	
	Propeller Emergence				90			
ASW	TAP Criteria AND …							
	Sonar Emergence				24			
	Active SONAR	7.5	2.5					
AAW	TAP Criteria AND…							
	Fwd Gun	3.8	3.8					0.5
	Missile Launch from VLS	8.8	1.5	0.8		0,3	0.35	
NAO	TAP Criteria AND…							
	Helicopter Landing	2.5	1					1

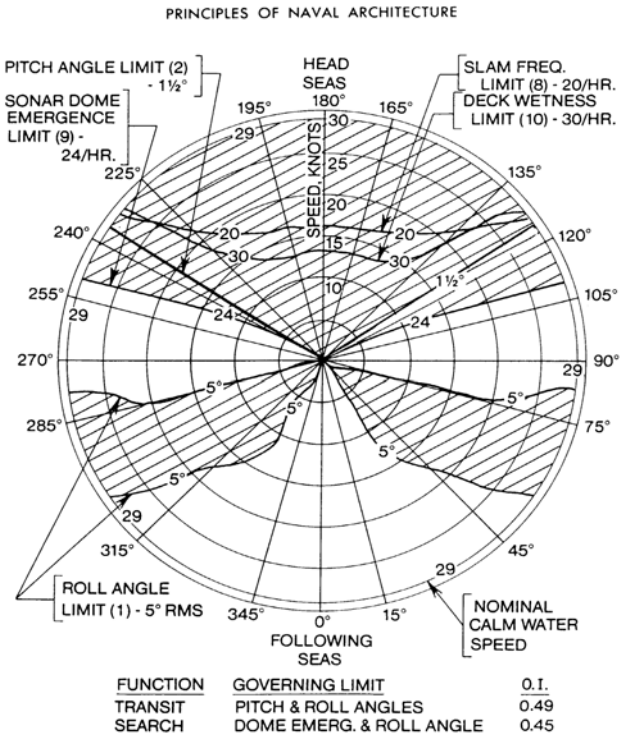

FIGURE 3. Polar Diagram for calculating the operability for TRANSIT and ASW operations at sea state 6 for all speeds and headings. The bigger the non-shaded area the better the seakeeping performance.

MISSION AND SEAKEEPING BEHAVIOUR OF THE HULL FORMS

Derivation of the Hull Forms

The prime scope of this paper is to present a rational comparison of three hull forms to be used as frigates serving Hellenic Navy and operating in the East Mediterranean sea region. Two

of the selected hull forms, the ONR 5415M and the ONR 5613 hull forms were scaled down from the destroyer to the frigate size (Figure 4). The former one is a well documented design available in the literature. The third hull form (HULL C) was manipulated in its real dimensions and was considered as a guide for scaling the other two.

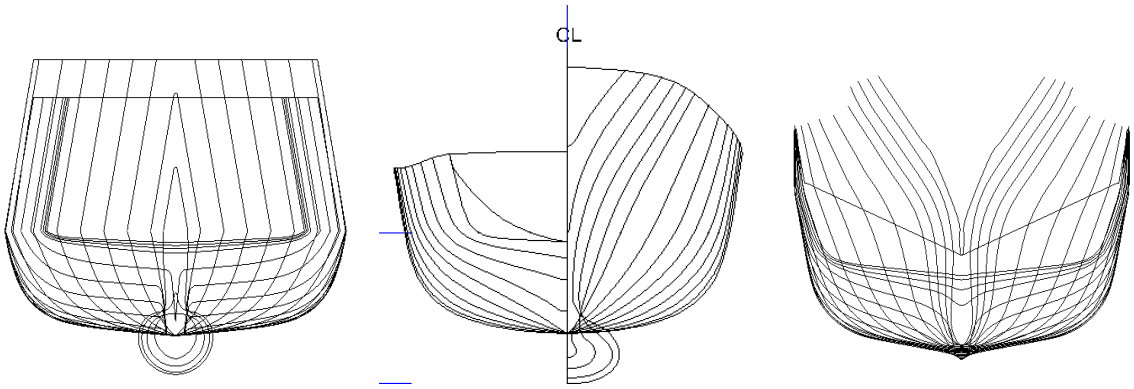

FIGURE 4. The investigated hull forms (HULL A, HULL B and HULL C)

TABLE 2. Main Particulars.

MAIN PARTICULARS	HULL A (ONR 5613)	HULL B (5415 M)	HULL C
Length Between Perpendiculars, L_{PP} [m]	109	109	109
Beam Amidships, B [m]	13.29	14.62	13.96
Draft Amidships, T [m]	3.89	4.72	4.32
Displacement in S.W. Δ [mt]	3087.6	3898.4	3441.1
Design Speed, V [kn]	30	30	30
Length/Beam Ratio L/B	8.199	7.456	7.806
Beam/Draft Ratio B/T	3.418	3.099	3.233
Draft/Beam Ratio T/B	0.293	0.323	0.309
Volume of Displ. / $(0.1L_{PP})^3$	2.325	2.934	2.59
Froude Number (Fn)	0.472	0.472	0.472
Vert. Centre of Gravity (KG) [m]	5.44	5.76	5.99
Metacentric Height (GM) [m]	1.41	1.46	1.41
Wetted Surface, WS	1590.2	1737.4	1619
Block Coefficient C_B	0.534	0.506	0.51
Prismatic Coefficient C_P	0.638	0.618	0.625

As reference for the scaling the length between perpendicular L_{PP} was used, while the ratios of the main dimensions were kept constant. Thus, the resulting hulls possess the same length L_{PP} but different displacement. Furthermore, the rest of the main dimensions are not the same (TABLE 2). The decision to compare the hull forms at their respective design conditions is based on the fact that the design condition is the most representative of each hull form, while the down-scaling of two of them was too mild to lead to un-realistic loading condition. In order to achieve greater accuracy, especially with roll response, the three hulls are examined with their appendages (Petropoulos, 2012).

Mission Definition

Naval vessels are generally built as multi-tasking platforms. Their sensors and arsenal is oriented to one mission, but the platform has the ability to perform successfully a variety of different missions by fitting and / or replacing devices, sensors or systems while the platform remains the same (modular concept). In this work four missions are depicted: Transit And Patrol (TAP), Anti-Air Warfare (AAW), Anti-Submarine Warfare (ASW) and Naval-Air Operations (NAO).

The seakeeping operability of the three competitors is examined in four areas of the Eastern Mediterranean Sea assuming four missions specified in NATO STANAG 4154 (2000) along with their respective platform criteria. Two ship speeds and three wave heading angles are accounted for in the presented test case out of the five headings that could cover all instances. The Western European Armament Organization (WEAO) Wind and Wave Atlas (2004) provides the necessary sea statistics. Plots have been produced to quantify the operability of each hull form in a specified area at constant heading and speed.

Sea Environment Description

In order to acquire reliable data for the sea environment, we use an Atlas. It is an edition where statistical data concerning wind speed, significant wave height, wave modal period, wind and wave directionality in various areas are gathered. The objective is to provide long term wind and wave statistics at specified points of a sea area (e.g. North Atlantic Ocean, Mediterranean Sea). For the purposes of this paper, the area of interest is focused on four points of the Eastern Mediterranean Sea (Figure 5). Statistical data related to the sea environment (wave direction, probability of occurrence, significant wave height and modal wave period) are derived from the WEAO Wind and Wave Atlas (2004).

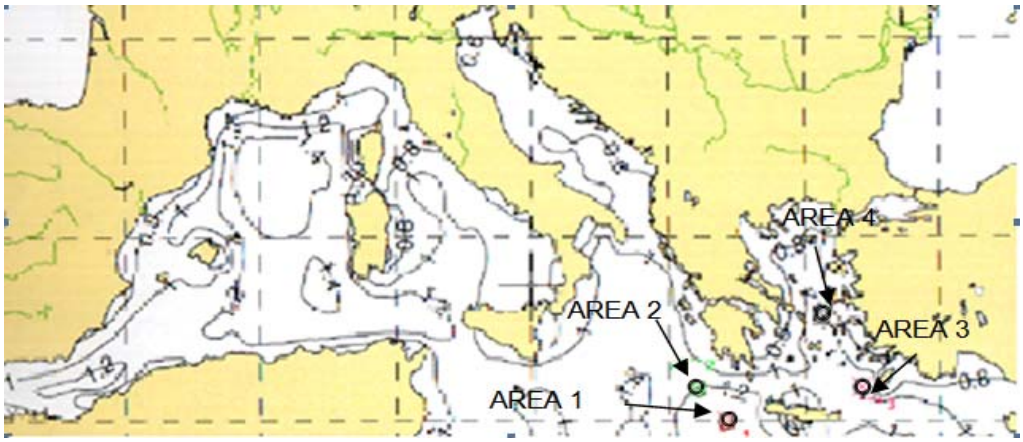

FIGURE 5. Areas of interest in the East Mediterranean sea region.

Calculation of the Dynamic Responses

In order to estimate the ship responses, the Standard Ship Motion Program of US Navy SMP 93-PC (Smith and Meyers, 1994) is used. This code is a frequency domain, strip theory based program, able to calculate responses in all six degrees of freedom (surge, sway, heave, roll, pitch, yaw) as well as random events in irregular seas (long-crested and short-crested). Frank close-fit method is used to estimate the two-dimensional hydrodynamic characteristics (Frank, 1967). Up to ten sources are distributed on each half-section. A two-parameter Bretschneider

spectrum is used. Roll response calculations make use of Tanaka's roll damping coefficients. Rigid body motions as well as derived responses and random events were calculated in various locations onboard the three vessels.

TABLE 3. Locations onboard ship. Station number starts at Forward Perpendicular. Y is the transverse distance from the vertical symmetry axis. Z is the vertical distance from the keel.

NUMBER	NAME	STATION NR	Y [m]	Z [m]
	HULL A			
1	Helicopter Deck	17.4711	0	10.325
2	Bridge (Helmsman)	6.6249	0	19.18
3	FWD GMVLS Outer Corner	6	4.399	11.738
4	FWD Gun Barrel Tip	5	0	11.738
5	Slamming @ 3/20 L_{PP}	3	0	1.489
6	Deck Wetness @ 1/10 L_{PP}	2	0.748	11.739
7	Propeller Emergence	18.44	2.898	3.38
8	Sonar Dome Emergence	-0.0149	0	2.9
	HULL B			
1	Helicopter Deck	18.227	0	10.736
2	Bridge (Helmsman)	6.2	0	21.3014
3	5/54 Gun Barrel Tip	1.8822	0	14.9687
4	FWD GMVLS Outer Corner	5	5.682	12.0457
5	Slamming @ 3/20 L_{PP}	3	0	2.3186
6	Deck Wetness @ 1/10 L_{PP}	2	5.7444	13.5076
7	Propeller Emergence	19	3.5668	4
8	Sonar Dome Emergence	0.5	0	3.7913
	HULL C			
1	Helicopter Deck	18.4954	0	10
2	Bridge (Helmsman)	5.5046	0	15.6
3	5/54 GUN Barrel Tip	1.3211	0	10.3
4	GMVLS Outer Corner	12.6606	2.2	15.8
5	Slamming @ 3/20 L_{PP}	3	0	0.6666
6	Deck Wetness @ 1/10 L_{PP}	2	5.047	10.736
7	Propeller Emergence	18.935	3.25	2.8
8	Sonar Dome Emergence	3.5963	0	0.675

For the analysis described herein, the operating speeds are assumed to be 15 kn and 25 kn. Short-crested seas are considered. Calculations are made for eight locations onboard each ship (TABLE 3). The angles of wave encounter are 0^0 (head seas), 45^0 (bow seas) and 90^0 (beam seas). These three headings have been selected as the worst cases out of the five headings to keep the number of plots to a minimum. The two additional headings refer to 135^o (stern waves) and 180^o (purely following waves). The body plans are derived as described by Petropoulos (2012) and fed to the code. For the purposes of the study, the appendages that affect roll

response (skeg, non-retractable fins, rudders and bilge keels) are fed to the code. HULL A and HULL C are described by 25 stations, while HULL B is defined by 23 stations.

Application of Seakeeping Criteria

The criteria are taken from NATO STANAG 4154 (2000) and concern the four aforementioned operations. Human Performance Degradation Criteria such as Motion Induced Interruptions as well as wind speed (for NAO operations) are omitted. Roll criterion used for NAO mission is the generic one, described in STANAG 4154. The decision to study simultaneously criteria referring to four missions arises from the fact that a naval ship is a multitasking platform. Thus, it is more realistic to use “multi-mission criteria sets” instead of single-mission criteria (Smith and Thomas, 1989), as depicted in TABLE 1 for the four missions under consideration. In case a response is used as criterion in more than one missions, only the stricter is taken under consideration. For instance, both TAP and NAO missions include roll RMS value as a criterion. But the RMS value for a NAO operation has a lower value than that of a TAP mission. Thus, the limiting criterion is considered to be the stricter one (Roll RMS value for NAO operations).

A NEW METHOD TO ASSESS SEAKEEPING OPERABILITY

Following the discussion in the proceeding sections, the seakeeping operability of a naval vessel is directly related to a mission profile that actually constitutes its overall mission or at least the major part of it. The currently available methods either evaluate this property for a given sea condition (polar diagrams) or evaluate the upper limiting values of one or more responses for which the vessel is operable, disregarding the probability of encountering sea conditions for which the criteria are violated. Even the overall operability index derived by repetitive implementation of the polar diagrams for the long list of the sea conditions that the vessel may encounter during a year or through life is based on the statistics of the waves in one or more sea areas, without taking into account the mission profile and the associated speed and heading profiles for the specific naval ship.

In the present study, a different approach is used, based on the method recommended by Andrew, Loader and Penn (1984) in its simplified version as described by Lloyd (1989). The Operability Index for each ship sailing at a chosen area location, speed and angle of encounter over a year is graphically presented. The Modal Period T_P, and the Significant Wave Height H_S are the abscissa and the ordinate of the plot, respectively. The wave probability of occurrence, taken from the WEAO Atlas is inserted and criteria of the four missions are plotted. The shaded area under the stricter criterion curve specifies the operable area for the ship at the specific pair of speed and heading angle. The operability index is the ratio of the shaded area to the area where there is a wave probability of occurrence. The probability of occurrence of each combination of H_S and T_P can be directly taken into account in whole or partly (if the respective parallelogram is crossed) as weighting in the evaluation of the operability index. Both the overall operability for all set criteria as well as the respective one for any single criterion or combination of criteria can be evaluated using the same plot.

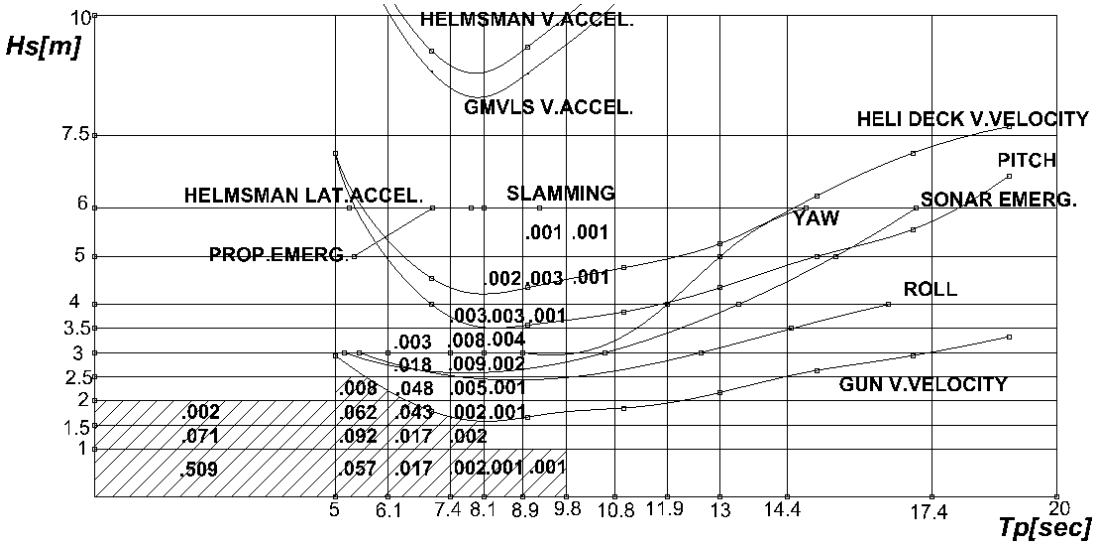

FIGURE 6. Operability calculation at a specific ship speed and wave heading and is based on the wave statistics of a specific area.. All criteria are plotted on a Cartesian coordinate system. Ship responses are calculated for a specific heading to derive the limiting (T_P, H_S) pairs. The shaded area represents the operability index for the specific area, ship, speed and heading.

In order to calculate the final operability of the vessel in the specific area, the course of the vessel to its mission in Cartesian Coordinates is combined with the directional wave statistics in the area to derive the probability of encountering specific headings. Then at each heading for which a plot like the one in Figure 6 is built, a weighting factor corresponding to the probability of encountering that heading is derived. The weighting factors are derived on the basis of TABLES 4 and 5. The former table presents the course of the vessel in the selected sea areas, while the latter one provides the probability of encountering waves with heading 0°, 45° and 90° in these areas.

TABLE 4. Ship's Course definition.

Area	Ship Course (^{0}) Relative to North
1 (35N,22E)	45
2 (36N,21E)	90
3 (36N,27E)	135
4 (38N,25.5E)	0

TABLE 5. Wave Probability of Occurrence/ Directionality.

Area	Course (^{0})	Wave Probability of Occurrence/ Directionality (^{0})		
		0	45	90
1	45	$0.1519/30^0 \div 60^0$	$0.0835/345^0 \div 15^0$	$0.3854/300^0 \div 330^0$
2	90	$0.1013/75^0 \div 105^0$	$0.0355/30^0 \div 60^0$	$0.0578/345^0 \div 15^0$
3	135	$0.0284/120^0 \div 150^0$	$0.0396/165^0 \div 195^0$	$0.0588/210^0 \div 240^0$
4	0	$0,541/345^0 \div 15^0$	$0.1074/300^0 \div 330^0$	$0.0294/255^0 \div 285^0$

Finally, the operability indices for every speed, area and course are as follows (TABLE 6).

TABLE 6. Final Operability Indices.

Final Operability Indices				
Area 1 35 N, 22 E				
Speed	**Course (^{0})**	**VESSEL A**	**VESSEL B**	**VESSEL C**
15	45	80.72%	75.42%	70.04%
25	45	78.91%	76.45%	70.94%
Area 2 36 N, 21 E				
Speed	**Course (^{0})**	**VESSEL A**	**VESSEL B**	**VESSEL C**
15	90	82.30%	77.78%	73,67%
25	90	81.30%	79.18%	74.17%
Area 3 36 N, 27 E				
Speed	**Course (^{0})**	**VESSEL A**	**VESSEL B**	**VESSEL C**
15	135	86.34%	81.79%	77.86%
25	135	85.43%	83.11%	78.25%
Area 4 38 N, 25.5 E				
Speed	**Course (^{0})**	**VESSEL A**	**VESSEL B**	**VESSEL C**
15	0	88.53%	86.11%	83.99%
25	0	89.54%	89.05%	84.97%

The overall operability performance assessment is calculated as the sum of the operability indices in all speeds, areas and courses. For simplicity reasons we may consider all ship speeds and areas as equally probable, otherwise we would have to make an assumption about their probabilities, thus we should insert weighting factors for each probability.

DISCUSSION AND CONCLUSIONS

In this paper a different approach for assessing the operability of three naval ships is briefly described. The method makes use of Cartesian Coordinates, in which a mission criteria set for four missions is graphically represented. The curves are drawn for each vessel, traveling in four areas, at two speeds and three angles of wave encounter (five angles are needed to take into account the following seas as well). These plots have the advantage of giving information about the seakeeping operability performance in all probable waves encountered in that area. The use of mission criteria sets gives the opportunity to choose which area and which ship is more suitable for each mission or combination of missions. In that way mission performance can be optimized. In addition, if consequential locations are selected, plotted and the results combined, it is possible to optimize ship's route, thus saving time and budget. Moreover, ship owners or Navy can compare different designs and arrive at safe conclusions about what vessel suits best their needs.

Following the results provided in graphical form, it is revealed that the gun barrel tip vertical velocity is the most limiting criterion (Figure 7). That was anticipated because the gun's location is close to the bow and thus exposed to large responses. On the other hand, keel mounted sonars suffer much less from sonar emergence than the hull mounted ones (Figure 8). Thus the designing trend to place keel mounted sonars in ships of that size is proved to be correct.

HULL A has the highest operability indices in every case. This may be due to:

1. The fact that the exact location of gun barrel tip wasn't known, thus an assumption had to be made. This is very important because the related criterion (gun barrel tip vertical velocity) is the stricter in every case examined.

2. The fact that this hull has an unconventional, wave piercing bow that moves through and not above waves.

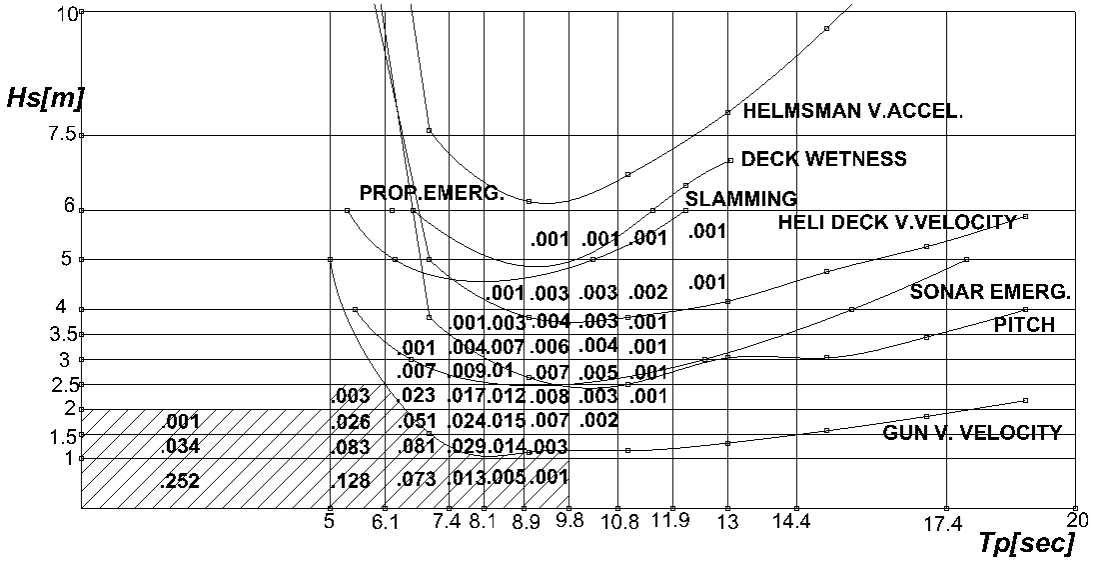

FIGURE 7. Altered 5415M plot for Area 1, at 15 kn in Head Seas. Criterion for gun barrel tip vertical velocity is the stricter of all.

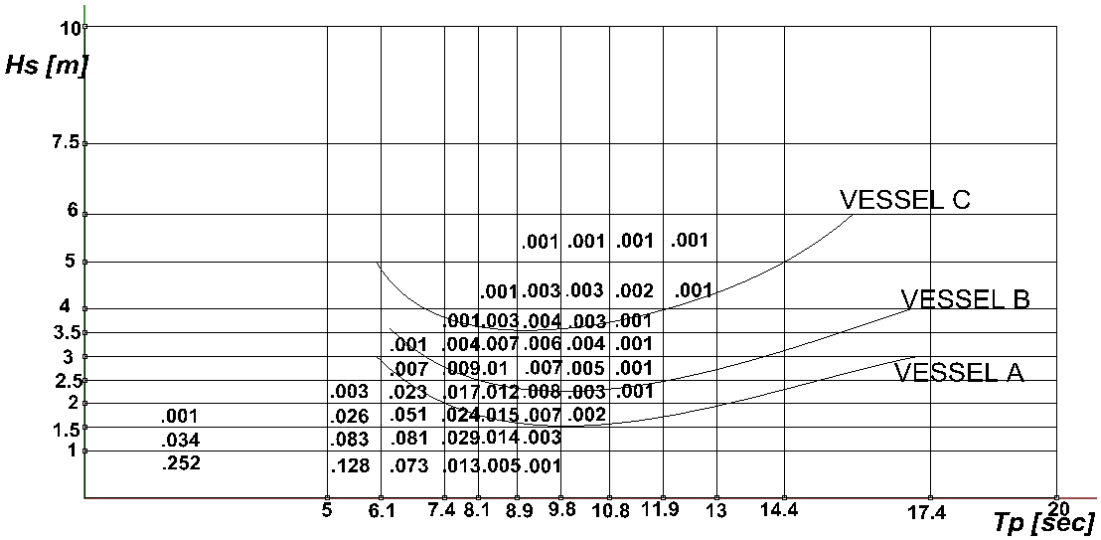

FIGURE 8. Sonar Emergence Criterion comparison for Area 1, at 25 kn in Head Seas. VESSEL C has a keel mounted sonar. The other two vessels have hull mounted sonars.

It must be emphasized that all operability performance assessment methods use a large amount of data and require a high degree of automation, especially in the plotting process. The method described is more convenient in case we are interested in a few missions in a specific area. If we intend to investigate the performance for a long list of missions, at many speeds, sea areas and courses the results may give a more precise insight, but in that case the amount of data would be of considerable amount. Thus, the development of a code able to use all information in an automated way and plot the diagrams is of crucial importance to take full advance of the method.

REFERENCES

1. Bales, N.K., "Optimizing the Seakeeping Performance of Destroyer-Type Hulls", Office of Naval Research, *13th Symposium on Naval Hydrodynamics*, Tokyo, Oct. 1980.
2. Frank, W., 'Oscillation of Cylinders in or Below the Free Surface of Deep Fluids', NSRDC, Rep. No. 2375, Washington, D.C., 1967.
3. Grigoropoulos, G.J and Loukakis, T.A., "On the Optimization of Hull Forms with Respect to Seakeeping", *5th IMAEM Congress*, Athens, May 1990.
4. Grigoropoulos, G.J., "Hull Form Optimization for Hydrodynamic Performance", *Marine Technology*, Vol. 41, No. 4, October 2004
5. Grigoropoulos, G.J. and Petropoulos, G.P., "A New Methodology for the Operability Performance Assessment of Naval Ships", 2012, to appear.
6. Comstock, E.N. and Keane, R.G., "Seakeeping by Design", Naval Engineers Journal, April 1980.
7. Lewis, E.V., "Principles of Naval Architecture 2nd Revision Vol 3, Motions in Waves and Controllability", SNAME, 1989.
8. Lloyd, A.R.J.M., "Seakeeping: Ship Behavior in Rough Weather", Ellis Horwood Ltd,1989.
9. NATO, "STANAG 4154 Edition 3", 2000.
10. NORDIC Project Board, "Assessment of Ship Performance in a Seaway", NORDFORSK, NORDIC Co-operative Project : Seakeeping Performance of Ships, Copenhagen, Denmark, 1987.
11. Petropoulos, G.P., "Seakeeping Operability of Large Naval Vessels in the Aegean Sea Environment", MSc Thesis, NTUA, 2012.
12. Smith, T. C. and Meyers, W. G., "SMP 93-PC User Manual", Carderock Division, Naval Surface Warfare Center, 1994.
13. Smith, T. C. and Thomas, W. L., "A Survey and Comparison of Criteria for Naval Missions», DTRC / SHD -1312-01, 1989.
14. WEAO, "Wind and Wave Atlas of the Mediterranean Sea", Western European Armaments Organization Research Cell, ISBN 2-11-095674-7, 2004.

Comparative Evaluation of the Effects of Intake Air Nitrogen-Enrichment and EGR on the Operational and Environmental Behavior of a SI Heavy Duty Natural Gas Engine

Roussos G. Papagiannakis[a] and Theodoros C. Zannis[b]

[a]*Thermodynamic & Propulsion Systems Section, Hellenic Air Force Academy, Dekelia Air Force Base, MP 1010 Dekelia, Attiki, Greece, r.papagiannakis@gmail.com*

[b]*Laboratory of Marine Internal Combustion Engines, Naval Architecture & Marine Engineering Section, Hellenic Naval Academy, Hatzikiriakio, 185 39 Piraeus, Greece, thzannis@snd.edu.gr*

Abstract. In natural gas spark-ignited engines operating under lean conditions, low temperature combustion is identified as one of the pathways to meet the mandatory ultra low NOx emissions levels set by the regulatory agencies. Exhaust gas recirculation (EGR) has proved to be an effective methodology to reduce in-cylinder combustion temperature and hence NO_x emissions. Nitrogen enrichment of the inducted air is an effective, alternative to EGR, methodology to reduce NOx emissions, since the introduction of inert diluents, such as nitrogen, into a fuel-air mixture results in reduction of the in-cylinder combustion temperature. Since nitrogen-enrichment of intake-air and exhaust gas recirculation (EGR) are two important methods that mostly affect the combustion process occurring within the combustion chamber of natural gas spark-ignited engines, the present work studies their effect on the performance and exhaust emissions of a multi-cylinder, four-stroke, turbocharged, spark-ignited engine fuelled with natural gas. Hence, a theoretical investigation is conducted by using a comprehensive, two-zone, phenomenological model. The model has been properly modified and substantially improved to describe, in a detailed way, the combustion process of the gaseous fuel taking into account the aforementioned techniques. The results concerning engine performance characteristics, NO and CO emissions, with : (i) normal oxygen mass fraction of the inducted air (i.e. normal engine operation NEO), (ii) nitrogen-enriched inducted air (NEIA) and (iii) EGR operating modes, for various engine operating conditions, come from the application of the model. The main objectives are to record and also to comparatively evaluate the relative impact that each one of the above mentioned methods has on the engine performance characteristics and emitted pollutants. Thus, comparing the theoretical results when engine operates with (i) NEIA or (ii) EGR mode, as against with NEO mode, a considerable effect on engine performance and emission characteristics are revealed. Another objective of this assessment is to quantify NO reduction benefit achieved with each of the two strategies examined. The conclusions of the specific investigation will be extremely valuable for the application of the examined technologies on an existing spark-ignited natural gas engine.

Keywords: natural gas, spark ignition, nitrogen enrichment, exhaust gas recirculation.

INTRODUCTION

For meeting stringent imposed emissions regulations, engineers working in the automotive industry or belonging to the research community have focused their interest either on the domain of engine- or fuel-related techniques, such as alternative gaseous fuels or oxygenated fuels that can mitigate emissions, used either in diesel or spark ignition engines that are well established as dominating power-train solution in the world market [1-9]. For the majority of heavy-duty spark-ignited engines, natural gas is most usually introduced with the air during the induction stroke. The majority of this type of engines features a homogeneous natural gas–air mixture compressed rapidly below its auto-ignition condition and ignited around top dead center (TDC) position by the existence of a spark plug. Under constant engine speed, the power output of the specific type of engine is controlled by changing the total amount of the inducted mixture (i.e. air and gaseous fuel). Substantial improvements of these engines in terms of brake specific fuel consumption and reduction of pollutant emissions has been achieved, over the last years, by adopting various engine-related techniques, such as the homogeneous charge compression ignition (HCCI), the micro pilot combustion, the exhaust gas recirculation (EGR), the nitrogen enrichment of the inducted air with the use of air separation membrane (ASM) [10-13] etc. While, each concept has its advantages and disadvantages, exhaust gas recirculation (EGR) has proved to be a very effective tool to reduce the nitrogen oxide emissions. However, exhaust gas recirculation has some significant demerits, such as increased CO emissions, decreased brake thermal efficiency, combustion contamination, greater control system complexity, application variability, material durability, lubricant contamination and increased PM emissions. On the other hand nitrogen enrichment of the inducted air (NEIA) could be an effective strategy, alternative to EGR, without the undesired consequences [10-13]. This strategy could be achieved using a mature technology which involves selective permeation of gases using an air separation membrane [10-13]. Introduction of inert diluents such as nitrogen, into a fuel-air mixture, slow down the reaction rates of participating chemical species, which eventually leads to lower combustion temperatures and hence lower nitrogen oxides. This process gives an added control parameter to reduce combustion temperature in advanced engines.

It is true that experimental work concerning fuel economy and low pollutant emissions from internal combustion engines includes successive changes of each of the many parameters involved, which is very demanding in terms of money and time. Today, the development of powerful digital computers leads to the obvious alternative of simulating the engine performance by mathematical modeling, where the effect of various design and operation changes can be estimated in a fast and inexpensive way. The need for accurate predictions of emitted pollutants has forced researchers to develop two-zone combustion models, accompanied with studies of the significant process of heat transfer in engines, many aspects of which are still unexplored. Eventually, some multi-zone combustion models have appeared where the detailed analysis of fuel-air distribution permits the calculation of exhaust gas composition with reasonable accuracy, but under the rising of computing time cost when compared to lower zones combustion models. At this point it is mentioned that multi-dimensional models have proved useful in examining problems characterized by the need for detailed spatial information and complex interactions of many phenomena simultaneously, but they are limited by the relative inadequacy of sub-models for turbulence, combustion chemistry and by computer size and cost of operation, to crude approximations to the real flow and combustion processes. Thus, it is felt that a good choice for the present study is a two-zone model, which includes the effect of changes in engine design and operation on the details of the combustion process, via a phenomenological model where the geometric details are fairly well approximated by detailed modeling of the various mechanisms involved. This is to have the advantage of relative simplicity and reasonable computer time cost. Numerous experimental and theoretical

investigations concerning the effect of (i) nitrogen-enrichment of intake-air [10-16] and (ii) exhaust gas recirculation (EGR) [17-23] on performance and exhaust emissions of an engine have been reported in the international literature.

The primary objective of the present work is to examine, using a theoretical model, the effect of nitrogen-enrichment of intake-air (NEIA) and exhaust gas recirculation (EGR) on the performance and exhaust emissions of an existing stationary, spark-ignited, engine fuelled with natural gas. The theoretical results are generated using a two-zone phenomenological combustion model, which predicts in-cylinder pressure and heat release rate histories, as well as NO and CO concentration profiles. Several of the model predictions on performance and emissions characteristics of the examined engine, have been presented already in the past [14-16]. For the current investigation, the simulation model has been properly modified and improved substantially to describe more accurately the complicated natural gas combustion process in a spark ignition engine environment, taking into account the details of the processes concerning the nitrogen-enrichment of intake-air (NEIA) and exhaust gas recirculation (EGR) and hence, their effects on the combustion process.

The theoretical results corresponding to engine operation without EGR and nitrogen-enriched inlet air (i.e. normal engine operation – NEO operating mode), are validated against respective experimental values obtained from a a multi-cylinder, turbocharged, water-cooled, spark-ignited engine operating under NEO mode at various engine operating points (i.e., load and engine speed) with natural gas. From the comparison of computed and experimental findings, it is revealed that the simulation model developed predicts adequately the engine performance and pollutant emissions trends with engine load under natural gas operation. Furthermore, taking into account data from the international literature, it is shown that the developed model could be used to examine the effect each one of the examined engine parameters on engine performance and pollutant emissions. In any case, it can be used safely in the present work, which performs a comparative assessment by using the simulation results concerning the relative impacts of the examined parameters on engine performance characteristics and emitted pollutants. The results reported herein concern the calculated maximum combustion pressure, ignition delay, duration of combustion, total brake specific fuel consumption, and the calculated brake specific NO and CO emissions, for intermediate and high engine loading conditions at 1500 rpm engine speed. The comparative assessment is accomplished through the comparison of results corresponding to engine operation with EGR or air inlet nitrogen-enrichment, with the corresponding ones corresponding to normal engine operation. From the theoretical findings, important information is derived revealing both the applicability each one of the examined techniques on an existing spark-ignition engine operating with natural gas and also the effect of each technique on engine performance and pollutant emissions.

Consequently, the information derived from the present work is extremely valuable regarding the implementation one of the two strategies examined in the present work for improving the environmental behavior of an existing heavy-duty spark-ignited engine fuelled with natural gas, without deteriorating seriously its performance.

BRIEF DESCRIPTION OF THE MODEL

In the present work only an outline of the model is given since its details have been presented in previous publications [14,16]. The simulation model used is a phenomenological two-zone one, examining the closed part of the engine cycle. At the start of the compression stroke, the cylinder charge is assumed to be a homogeneous mixture of air and gaseous fuel, which has been properly premixed during the induction stroke. During the compression stroke, the entire charge of the mixture is treated as a single zone up to the initiation of combustion. Here, at each instant of time, the perfect gas law describes the state of the mixture inside the

cylinder, while there is uniformity in space of pressure, temperature and composition. As is well known, the combustion process of a SI engine is divided into two processes, that is, the ignition process and the stable flame propagation process [24-28]. The former one is made of the flame kernel, which is formed by a spark electric discharge and the unstable flame propagation of the kernel. This is, however, treated as a SI delay period. In the proposed model, the initiation of combustion is assumed to take place when a finite volume of the burned mixture (i.e. the volume of the flame kernel formed by the spark discharge) exceeds 0.001 times the total cylinder volume, that is, displacement plus clearance volume (see Figure 1).

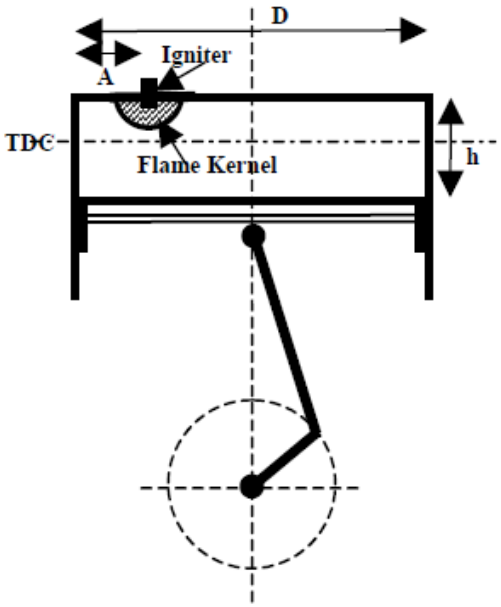

FIGURE 1. Schematic diagram of the flame kernel formation.

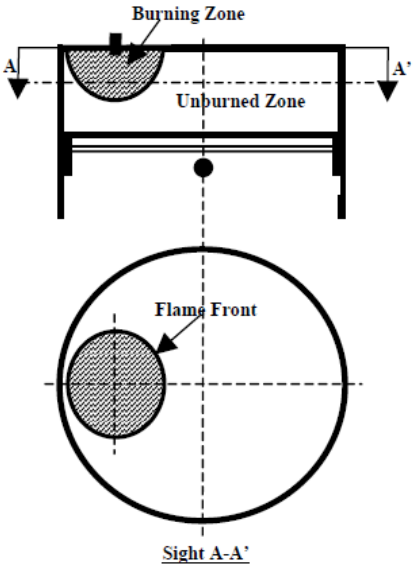

FIGURE 2. Two-zone thermodynamic model of combustion process.

When combustion is initiated, a two-zone phenomenological model is considered to exist for the rest of the closed part of the engine cycle. The first zone consists of air–gaseous fuel mixture (unburned zone), while the second one (burning zone) consists of combustion products and excess air depending on the AFR (air to fuel ratio) (see Figure 2). In each zone, there is uniformity in space of pressure, temperature and composition, at each instant of time, neglecting heat exchange between the zones. After the spark plug ignition, the two zones are separated by a thin flame front that has the shape of a sphere. During the combustion process, the instantaneous cylinder volume and its derivative with respect to crank angle, the flame front area, and the area of the combustion chamber in contact with the unburned and burning zones, are computed through the respective geometric sub-models. Assuming that the geometry of the flame front formed inside the chamber of a spark-ignited engine has a spherical form [2-3], the determination of the instantaneous flame geometry after spark discharge is achieved in the present work by applying a model developed by Annand [28]. The flame front spreads towards the unburned zone, having a flame speed that is calculated by taking into account both the turbulent flame propagation mechanism and the percentage of the nitrogen-enriched inducted-air [27]. After the initiation of combustion, the volume of the burning zone changes due to the existence of the flame front which spreads towards the unburned zone having a turbulent flame speed. The volume change of the burning zone leads to the computation of the quantity of the gaseous fuel and air entrained into the zone. Since the laminar flame thickness under engine conditions is infinitesimal [2-3], in the present model the flame is treated as negligibly thin. The present model assumes that a flame front of negligible thickness propagates into the unburned

zone, having a direction perpendicular to the outer spherical surface of the burning zone formed after the initiation of combustion. The gaseous fuel entrained inside the burning zone, due to the flame front spread, is transformed into products. Thus, the combustion rate depends actually on the turbulent flame speed. Heat exchange rate for each zone is calculated by employing the Annand formula [29]. After the initiation of combustion, each zone possesses its own temperature and composition, while the pressure is uniform inside the cylinder. Dissociation of combustion products is taken into account by using the Vickland et al. [30-31] method, incorporating 11 chemical species. For the formation of NO, the extended Zeldovich chain reaction mechanism is considered [30-31].

Model Modifications - Improvements

Below, is given an analysis of the most important modifications performed to the engine simulation model regarding the definition of the calculation of the laminar flame speed and the definition of the charge mixture composition at inlet valve closure (IVC) corresponding to air inlet nitrogen-enrichment and EGR operating modes.

Laminar Flame Velocity

The laminar flame velocity is defined as the relative velocity, with which the unburned gas moves inside the flame front and is transformed to products [2-4]. It is an important intrinsic property of a combustible mixture. The laminar flame velocity developed inside a combustion chamber depends mainly on the equivalence ratio, the temperature of the unburned gas and the pressure [2-4]. Since methane is the main constituent of natural gas, the laminar flame velocity in the present model is obtained by applying a correlation proposed by Karim [32], which simulates adequately the burning velocity of Methane – Air mixtures. The mathematical formula has as follows:

$$S_l = A + \left(F_1 \cdot F_2\right) \cdot \left(F_3 + F_4\left(\varphi_u - 1.036\right) + F_5\left(\varphi_u - 1.036\right)^2\right) \quad (1)$$

where A, F_1, F_2, F_3, F_4 and F_5 are correlations given in [32] that take into account the gaseous fuel equivalence ratio of unburned zone (φ_u), the cylinder pressure and the temperature of the unburned zone. The main advantage of the proposed correlation is that it can predict adequately the laminar burning velocity for non-stoichiometric region.

Definition of the Actual Mass Flow Rate of the Inducted Air at Inlet Valve Closure (IVC)

Under EGR operating mode, the percentage of the exhaust gas re-circulated (x_{EGR}) is defined via the formula:

$$x_{EGR}\left(\%\right) = \frac{\dot{m}_{EGR}}{\dot{m}_{mix,IVC}} \cdot 100\% \quad (2)$$

where ($\dot{m}_{EGR}$) represents the mass flow rate of exhaust gas re-circulated, and ($\dot{m}_{mix,IVC}$) represents the total mass flow rate of gaseous mixture inside the cylinder at inlet valve closure. The latter is calculated by taking into account the pressure, temperature and concentration of the mixture at inlet valve closure. The pressure is assumed to be the one after the air-compressor as this is a turbocharged spark ignited heavy duty engine. It is well known that re-circulated exhaust gas displaces some of the air entering the combustion chamber. Thus, the actual mass flow rate of the inducted air at inlet valve closure is calculated as:

$$\dot{m}_{air,IVC} = \left(1 - x_{EGR}\right) \cdot \dot{m}_{mix,IVC} \quad (3)$$

Then, for specific total air excess ratio, the actual mass flow rate of natural gas is calculated by taking into account the actual mass flow rate of the inducted air as follows:

$$\dot{m}_{NG} = \frac{\dot{m}_{air,IVC}}{AFR_{st} \cdot \lambda} \tag{4}$$

where AFRst corresponds to the stoichiometric air to fuel ratio (by mass) for natural gas. It must be stated here that the mixture at inlet valve closure is assumed to be an ideal homogeneous mixture with uniform composition and thermodynamic properties. It consists of fresh air, gaseous fuel, and re-circulated exhaust gas. The re-circulated exhaust gas is assumed to consist of CO_2 and H_2O, the concentrations of which are obtained from the composition of the cylinder charge at exhaust valve opening event. Moreover, the temperature of the re-circulated exhaust gas is calculated at the exhaust valve opening condition by running the in-house made software for the baseline Normal Engine Operation (NEO). Under nitrogen-enriched air inlet (NEIA) operating mode, nitrogen enrichment alters the chemical composition of the inducted air because N_2 displaces a portion of the inducted air that would otherwise be utilized during combustion, resulting in lowering of the total air excess ratio. In the proposed model, for each load examined (i.e. air excess ratio value), the actual mass flow rate of the air at inlet valve closure ($\dot{m}_{air,IVC}$) is calculated taking into account the percentage of nitrogen enrichment in the inducted mixture combined with the air mass flow rate corresponding to NEO operating mode. The percentage of nitrogen enrichment in the inducted mixture (Δy_{N_2}) is defined as :

$$\Delta y_{N_2}(\%) = \frac{y_{N_2}^{NEIA} - y_{N_2}^{NEO}}{y_{N_2}^{NEO}} \cdot 100 \tag{5}$$

where ($y_{N_2}^{NEIA}$) represents nitrogen concentration (by volume) in the inducted mixture under NEIA operating mode while ($y_{N_2}^{NEO}$) represents nitrogen concentration (by volume) in the inducted mixture under NEO operating mode. Furthermore, the gaseous fuel consumption ($\dot{m}_{NG}$) is calculated by EQ(4).

TEST CASES EXAMINED

In the present work, the simulation model is used to investigate the relative impact of air inlet nitrogen enrichment and exhaust gas recirculation on the performance characteristics and exhaust emissions of a heavy duty, spark-ignited natural gas engine fuelled with natural gas. Thus, at partial (i.e. 65% of full load) and high (i.e. 100% of full load) load conditions, the percentage of nitrogen concentration in the inducted air was increased by 2, 4 and 6 per cent (Δy_{N2} = 2%, 4% and 6%) relative to the convectional operating case (i.e. 79% by volume in air). Thus, for each loading point examined, besides the oxygen mass fraction of the inducted mixture corresponding to the conventional operating case ($x_{O_2} = 23,2\%$), three different oxygen mass fractions were estimated. Specifically, oxygen mass fraction of the inducted mixture was decreased from $x_{O_2} = 23,2\%$ to $x_{O_2} = 18\%$, at both engine loading conditions examined. Moreover, for each loading point examined, three different EGR percentages were examined herein. Specifically, for each engine load condition, the appropriate EGR percentage was estimated in order that the inducted mixture oxygen mass fraction resulting from the EGR application becomes equal to the respective oxygen mass fraction derived from the application of nitrogen-enrichment operating mode. Thus, under EGR operating mode, EGR percentage was increased from $x_{EGR} = 0\%$ to $x_{EGR} = 15\%$ at partial load conditions, while at high load

conditions it was increased up to $x_{EGR} = 10\%$. It must be stated here that the test case corresponding to $x_{O_2} = 23,2\%$ (by mass) nitrogen concentration in the inducted air and $x_{EGR} = 0\%$ is referred as 'normal engine operating point' (NEO point). Moreover, for each test case examined, the injection advance was kept constant. In Table 1 more details are given about the test cases examined in the present work.

Table 1. Test Cases Examine

$x_{O_2}(\%)$	65% Load & λ_α = 1,66 & 1500 rpm			100% Load & λ_α = 1,85 & 1500 rpm		
	λ_{O_2}	$\Delta y_{N_2}(\%)$	$x_{EGR}(\%)$	λ_{O_2}	$\Delta y_{N_2}(\%)$	$x_{EGR}(\%)$
23,2	1,73	0	0	1,92	0	0
21,5	1,60	2	5	1,78	2	6
19,8	1,47	4	10	1,63	4	12
18	1,34	6	18	1,49	6	20

MODEL VALIDATION

Results obtained from an extended experimental investigation conducted in the past on a 'GE Jenbacher 320', multi-cylinder, spark-ignited engine [15] are used to experimentally validate the predictions of the simulation model. The basic data related to the simulated engine are presented in Table 2 [15].

Table 2. Basic data of the Test Engine.

Engine Type	**V-70^0, 20 Cyl., 4-Stroke, SI, T/C**
Bore	135 mm
Stroke	170 mm
Connecting Rod	320 mm
Compression Ratio	11:1
Engine Displacement Volume	48,7 lt
Normal SOI (at 100% load)	23 ^{o}CA before TDC

This is a four-stroke, turbocharged, water-cooled, spark-ignited engine fuelled with natural gas. Since the specific engine is used as an electric power generator (actually in a co-generation mode), the normal speed of the engine is fixed at 1500 rpm and it is kept constant for the entire range of loads examined. A comparison between experimental and calculated pressure traces under NEO operating mode is given in Figure 3. Also, in figure 4 are compared experimental and calculated values of (i) engine power, (ii) engine efficiency and (iii) NO emissions. All experimental data were taken at four different engine loads corresponding to 40, 65, 85 and 100% of full engine load and at 1500 rpm engine speed. Examining these figures, it is observed that there is a good coincidence between calculated and experimental values at all test cases examined. This proves the ability of the specific model to predict adequately performance characteristics and the exhaust emissions of a spark ignition engine operating under natural gas fuel mode with normal chemical composition of the inducted air.

Furthermore, taking into account experimental data it is shown that the simulation model manages to predict with adequate accuracy the trend of the engine performance characteristics with the change each one of the examined techniques. Thus, the specific model can be used to look into the effect each one of the examined parameters on performance and pollutant emissions of the specific engine. It is emphasized here that the values of the present model's constants are held constant for all strategies examined in the present work (i.e. NEIA and EGR).

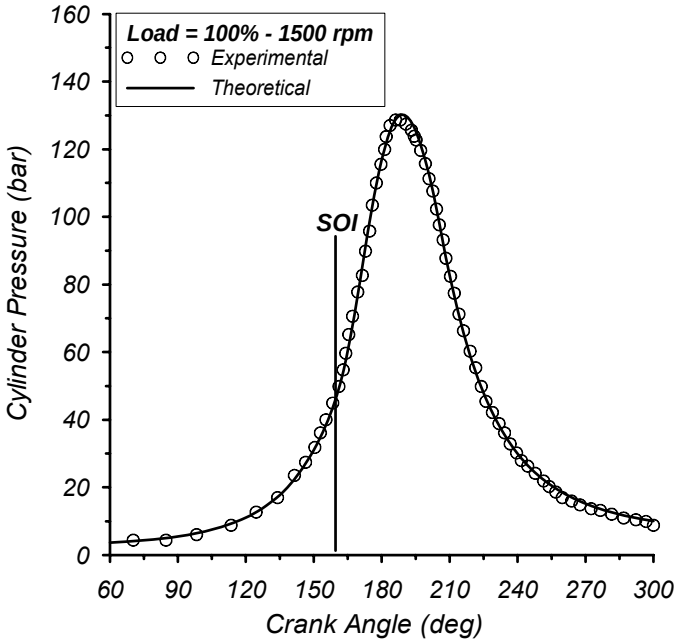

FIGURE 3. Comparison of experimental and computed pressure traces at the engine speed of 1500 rpm and 100% load.

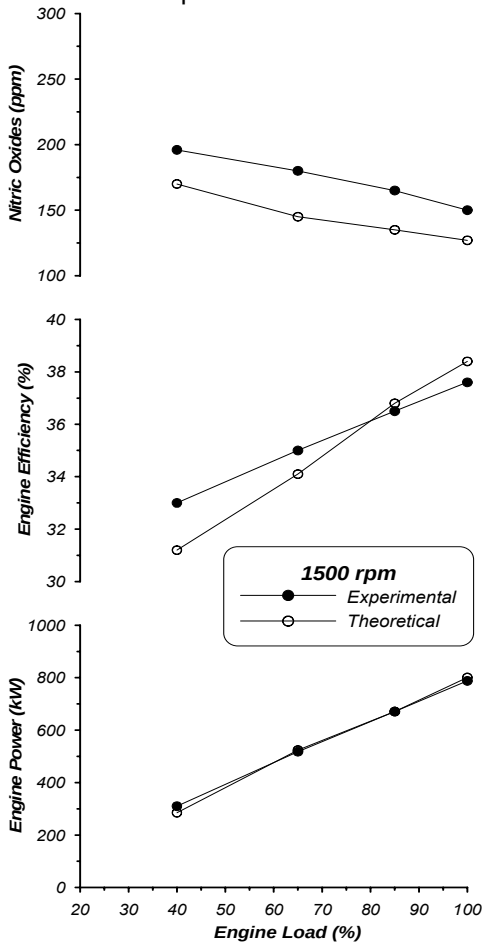

FIGURE 4. Computed and experimental values of (i) Power, (ii) Efficiency and (iii) NO emissions, versus engine load, at 1500 rpm engine speed.

RESULTS AND DISCUSSION

Comparative Evaluation of the Effects of Intake-Air Nitrogen-Enrichment and EGR on SI Natural Gas Engine Performance Characteristics

In this section, the predictive capabilities of the phenomenological model are explored. The predicted effects of the two strategies examined herein on some basic performance characteristics and pollutant emissions of a heavy-duty spark-ignited natural gas engine are examined, for two engine operating points corresponding to 65% and 100% of full engine load at 1500 rpm engine speed.

Figures 5-6 provide the predicted cylinder pressure and total heat release traces for x_{O2} = 19,75 (%) oxygen mass fraction of the cylinder charge at inlet valve closure event, at 100% of full engine load at 1500 rpm engine speed, using the two methodologies examined herein i.e. nitrogen enrichment of the inducted air (NEIA) and exhaust gas recirculation (EGR), respectively. In these figures the predicted cylinder pressure and total heat release traces are also given corresponding to normal engine operating (NEO) mode. Observing figure 5 it can be seen that the air inlet nitrogen-enrichment affects the cylinder pressure history. Thus, by raising the nitrogen mass fraction of the inducted mixture, the rate of cylinder pressure rise during the initial stage of the combustion process becomes lower, while the peak cylinder pressure occurs slightly later compared to the respective values observed under NEO condition. This is the result of both the later initiation of combustion and the lower combustion rate of the gaseous fuel, especially during the initial stages of combustion process, which occurred due to the lower cylinder charge temperatures. As far as the heat release rate curves are concerned (Figure 6), it is observed that the nitrogen enrichment affects also the burning rate. It is shown that the initiation of combustion observed with increased nitrogen mass fraction at IVC starts later compared to the respective one under NEO mode. This is attributed to the increase of ignition delay and also due to the fact that the combustion of the gaseous fuel has not yet progressed enough, since the cylinder charge conditions (i.e. cylinder charge temperature, etc.) do not favor the propagation of the flame front.

Observing figures 5-6, it is obvious that the presence of the exhaust gas re-circulated in the cylinder charge, affects both cylinder pressure and total burning rate. Thus, for high engine loading point, the increase of EGR affects the values of the cylinder pressure compared to the respective one observed under normal engine operating mode. The difference observed during the last stages of the compression stroke is the result of the higher specific heat capacity of the cylinder charge mixture (i.e. air-natural gas-EGR), compared to that of the air-natural gas in the case of NEO mode. Moreover, for all engine operating points examined, as EGR increases the rate of cylinder pressure rise during the first stage of the combustion process becomes lower, while the peak cylinder pressure occurs slightly later compared to the respective values observed without EGR. As far as the heat release rate curve is concerned (Figure 6), it is revealed that for the same oxygen mass fraction at IVC the initiation of combustion observed with EGR operating mode starts later compared to the respective one observed with air inlet nitrogen enrichment (NEIA mode). This is due to the fact that the cylinder charge with EGR (i.e. gaseous fuel – air – EGR mixture) has higher overall specific heat capacity compared to the respective one without EGR. Furthermore, as EGR increases the burning rate observed during the first stage of combustion decreases. This is due to the lower cylinder charge temperature that affects negatively the combustion process of the gaseous fuel, which has not yet progressed enough since the cylinder charge conditions during the specific phase do not favor the existence of the flame front.

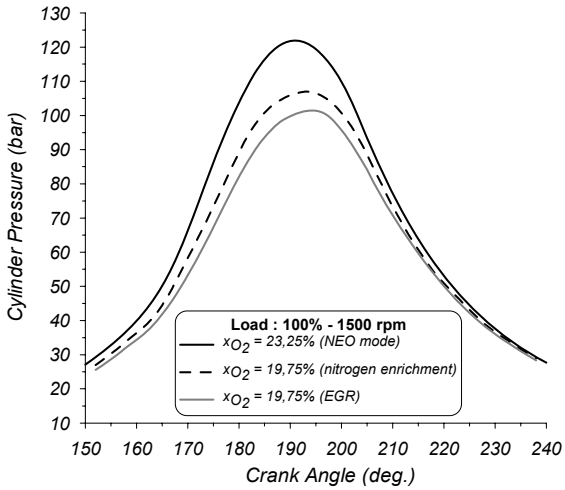

FIGURE 5. Calculated cylinder pressure traces at 1500 rpm and 100% load, for 19.75 (%) oxygen mass fraction in the inducted mixture using (i) air inlet nitrogen enrichment and (ii) EGR.

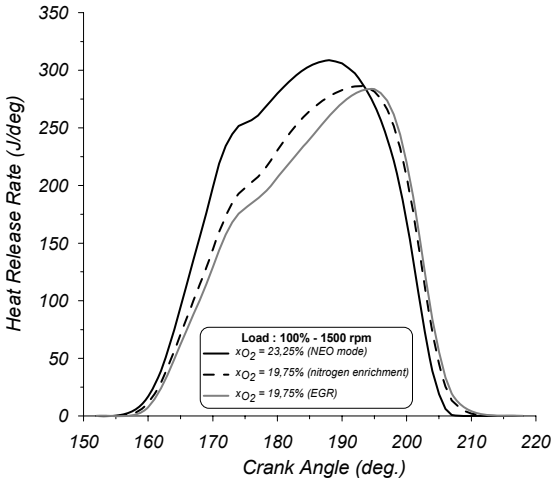

FIGURE 6. Calculated heat release rate traces at 1500 rpm and 100% load, for 19.75 (%) oxygen mass fraction in the inducted mixture using (i) air inlet nitrogen enrichment and (ii) EGR.

Figures 7A-B and 8A-B illustrate the variation of the calculated peak cylinder pressure and maximum cylinder temperature as a function of the oxygen mass fraction of the inducted mixture. The results correspond to 65% and 100% of full engine load conditions, for two strategies examined i.e. nitrogen enrichment and EGR, at 1500 rpm engine speed. In the same figures the normal engine operating point is also given, that corresponds to 23.2 (%) oxygen mass fraction (NEO mode). Since both maximum cylinder pressure and temperature are critical parameters affecting the mechanical and the thermal strength of engine structure, the study of the effect of the examined strategies on maximum cylinder pressure and temperature is of particular interest. By examining these figures, it is revealed that the maximum cylinder pressure decreases with the increase of the percentage of air nitrogen-enrichment resulting thus in lower cylinder charge temperatures. This is attributed to the decrease of the gaseous fuel combustion rate, due to the retardation of the flame front. The effect becomes more evident at full engine load conditions, where the decrease of the maximum cylinder temperature is up to 10%. For both loads examined, the decrease of the maximum cylinder pressure is not so severe (up to 10% at part load, and up to 8% at high load). Regarding the effect of EGR on both maximum cylinder pressure and temperature, it is observed that for all test cases examined, the increase of EGR leads also to the decrease of the maximum cylinder pressure and temperature. Despite the smooth decrease of the maximum temperature, the maximum cylinder pressure starts to decrease slightly with an increase of EGR until a certain limit, where a further increase of EGR leads to a more intense decrease of the maximum combustion pressure. The effect becomes more evident at high load. Eventually, it should be mentioned, that under EGR operating mode, the lower heat release rate and the higher specific heat capacity of the cylinder charge are the main reasons for the lower and delayed appearance of the maximum combustion pressure, compared to the respective values observed under NEO and air inlet nitrogen enrichment operating modes.

Figures 9A-B depict the variation of the calculated duration of combustion as a function of the oxygen mass fraction of the inducted mixture. The results correspond to 65% and 100% of full engine load conditions, for two strategies examined i.e. intake-air nitrogen-enrichment and EGR, at 1500 rpm engine speed. In the same figures the normal engine operating point is also given, that corresponds to 23.2 (%) oxygen mass fraction (NEO mode). Examining these figures, it is

observed that for both engine loads examined, both strategies examined herein lead to a longer duration of combustion as compared to the respective one observed under NEO mode.

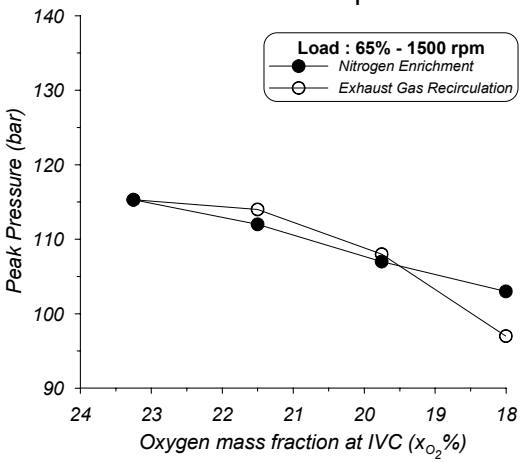

FIGURE 7A. Maximum pressure as a function of oxygen mass fraction of the inducted mixture, at 1500 rpm and 65% load, for (i) NEIM and (ii) EGR operating modes.

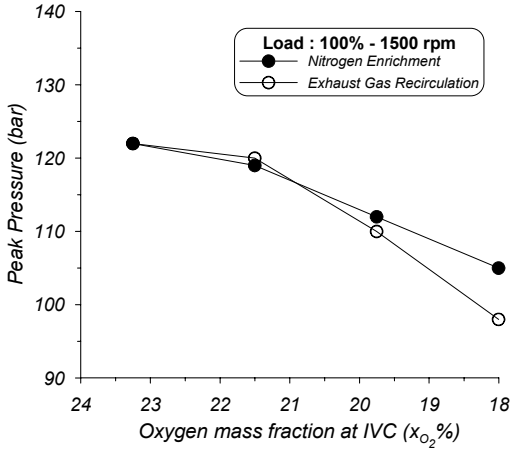

FIGURE 7B. Maximum pressure as a function of oxygen mass fraction of the inducted mixture, at 1500 rpm and 100% load, for (i) NEIM and (ii) EGR operating modes.

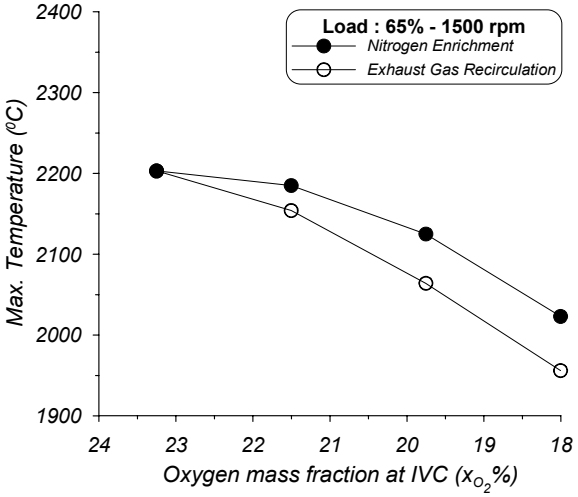

FIGURE 8A. Maximum temperature as a function of oxygen mass fraction of the inducted mixture, at 1500 rpm and 65% load, for (i) NEIM and (ii) EGR operating modes.

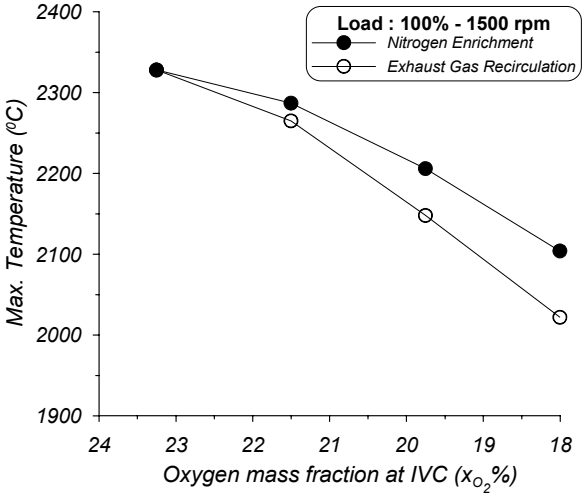

FIGURE 8B. Maximum temperature as a function of oxygen mass fraction of the inducted mixture, at 1500 rpm and 100% load, for (i) NEIM and (ii) EGR operating modes.

Specifically, nitrogen enrichment prolongs the duration of combustion and the specific effect becomes more intense at high load and high nitrogen percentages in the inducted mixture. This may be attributed, primarily, to the fact that nitrogen enrichment delays slightly the initiation of combustion. This emanates from the higher specific heat capacity of the mixture accompanied by the lower cylinder charge conditions occurring at the spark timing, compared to the respective values under NEO operating mode.

According to Figures 9A-B, it is observed that, despite the fact that the lower total air excess ratios, caused by the presence of EGR, is a critical factor favoring the flame propagation mechanism contributing, thus, to an improvement of the natural gas combustion quality, as EGR percentage increases the duration of combustion also increases. This specific effect is ascribed

primarily to the low cylinder charge temperature, due to the higher specific heat capacity of the cylinder charge and also to the slower combustion rate of the natural gas.

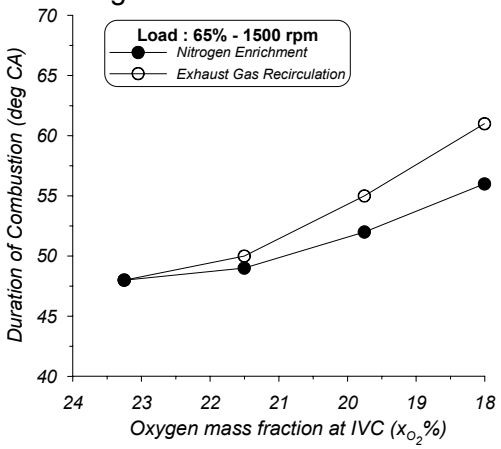

FIGURE 9A. Duration of Combustion as a function of oxygen mass fraction of the inducted mixture, at 1500 rpm and 65% load, for (i) NEIM and (ii) EGR operating modes.

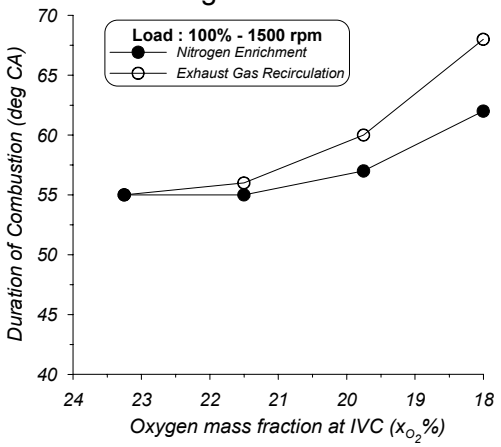

FIGURE 9B. Duration of Combustion as a function of oxygen mass fraction of the inducted mixture, at 1500 rpm and 100% load, for (i) NEIM and (ii) EGR operating modes.

Figures 10A-B illustrate the variation of the calculated brake specific fuel consumption (bsfc) as a function of the oxygen mass fraction of the inducted mixture. The results correspond to 65% and 100% of full engine load conditions, for two strategies examined i.e. nitrogen enrichment and EGR, at 1500 rpm engine speed. In the same figures the normal engine operating point is also given (NEO mode). It must be noted here that the computed bsfc is estimated from the calculated brake power output and the calculated mass flow rate of the natural gas. Moreover, brake power output is estimated from the calculated indicated power output (i.e. calculated from cylinder pressure diagram) and the mechanical efficiency that is predicted through a simple simulation sub-model. Observing these figures, it is revealed that for both loads examined, the increase of the nitrogen percentage in the inducted mixture results to an increase of bsfc since the combustion of the fuel becomes more ineffective. As far as the effect of EGR percentage on bsfc is concerned, it is revealed that the presence of EGR affects also the brake engine efficiency. Specifically, for both loads examined, the increase of the EGR percentage leads initially to a slight increase of the total brake specific fuel consumption, while a further increase of the EGR beyond a critical percentage results to a more intense deterioration of engine efficiency. This specific deterioration is ascribed primarily to the longer ignition delay period, which affects negatively the heat release rate, especially during the initial stages of combustion process. At the same time, the improvement of the gaseous fuel combustion quality, which is caused by the reduction of the total air excess ratio (i.e. lower total air excess ratio leads to faster flame speed), does not contribute considerably to the improvement of engine efficiency.

Comparative Evaluation of the Effects of Intake-Air Nitrogen-Enrichment and EGR on SI Natural Gas NO and CO Emissions

Figures 11A-B illustrate the variation of the calculated specific NO emissions as a function of the oxygen mass fraction of the inducted mixture. Theoretical results are presented at65% and 100% of full engine load conditions, for the two strategies examined herein i.e. nitrogen enrichment and EGR, at 1500 rpm engine speed. In the same figures predictions for the normal engine operating point are also given. It is well known [2-4] that the formation of NO is favored in general by high gas temperatures and near stoichiometric mixture conditions towards the lean.

Observing figures 11A-B, it is revealed that, for both loads examined, specific NO concentration under nitrogen enriched inducted mixture (NEIM) operating mode is lower compared to the one observed under NEO mode. For the same load, the burning temperature observed under NEIA mode is lower compared to the respective one under NEO mode. Moreover, nitrogen enrichment depletes effectively oxygen concentration in the cylinder charge. Thus, the lower oxygen concentration in combination with the lower burning temperatures provides a possible explanation about the lower NO concentrations observed under NEIM operating modes compared to the respective ones under NEO operating mode.

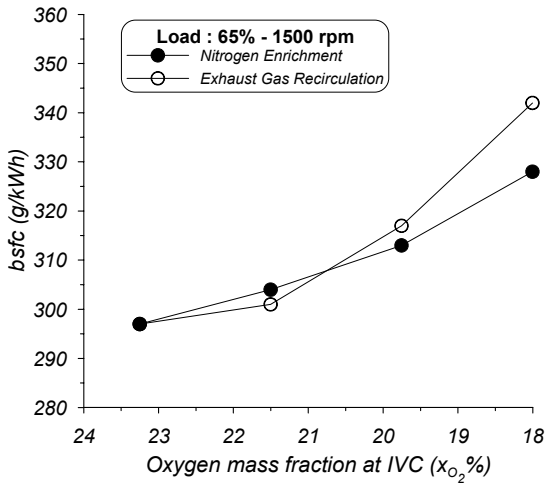

FIGURE 10A. Brake specific fuel consumption as a function of oxygen mass fraction of the inducted mixture, at 1500 rpm and 65% load, for (i) NEIM and (ii) EGR operating modes.

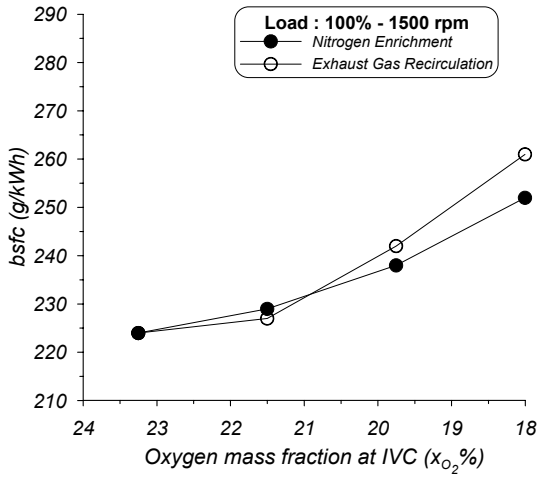

FIGURE 10B. Brake specific fuel consumption as a function of oxygen mass fraction of the inducted mixture, at 1500 rpm and 100% load, for (i) NEIM and (ii) EGR operating modes.

As far as the effect of EGR on specific NO emissions is concerned, it is revealed that the increase of EGR percentage results also in a decrease of specific NO emissions. This may be attributed to the delayed, relative to TDC, initiation of combustion due to the increase of the ignition delay period. Furthermore, the increase of EGR percentage results to lower charge temperature caused by the higher specific heat capacity of the cylinder charge and, moreover, it leads to a reduction of the oxygen availability in the cylinder charge. The aforementioned parameters restrain the NO formation mechanism. By examining figures 11A-B it is revealed that for high load examined, NO emissions seems to be more sensitive to EGR rather than to nitrogen enrichment of the inducted air. Inferentially, by comparing the results obtained from both strategies examined, it is revealed that for an existent SI engine, running at high load, the curtailment of the emitted NO without serious deterioration of engine efficiency may be achieved with nitrogen enrichment of the inducted air instead of using EGR.

Figures 12A-B show the variation of the calculated specific CO emissions as a function of the oxygen mass fraction of the inducted mixture. The results correspond to 65% and 100% of full engine load conditions, for two strategies examined i.e. nitrogen enrichment and EGR, at 1500 rpm engine speed. In the same figures predictions for the normal engine operating point are also given. As known [2-4], CO formation rate depends on the relative air/fuel ratio, the unburned gaseous fuel availability and the cylinder charge temperature. The latter two parameters control the rate of fuel decomposition and oxidation [2-4].

Observing figures 12A-B, it is revealed that the decrease of oxygen mass fraction of the inducted mixture using nitrogen enrichment results in a negligible variation of CO emissions. Specifically, the increase of nitrogen concentration in the charge mixture causes a slight reduction of the total air/fuel ratio. This leads to a negligible effect on both CO formation and

oxidation rates, due to the decreased charge temperature. Thus, the emitted CO concentrations observed under NEIA operating mode seem to be almost the same with the respective ones observed under normal engine operating mode. On the other hand, the increase of EGR percentage results to an increase of CO emissions. Specifically, the increase of EGR percentage causes an increase of the ignition delay period, which suppresses the progress of the gaseous fuel combustion process, a situation that affects negatively (i.e. increase) the emitted carbon monoxide. On the other hand, the increase of EGR percentage promotes slightly CO oxidation rate, due to the lower total air-fuel excess ratio, which leads to a slight acceleration of the flame front and, thus, to a slight improvement of the gaseous fuel combustion rate. Nonetheless, the aforementioned improvement contributes insignificantly to the reduction of the emitted CO, since it occurs late. Observing the results, it is revealed that for high engine operating point the effect of EGR on CO emissions is more intense compared to the respective effect caused by the nitrogen enrichment of the inducted air.

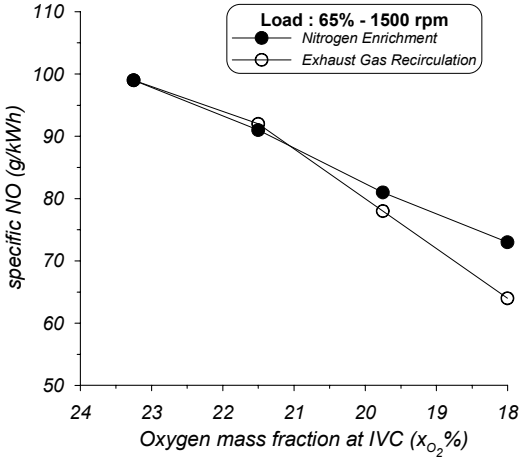

FIGURE 11A. Specific NO concentration as a function of oxygen mass fraction of the inducted mixture, at 1500 rpm and 65% load, for (i) NEIM and (ii) EGR operating modes.

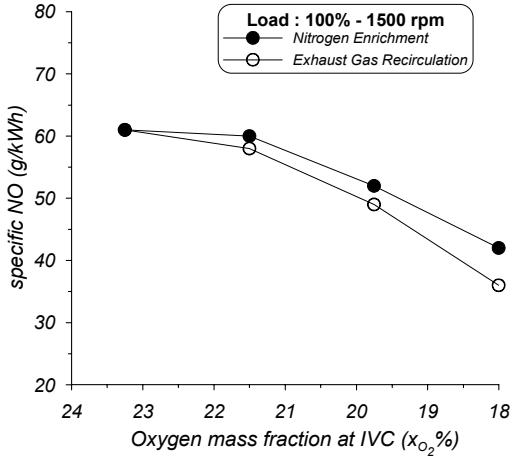

FIGURE 11B. Specific NO concentration as a function of oxygen mass fraction of the inducted mixture, at 1500 rpm and 100% load, for (i) NEIM and (ii) EGR operating modes.

CONCLUSIONS

In the present work, an existing two-zone phenomenological model has been used to examine the effect of (i) nitrogen enrichment of the inducted air and (ii) EGR, on performance characteristics and pollutant emissions of a natural gas spark ignited engine. A good coincidence between calculated and measured values under normal composition of the inducted air (NIA) operation was observed for performance characteristics, NO and CO emissions. Specifically, the model predicts with reasonable accuracy the absolute values but most important it predicts the trends of the combustion and pollutants formation mechanisms with various engine operating parameters.

Acknowledging the predictive ability of the two-zone combustion model, it was used to examine the effect of the aforementioned strategies on engine performance parameters, NO and CO emissions. From the evaluation of the theoretical findings, the following conclusions can be summarized as below:

- the increase of nitrogen mass fraction in the inducted mixture, results to:
  - deterioration of engine efficiency. The effect is more evident at intermediate load and high N_2 mass fractions in the inducted mixture.

- decrease of the maximum cylinder pressure, which at high N_2 mass fractions in the inducted mixture is up to 8%.
- decrease of the specific NO concentration. The effect is more evident at high N_2 mass fractions in the inducted mixture for both loads examined.
- an almost negligible variation of the specific CO concentration.

- the increase of EGR percentage, results to:
  - deterioration of engine efficiency. The effect is more evident at high load and high EGR percentages.
  - decrease of the maximum cylinder pressure, which at high EGR percentage is up to 12%.
  - decrease of the specific NO concentration. The effect is more evident at high load and high EGR percentages.
  - increase of the specific CO concentration. At high load and high EGR percentage the specific increase is up to 30%.

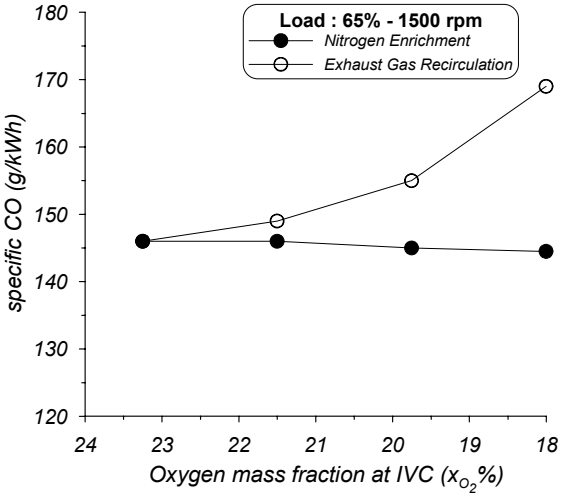

FIGURE 12A. Specific CO concentration as a function of oxygen mass fraction of the inducted mixture, at 1500 rpm and 65% load, for (i) NEIM and (ii) EGR operating modes.

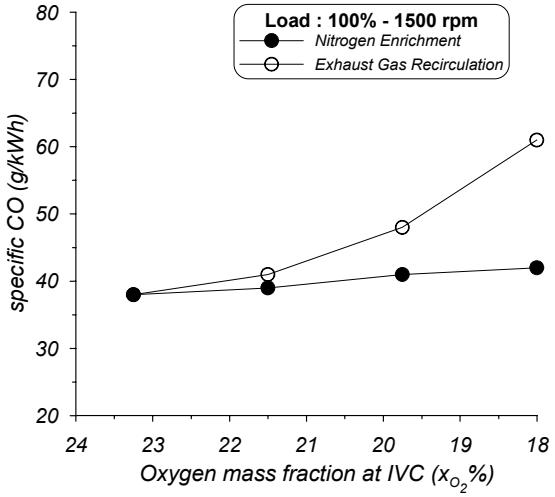

FIGURE 12B. Specific CO concentration as a function of oxygen mass fraction of the inducted mixture, at 1500 rpm and 100% load, for (i) NEIM and (ii) EGR operating modes.

In general, the increase of nitrogen percentage in the inducted mixture could be a promising solution for reducing NO emissions as compared to EGR. At low percentages, the specific strategy does not bring serious problems to engine performance characteristics. However, at high engine loads, the excessive increase of the nitrogen enrichment percentage beyond a certain limit may be proven to be harmful to engine performance characteristics (i.e. brake efficiency, engine power output). At the same time, the simultaneous increase of both parameters, at both low and high engine load conditions, does not bring any serious problem to engine operational lifetime, since the maximum cylinder pressure is lower compared to the respective one observed under normal engine operation. The results of this preliminary investigation are encouraging and urge us to prolong our theoretical investigation to examine the combined effect of other engine parameters (i.e. ignition timing, etc) on performance characteristics of an existing spark-ignited engine fuelled with natural gas. This is currently under progress and results will be given in the near future. Even though it is difficult to generalize the findings of the current preliminary investigation, we believe that they are important since the reduction of NO emissions on existing SI natural gas engines is extremely important.

REFERENCES

1. Korakianitis T, Namasivayam AM, Crookes RJ. Natural-gas fueled spark-ignition (SI) and compression-ignition (CI) engine performance and emissions. Prog Energy Combust Sci 2011;37:89-112.
2. Heywood J.B. Internal Combustion Engine Fundamentals. New York: McGraw–Hill, 1988.
3. Ferguson, C.R. Internal Combustion Engines – Applied Thermosciences, John Wiley, New York, 1986
4. Benson, R.S. and Whitehouse, N.D. Internal Combustion Engines, Pergamon Press, Oxford, 1979
5. Karim, G.A. and Ali, I.A. Combustion, knock and emission characteristics of a natural gas fuelled spark ignition engine with particular reference to low intake temperature conditions, Proceedings of the Institute of Mechanical Engineers, Vol. 189, pp.139–147, 1975.
6. Krishnan S.R., Biruduganti M., Mo Y., Bell S.R., Midkiff K.C., Performance and Heat Release Analysis of a Pilot-Ignited Natural Gas Engine. J. of Engine Research 2002;3:171-183.
7. Srinivasan K.K., Krishnan S.R., Midkiff K.C., Improving Low Load Combustion, Stability and Emissions in Pilot-Ignited Natural Gas Engines. In Proceedings of IMechE 2006, J. of Automobile Engineering 2006;220:229-239.
8. Liss, W.E. and Thrasher, W.H., Natural Gas as a Stationary Engine and Vehicular Fuel, SAE Paper No 912364.
9. Unich, A., Bata, R.M. and Lyons, D.W., Natural Gas: A Promising Fuel for I.C. Engines, SAE Paper No 930929.
10. Poola R.B., Stork, K.C., Sekar, R.R., Callaghan, K. and Nemser, S., Variable Air Composition With Air Seperation Membrane: A New Low Emissions Tool for Combustion Engines, SAE Transactions, 1998, 106, pp. 332-346.
11. Wong, H.C., Beck, N.J. and Chen, S.K., The Evolution of Compression Ignition Natural Gas Engines for Low Emission Vehicles, 2000, ASME Paper No 2000-ICE-318.
12. Biruduganti, M., Gupta, S. and Sekar, R., Low Temperature Combustion Using Nitrogen Enrichment to Mitigate NOx from Large Bore Natural Gas Fuelled Engines, ASME Paper No ICES2008-1616.
13. Biruduganti, M., Gupta, S., McConnel, S. and Sekar, R., Nitrogen Enriched Combustion of a Natural Gas Engine to Reduce NOx Emissions, ASME Paper No ICEF2004-843.
14. Papagiannakis R.G., Rakopoulos C.D., Hountalas D.T and Giakoumis E.G., Study of the performance and exhaust emissions of a spark-ignited engine operating on syngas fuel, Int. J. Alternative Propulsion, Vol. 1, No. 2/3, 2007
15. GE Jenbacher – Technical Report Laminar Flame Speed versus Air Fuel Ratio – Experience in Woodgas Plants, June 2005, Jenbach, Austria.
16. Papagiannakis R.G., Zannis T.C., Hountalas D.T. and Kotsiopoulos P.N., Study of Performance and Exhaust Emissions of a Spark-Ignited Engine operating with Nitrogen Enrichment of Intake Air, ECOS Paper, 2011.
17. Srinivasan K. K., Krishnan S. R., Qi Y., Midkiff K. C. and Yang H.., Analysis of diesel pilot-ignited natural gas low temperature combustion with hot exhaust gas recirculation. Journal of Combustion Science and Technology, 2007, 179:9,1737 -1776
18. Pirouzpanah V. , Khoshbakhti Saray R, Sohrabi A. and Niaei A.., Comparison of thermal and radical effects of EGR gases on combustion process in dual fuel engines at part loads, J. of Energy Conversion and Management, 2007, 48, 1909-1918
19. Pirouzpanah V., Khoshbakhti Sarai R.., Reduction of emissions in an automotive direct injection diesel engine dual-fuelled with natural gas by using variable exhaust gas recirculation. Proc. Instn Mech. Engrs Part D: J. Automobile Engineering, 2003, 217, 719-725.
20. Krishnan, S.R., Srinivasan, K.K., Singh, S., Bell, S.R., Midkiff, K.C., Gong, W., Fiveland, S. and Willi, M., Strategies for reduced NOx emissions in pilot-ignited natural gas engines., ASME-WA Meeting, Proc. ICEF, 2002, 39, 361-367.
21. Kusaka J., Okamoto T., Daisho Y., Kihara R., Saito T., Combustion and exhaust gas emission characteristics of a diesel engine dual- fueled with natural gas. Society of Automotive Engineers of Japan, Inc. and Elsevier Science, JSAE Review, 2000, 21, 489-496
22. Ishida M, Tagai T, Ueki H. Effect of EGR and preheating on natural gas combustion assisted with gas-oil in a diesel engine. JSME Int J, 2003;46:124-30.

23. Abd Alla GH. Using exhaust gas recirculation in internal combustion engines: a review. Energy Convers Manage, 2002, 43:1027-42.
24. Blizard, N.C. and Keck, J.C. Experimental and Theoretical Investigation of Turbulent Burning Model for Internal Combustion Engines, SAE Paper No. 740191.
25. Lucas, G.G. and James, E.H., Computer Simulation of a Spark Ignition Engine, SAE Paper No. 730053.
26. Lavoie, G. Correlations of Combustion Data for a SI Engine Calculations-Laminar Flame Speed, Quench Distance and Global Reaction Rates, SAE Paper No. 780229.
27. Bayraktar H. Experimental and theoretical investigation of using gasoline-ethanol blends in spark ignition engines. J. of Renewable Energy 30, 11, pp. 1733-1747, 2005.
28. Annand, W.J.D. Geometry of spherical flame propagation in a disc-shaped combustion chamber, Journal of Mechanical Engineering Science, Vol. 12, pp.146–149, 1970.
29. Annand, W.J.D. Heat transfer in the cylinders of reciprocating internal combustion engines, Proceedings of the Institute of Mechanical Engineers, Vol. 177, pp.973–990, 1963
30. Vickland, C.W., Strange, F.M., Bell, R.A. and Starkman, E.S. A consideration of the high temperature thermodynamics of internal combustion engines, Transactions of the SAE, Vol. 70, pp.785–793, 1962
31. Lavoie, G.A., Heywood, J.B. and Keck, J.C. Experimental and theoretical study of nitric oxide formation in internal combustion engines, Combustion Science and Technology, Vol. 1, pp.313–326, 1970
32. Al-Himyary TJ, Karim GA. A correlation for the burning velocity of methane – Air mixtures at high pressures and temperatures. ASME Trans, J Eng Gas Turbines Power 1987;109:439-42.

ISSN: 1791-4469 Copyright © 2012 Hellenic Naval Academy

Feasibility Analysis on a Steam Rankine Cycle to Recover Heat from a Gas Turbine used on a Naval Vessel

Efthimios G. Pariotis*, Ioannis Katsanis and Ioannis Roumeliotis

Laboratory of Naval Propulsion Systems, Section of Naval Architecture and Marine Engineering, Department of Naval Sciences, Hellenic Naval Academy, End of Hatzikiriakou Ave., 18539 Piraeus, Greece
pariotis@snd.edu.gr, Tel.: +30 210 4581663; Fax: +30 211 7701574.

Abstract. The design concept of some special purpose naval vessels requires the usage of gas turbines as prime mover engines, which offer high power density and high flexibility on the variation of the engine load. However, one of the disadvantages of the gas turbines compared to their main competitors, the diesel engines, is their lower fuel efficiency. The comparison becomes ever worse when referring to the part load engine conditions, especially for the legacy gas turbines installed in some vessels of the Hellenic Navy. The part load operation is of paramount importance for the case of marine propulsion, since the engines operate most of the time at part load. Apart from the economic impact of the relatively high fuel consumption of the installed gas turbines, there are also operational issues that arise and have to be considered. The engine's fuel consumption affects the planning of the required fuel supply chain and the operational range of the vessel. In the present study, a preliminary feasibility analysis of installing a waste heat recovery bottoming Rankine cycle with steam as a working medium is conducted, in order to estimate the improvement of the fuel consumption over the entire operating range for a gas turbine used as a base prime mover at the Hellenic Navy. For this purpose, a gas turbine performance model is used to calculate the flue gas properties (temperature and mass flow rate) during the engine off-design operation and is coupled with a thermodynamic model that simulates the Rankine cycle and predicts the thermodynamic properties of water/steam at all operating conditions. The analysis takes into account constraints regarding the available space for installing the various components and especially the exhaust gas heat exchanger (HRSG), as well as the lower limit of the exhaust gas temperature to avoid condensation. From this preliminary investigation it has been confirmed that with the proposed configuration, a significant improvement on the overall (combined) efficiency can be obtained ranging from 33% at full power to 53% at 25% of the gas turbine load, providing a technically feasible solution to the problem of low gas turbine engine efficiency, especially at part load operation. Moreover, at the same time, this technique provides tactical benefits, since it lowers the exhaust gas temperature which consequently affects the infrared "signature" of the ship, making its tracking by the enemy harder.

Keywords: Gas Turbines, Waste heat recovery, Steam Rankine cycle, COGAS.

INTRODUCTION

The classical heat engine cycles for power generation in steam and gas turbine plants are those associated with the names of Rankine and Joule-Brayton [1]. The temperature-entropy diagrams for these cycles are shown in Figs. 1A and 1B respectively. The Rankine cycle is the basis of steam power plant, with steady flow through a boiler, a turbine driving a generator delivering electrical or mechanical power, a condenser and a feed-pump. The Joule-Brayton constant pressure cycle is the basis of the gas turbine power plant, with steady flow of air (or gas) through a compressor, the heater, the turbine, and the cooler within a closed circuit. The turbine drives both the compressor and the generator delivering electrical power or provides mechanical power on a power shaft.

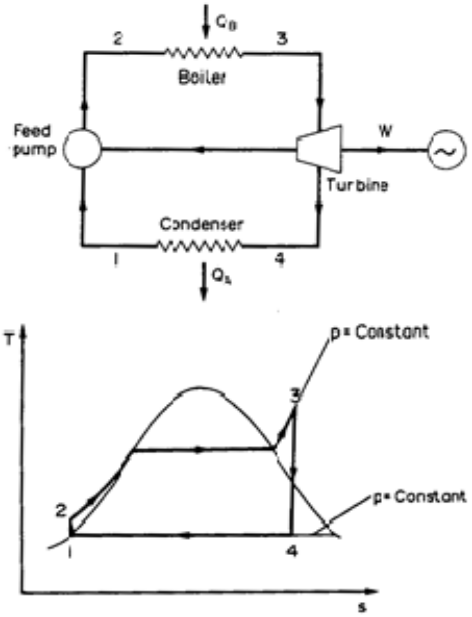

FIGURE 2A. Rankine cyclic heat engine [1]

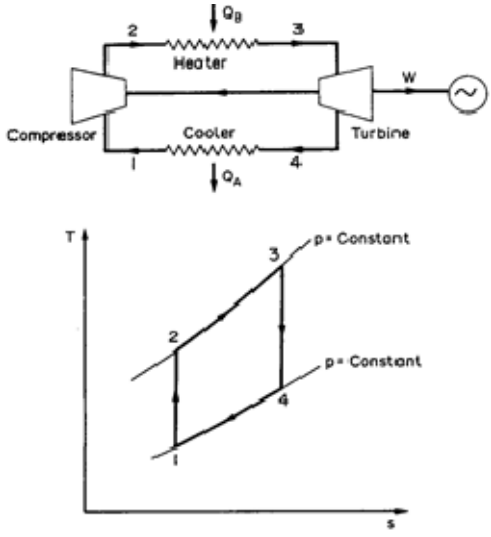

FIGURE 1B. Joule – Brayton cyclic heat engine [1]

One particularly important field of study for conventional power plant design is that of the "combined plant". A broad definition of the conventional "combined cycles" is the cycles that are coupled to work together, in such a way that the heat rejected from the one power cycle (as dictated by the 2nd Law of thermodynamics) which is called upper or topping cycle, becomes the heat source for the other which is called lower or bottoming cycle, in order to produce more useful power. In practice the "upper" plant is often open circuit, not cyclic. In this way it becomes feasible to produce greater work output for a given heat (or fuel energy) supply, i.e. improved energy efficiency. Using the second Law of Thermodynamics it is proved that the maximum efficiency of a heat engine is achieved when it is operated according to the reversible Carnot cycle between a given (maximum) constant temperature (T_B) of heat supply (Q_B) and a given (minimum) temperature (T_A) of heat rejection (Q_A) (according to the temperature –entropy diagram shown in Fig. 2). Its thermal efficiency is given by the following expression:

$$\eta_{TH} = \frac{W}{Q_B} = \frac{Q_B - Q_A}{Q_B} = \frac{T_B \Delta S - T_A \Delta S}{T_B \Delta S} = \frac{T_B - T_A}{T_B} \qquad (1)$$

Increasing the high temperature (T_B) or reducing the low temperature of the cycle (T_A) leads to higher energy efficiency. Although in practice it is not feasible to develop an engine working based on the Carnot cycle, this thermodynamic cycle is treated as the measure of excellence when studying power producing cycles under given boundary conditions (i.e. given temperatures of the “hot” source and the “cold” sink) .

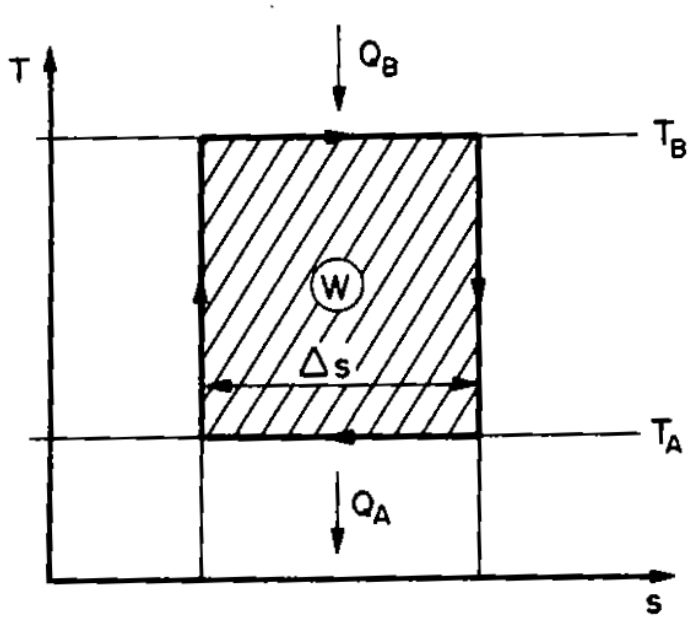

FIGURE 2. Typical Temperature-entropy diagram for a Carnot power plant

There are two features of the Carnot power plant which are responsible for its maximum thermal efficiency [1]:

- all process involved are reversible;
- all heat is supplied at the maximum (specified) temperature (T_B) and all heat is rejected at the lowest (specified) temperature (T_A).

In an attempt to achieve high thermal efficiency, the designer of a conventional power plant investigates alternative ways to raise T_B and lower T_A. In Fig. 3 it is shown how this affects the (Rankine) steam power plant. Firstly, lower rejection temperature (T_A) is achieved by lowering condenser pressure, and it is an important feature of the cycle that all heat is rejected at the lowest temperature.

Secondly, efforts are made to raise the mean temperature of heat supply T_B temperature, by

- raising the boiler pressure;
- reheating between turbine blades
- feed heating (bleeding steam from the turbine to heat the condensate before it is fed to the boiler plant

Whether such modifications to achieve increased thermal efficiency justify the extra capital required is a matter for economic study; thermodynamics is not always the sole criterion. In this search for higher efficiency, the designer of the conventional power plant is maximizing the work output (W) for a given heat supply (Q_B).

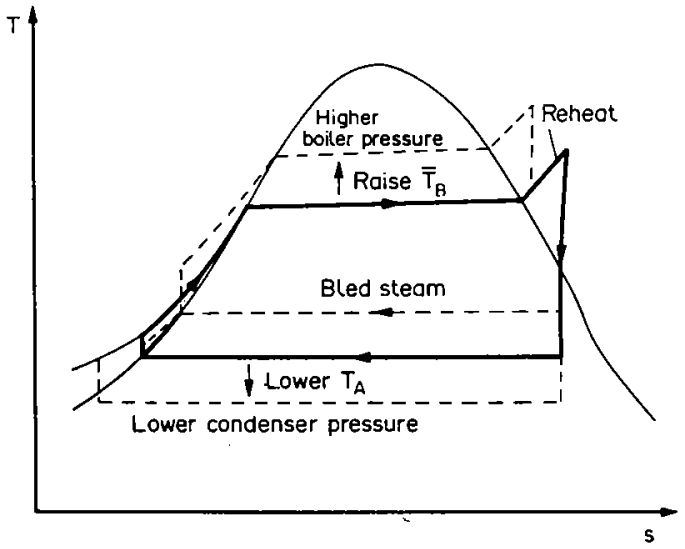

FIGURE 3. Common Modifications of the basic Rankine cycle to increase thermal efficiency

In the design process of a combined cycle power plant, the objective is to optimize the overall system performance, which sometimes does not directly mean that each of the system's components (upper and lower cycle) operate at their most effective operating conditions [2, 3, 4]. To make this clearer, consider a combined power plant, consisted by two separate power plants (H and L) combined as shown in Fig. 4. Heat rejected (Q_{HL}) from the ''higher'' (topping) plant (H), with a thermal efficiency η_H, is used to the lower (bottoming) plant L (as a heat source), which operate with a thermal efficiency η_L. The two plants may use different working mediums. The work output from the lower cycle is

$$W_L = \eta_L Q_{HL} \tag{2}$$

But

$$Q_{HL} = Q_B(1-\eta_H) \tag{3}$$

where Q_B is the heat supplied to the upper plant, which delivers work

$$W_H = \eta_H Q_B \tag{4}$$

Thus the total work output is

$$W = W_H + W_L = \eta_H Q_B + \eta_L(1-\eta_H)Q_B = Q_B(\eta_H + \eta_L - \eta_H\eta_L) \tag{5}$$

The thermal efficiency of the combined plant is therefore

$$\eta_{TH} = \frac{W}{Q_B} = \eta_H + \eta_L - \eta_H\eta_L = \eta_H + \eta_L(1-\eta_H) \tag{6}$$

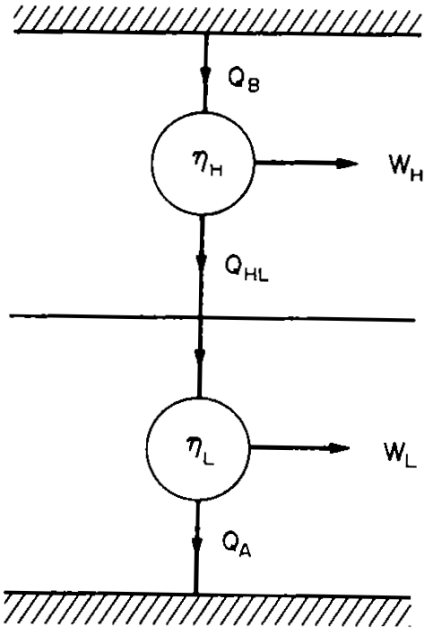

FIGURE 4. Combined power plant

The advantages are clear. The basic efficiency of the upper cycle has been increased by: $\eta_L(1-\eta_H)$, using its rejected heat to generate power in the lower cycle.

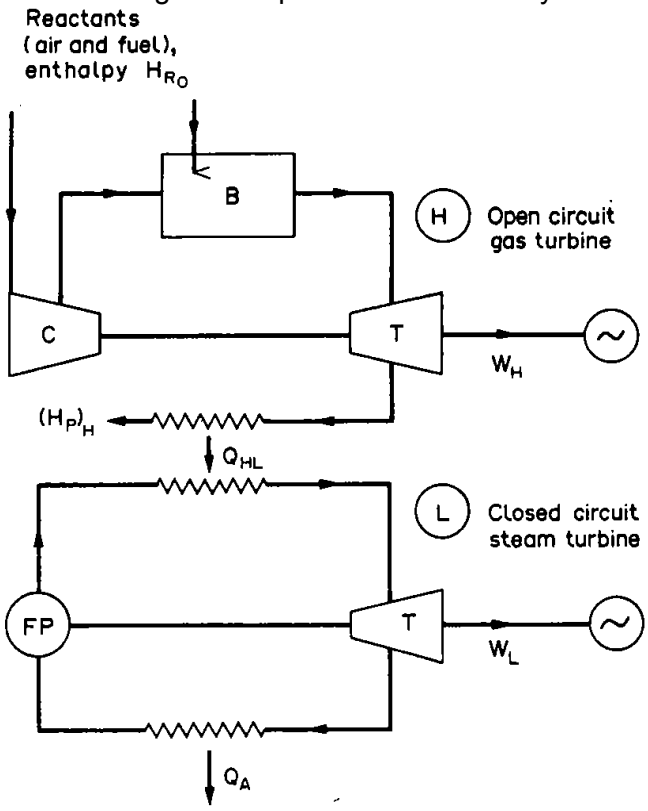

FIGURE 5. Gas turbine/steam turbine combined power plant

When the upper cycle is consisted by a gas turbine, one of the most familiar ways to further exploit the energy of the exhaust gases is to combine the upper cycle with a bottom Rankine cycle equipped with a steam turbine. A typical configuration is the one shown in figure 5. The combination of an open cycle gas turbine with a water/steam cycle, commonly known as the combined cycle, offers several advantages [4, 5]:

- Air/Exhaust gas is a straightforward medium that can be used in modern gas turbines at high turbine inlet temperature levels (above 1200°C), providing the optimum prerequisites for a good topping cycle.
- Steam/water is inexpensive, widely available, non-hazardous, and suitable for medium and low temperature ranges, being ideal for the bottoming cycle.

In this case the combined efficiency of the plant can be expressed by the following equation:

$$\eta_{CC} = \frac{\eta_{GT}\dot{Q}_{GT} + \eta_{ST}\dot{Q}_{GT}(1-\eta_{GT})}{\dot{Q}_{GT}} = \eta_{GT} + \eta_{ST}(1-\eta_{GT}) \quad (7)$$

Differentiation makes it possible to estimate how the overall combined plant efficiency is affected by a change in the efficiency of the gas turbine:

$$\frac{\theta\eta_{CC}}{\theta\eta_{GT}} = 1 + \frac{\theta\eta_{ST}}{\theta\eta_{GT}(1-\eta_{GT})} - \eta_{ST} \quad (8)$$

Thus, increasing the gas turbine efficiency improves the overall efficiency only if:

$$\frac{\theta\eta_{CC}}{\theta\eta_{GT}} > 0 \quad (9)$$

which leads to:

$$-\frac{\theta\eta_{ST}}{\theta\eta_{GT}} < \frac{1-\eta_{ST}}{1-\eta_{GT}} \quad (10)$$

The last equation shows that improving the gas turbine efficiency is helpful only if it does not cause a high drop in the efficiency of the bottoming cycle (n_{ST}). Table 1 indicates that when the efficiency of the gas turbine is raised, there is a limit on the allowable decrease of the bottom rankine cycle efficiency, in order this to have a positive effect on the overall combined cycle efficiency. For example, steam process efficiency can be reduced from 30% to 27.8% ($\frac{\theta\eta_{ST}}{\theta\eta_{GT}} = \frac{27.8-30}{35-30} =$ in case the gas turbine efficiency is raised from 30% to 35% to keep the overall combined-cycle efficiency.

TABLE 1. Example of the allowable reduction in the bottoming cycle efficiency n_{ST} when the gas turbine efficiency n_{GT} increases from 30% to 35% or 40%, in order to keep the overall combined-cycle efficiency.

η_{GT}	0.3	0.35	0.4
$-\frac{\theta\eta_{ST}}{\theta\eta_{GT}}$	1.0	1.08	1.17

IMPLEMENTATION OF A COMBINED CYCLE FOR MARINE APPLICATIONS

The recent changes in the emission legislation with the burdens on the maximum content of sulfur in the marine fuels, as well as, the inherent advantages of the gas turbines as prime movers, together with the development of advanced systems with high overall efficiency, have grown the interest regarding the usage of gas turbines as prime movers for vessels instead of using diesel engines [4, 6, 7, 8, 9]. Especially for the navy, gas turbines offer high flexibility on the operating conditions, low demand in maintenance and high power density, which make them ideal for specific types of vessels (i.e. combatants) [10]. However, the operational demands and the growing fuel prices have raised skepticism regarding the relatively low overall engine efficiency of the gas turbines used in the Hellenic Navy, as well as in the foreign Navies worldwide. One of the solutions proposed is the modification of the existing gas turbine power plants, by adding a bottoming cycle (Rankine) working with steam/water in order to recover a portion of the heat rejected to the environment with the exhaust gases. This excess power could be offered to cover a portion of the electric loads of the ship (reducing the fuel consumption of the auxiliary engines), or could be provided as propulsion power through an appropriate gear box. The US Navy has studied such alternatives since the 80s and the conclusions derived are positives [10].

In the present work a preliminary investigation is conducted in order to explore the feasibility of adding a bottom cycle (i.e. Rankine with steam as the working medium) to the existing gas turbine configuration which is used as the basic propulsive power unit on a combatant vessel of the Hellenic Navy. In this first part of our research work, the investigation is limited to the determination of the possible power increment and the corresponding improvement of the overall system efficiency taking into account specific limitations which exist, regarding the allowable lower exhaust gas temperature and the dimensions of the heat exchanger used for the exhaust gas heat recovery (Heat Recovery Steam Generator, i.e. HRSG).

Gas Turbine Model

In order to model the off – design operation of the gas turbine a generic, zero-dimensional non-linear adaptive performance model is used [12]. The model is based on the logic that a gas turbine is an assembly of different components (modules). Each component is identified and modelled according to the kind of aero-thermodynamic process it materializes. For each component, if $\boldsymbol{Y}_{IN}$ is the vector of the independent variables at its inlet and $\boldsymbol{Y}_{OUT}$ the corresponding vector at its outlet, then in order to find the values at the component exit an equation of the following form must be solved.

$$g(\bar{Y}_{IN},\bar{Y}_{OUT})=0 \tag{11}$$

This equation usually derives from conservation laws, as well as from existing experience in components operation. It may consist of analytical relations, possibly including empirical constants (e.g. duct pressure loss), or a set of curves (e.g. turbo-machinery component maps). Additional equations express the compatibility of operation between the different components, imposing “matching” conditions, as for example, power balance between the high pressure turbine and compressor. In this way a set of equations, which have to be simultaneously satisfied by the fluid parameters, is formed. The solution of this system of equations, non-linear in nature, is achieved numerically. Different types of numerical techniques can be employed, as

for example described by Stamatis et al. [13]. The solution of this system of equations, for an operating point as specified by the ambient conditions and the selected engine control variable (e.g. engine load, Turbine Entry Temperature etc.), gives the full cycle details, and the performance parameters are uniquely defined for off-design operation.

The model is capable of simulating all existing gas turbine configurations from single shaft engines, up to a three spool engines with power turbine with intercooling, reheating, recuperation and water injection at various positions along the engine. The model layout and the system of equations to be solved are modified in accordance with the engine configuration under consideration. Also, as the control variable of different engines may be different, or even change throughout their operation, the model is capable to acknowledge several parameters as control variables like Turbine Entry Temperature (TET), Compressor Discharge Pressure (CDP), load etc. depending on the engine configuration.

In order to be capable to simulate a specific engine the model can be adapted to available, engine specific data by employing the adaptive modelling technique, introduced by Stamatis et al. [14]. The basic idea behind adaptive modelling is that component characteristics (e.g compressor map) are allowed to change through appropriate modification factors. The values of these factors are determined by requiring that available engine performance data are matched by the engine model. In this way, at the end of the adaptation procedure, a set of components characteristics is produced which are capable to reproduce the specified engine operation with great accuracy (e.g Tsalavoutas et al. [15]).

The gas turbine selected as a test case in the present study, is a twin spool – three shaft engine of 4MW nominal power and a corresponding thermal efficiency of 29.4%. This engine type is used as the cruising engine (two engines of this type) of a specific marine vessel type of the Hellenic Navy, in a COGOG configuration. Due to the fact that the majority of the vessel's operational duty is covered by the cruising gas turbines, this engine type is used for the investigation of the exhaust gas heat recovery technique.

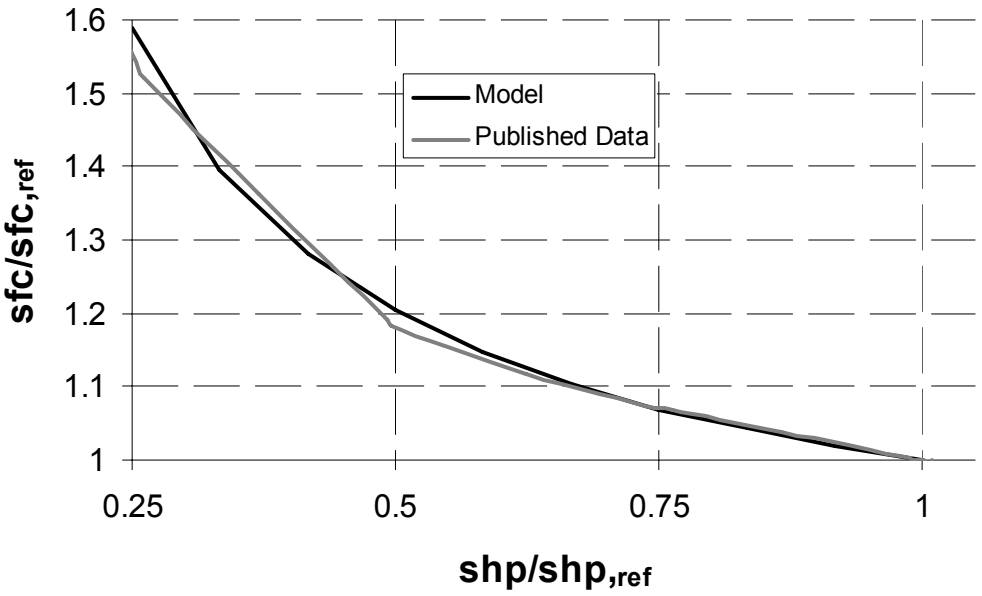

FIGURE 6. Predicted and published values [15] of the gas turbine versus load.

In order to build a reliable model capable to predict the engine's off-design operation, the model has been adapted to available data. The results presented by Tsalavoutas et al. [15] indicate that the model can simulate the off-design operation of the engine with good accuracy. The calculated by the model specific fuel consumption (sfc) compared with published values [15]

versus the operating load is presented in Figure 6. The adapted model is used for calculating the exhaust flow properties (mass flow, temperature and composition) at specific operating points.

Heat Recovery Steam Generator Design

One of the most important parts of the Rankine cycle is the heat recovery steam generator (HRSG) since it is the component of the cycle which is responsible for the exhaust heat recovery (and the production of steam, with adequate thermodynamic properties). This component of the bottoming cycle contributes considerably to the system's weight and volume. These two parameters are crucial for marine applications in general and even more crucial when the application concerns a naval vessel. In general there are two types of Heat recovery steam generators (HRSG): The once-through type and the drum-type.

In drum-type HRSGs the water/steam separation and water retention is conducted in a steam drum. A HRSG of drum-type can be built in two basic constructions, based on the direction of the gas turbine exhaust flow through the boiler: vertical HRSG and horizontal HRSG [2] as shown in Figure 7. In vertical designs, the heat transfer tubes are horizontal, suspended from uncooled tube supports located in the gas path. Often this design requires circulating pumps in order to assure constant circulation within the evaporator (that's why often they are called forced-circulation HRSGs). In a horizontal design, the circulation through the evaporator takes place entirely by gravity, based on the density difference of water and boiling water mixtures (often called natural-circulation HRSG). The heat transfer tubes are vertical, and essentially self-supporting. Earlier the vertical designs had several advantages compared with horizontal designs, with respect to space requirement and start-up performance. However, the natural-circulation HRSGs have been improved, and current designs offer performance comparable with the forced-circulation designs [2].

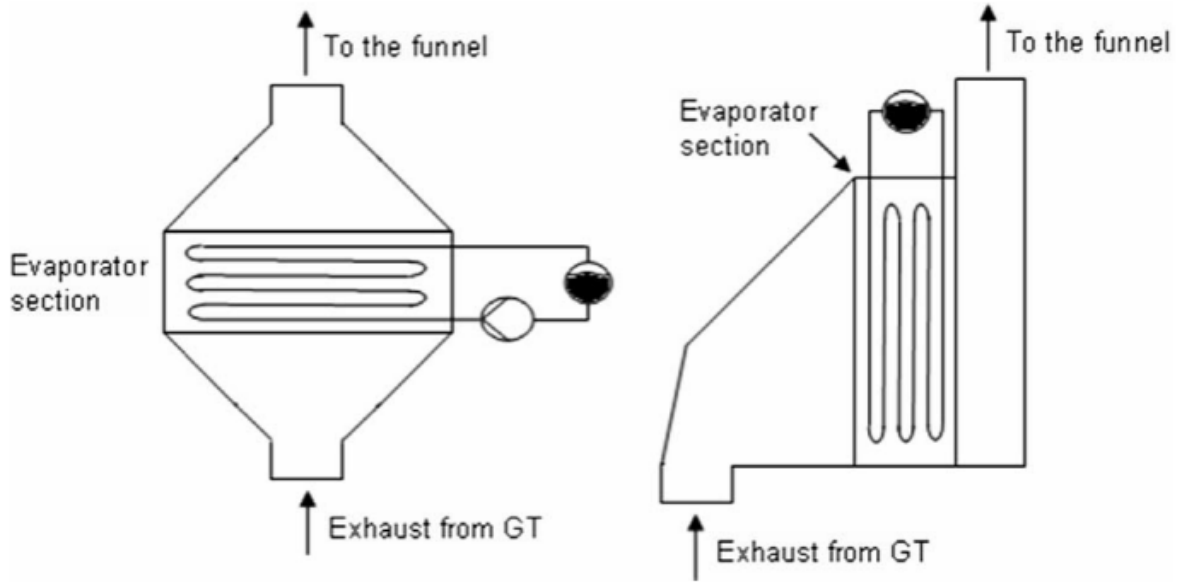

FIGURE 7. Schematic figures of vertical (left) and horizontal (right) HRSGs [2].

Another feature that needs to be considered when selecting HRSG arrangement is whether a by-pass stack which permits the operation of the gas turbine without the HRSG (and steam turbine) in service is desirable. Such feature would increase the cost and occupy space. An

important drawback with the drum-type HRSG is that for high live-steam pressures the operational flexibility is restricted. Combined cycles used for marine applications are often operated in cycling duties with frequent load changes and start-up cycles. Such operation causes high thermal stresses on parts within the HRSG, especially on the drum. Thus, the loading rate, for example during start-up, is primarily constrained by the drum.

On the other hand a once-through HRSG is basically one tube, featuring the economizer, the evaporator and the super-heater. Water enters at one end and steam leaves at the other, eliminating the drum and circulation pumps. Since it contains no drum, it provides the desired high thermal flexibility. However, as all the water mass flow should evaporate when flowing through the HRSG, the area requirement of the evaporator section is large. In a HRSG of drum-type, the water is re-circulated and only a portion of the flow is evaporated at the time, thereby requiring less heat transferring area.

Previous work on the use of combined cycles for marine applications does not provide a coherent picture on the optimum choice of the HRSG type. Taking into account the space limitations which apply on a naval vessel, in this study a once-through heat exchanger is considered with vertical gas flow mounted directly over the gas turbine, as shown in figure 8. Such a design would minimize ground-floor and space requirements. Additionally, a vertical arrangement is associated with a low cost and it provides a good exhaust gas distribution across the boiler heating surfaces. On the other hand, this configuration may set some obstacles to the maintenance of the gas turbine, but taking into account the very limited available space this configuration seems to be the optimum solution.

In this HRSG, the feed water is introduced at the gas outlet and is moved through the core until it leaves the other end at the desired condition (superheated). The steam exit conditions are controlled by the feed-water flow rate. A low water flow rate produces high superheat, high minimum wall temperatures of the heat exchanger tubes and low heat recovery. This control feature is utilized in this study since focus has been given to maintain a minimum exhaust gas temperature at the exit of the boiler (economizer) above the sulfur-acid dew point. Specifically, this limit value was assumed equal to 135°C, which is slightly above the dew point of the specific gas turbine exhaust gas. It is noticed that in the Greek Navy the standard fuel used in the gas-turbine-powered combatants has a maximum sulfur content equal to 1% [16].

HRSG Design

To simplify the simulation procedure, the dimensions of the HRSG are calculated based on relevant studies which have already been conducted by the US Navy. Specifically the case study examined in [10] has been taken as a reference for the present work, where the bottom steam Rankine cycle has been applied on a LM2500 gas turbine which is used for propulsion of a combatant ship. Therefore the main design parameters of the HRSG used in the present study have been determined by appropriately scaling the corresponding data of this reference work. The HRSG has tubes with a nominal 3/4 inch diameter and nine fins per inch. These tubes are arranged in a staggered tube bank, while, no feed-water heating is considered, which means that the condenser water is fed directly to the economizer inlet. As far as the HRSG's dimensions, these are assumed to be proportional to the ones of the reference HRSG. Specifically, the height of the HRSG is set equal to 2.40m (which corresponds to the ship's deck-height), while the cross sectional area is determined so that the mean exhaust gas velocity at full engine load (4 MW), is identical to the one used in the aforementioned reference study. In this way, similar flow conditions are expected to exist, which makes the assumption of similar exhaust gas pressure losses and overall heat transfer conditions to be trustworthy. In the reference study the design exhaust gas flow rate is equal to 45.4 kg/s (corresponding to a power of 8.95 MW), and the dimensions of the boiler are: Length=2.7m, Width=2.7, Height=2.40m, with a total heat transfer area equal to 1230 m^2. Taking into account that at the present study, the

gas turbine's exhaust gas mass flow rate at full power is equal to 18.3 kg/h, it can be concluded that the corresponding dimensions of the assumed HRSG are: Length=1.71m, Width=1.71, Height=2.40m, with a total heat transfer area equal to 495,79 m^2.

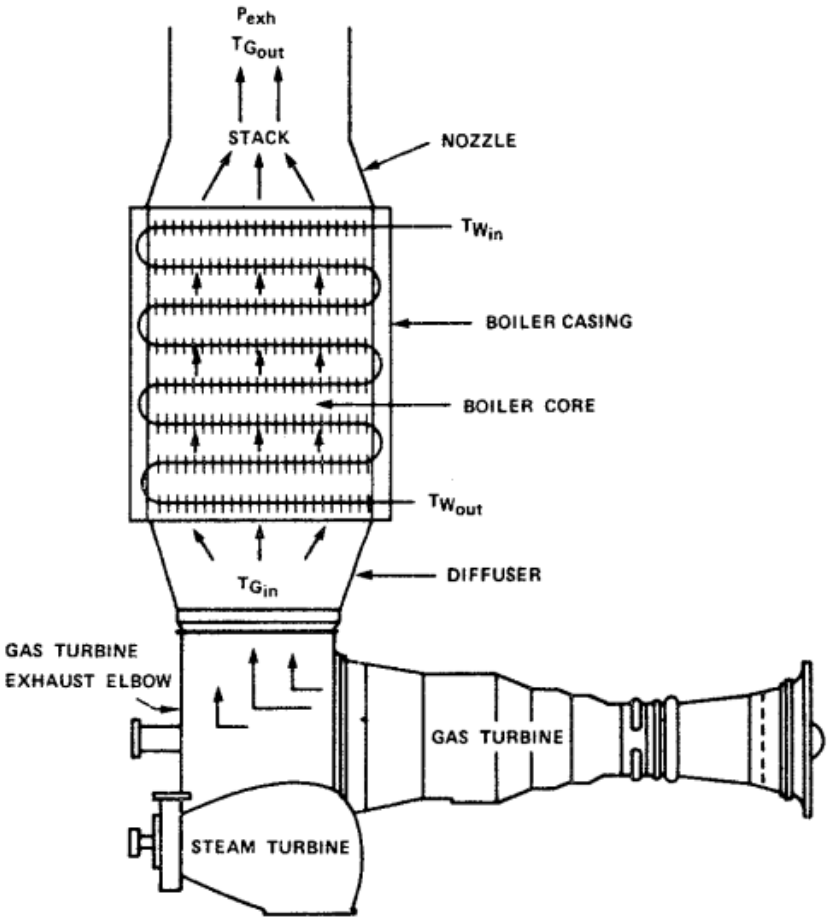

FIGURE 8. Schematic diagram of the once-through HRSG [10]

To further simplify the simulation procedure, the overall heat transfer coefficient U_{mean} from the gas side to water / steam, is assumed to be constant at the whole HRSG length and equal to the mean value of the one which has been calculated in the reference study [10] since the flow conditions of the two streams of working mediums and especially the ones corresponding to the gas-side, which possesses the higher resistance to the heat transfer are similar with the ones which apply to the present study. Thus, the overall heat transfer coefficient U_{mean} is assumed to be equal to 0.060 W/m2C [8, 10, 17].

Rankine Cycle Simulation Procedure

For this preliminary feasibility study a simple configuration of the combined power plant is examined, which comprises by: a Gas turbine power plant (following the Bryton cycle) and a simple Rankine cycle (bottom cycle), as shown in fig. 9.

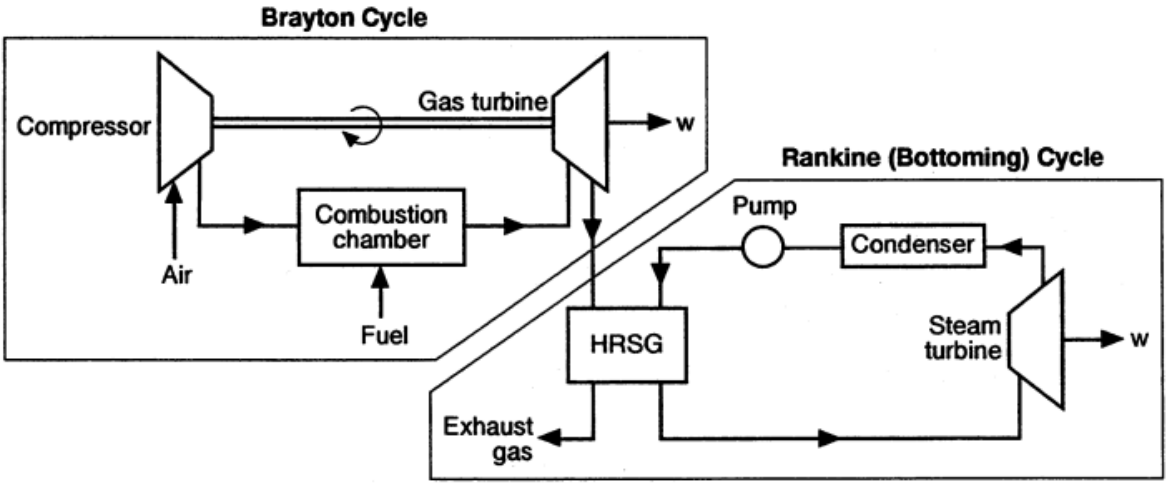

FIGURE 9. Configuration of the Combined Cycle examined (Gas-Turbine / Water-Steam Rankine Cycle)

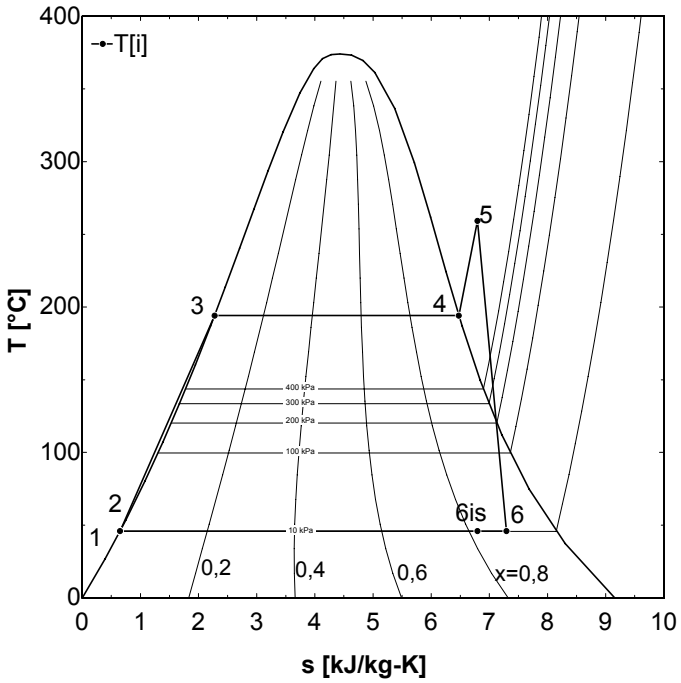

FIGURE 10. Thermodynamic processes of the Rankine cycle examined

This bottoming cycle is composed by four main components: a pump, a heat exchanger (HRSG), a steam turbine / generator and a condenser. As shown in fig. 10 the thermodynamic cycle for the steam/water working fluid considered, includes the following processes: a compression process in the pump (process 1-2), with an isentropic coefficient equal to $n_{is,p}$=0.90, an isobaric heat transfer process in the heat exchanger (processes 2-3-4-5), an expansion process through the steam turbine with an isentropic coefficient $n_{is,t}$=0.80 (process 5-6), and an isobaric heat transfer process in the condenser (process 6-1). The HRSG is assumed to be consisted by three parts: the economizer, the boiler and the super-heater (while these parts are considered to have “moving” boundaries depending on the operating conditions). The process (2-3) takes place in the economizer, the process (3-4) takes place in the boiler and the process (4-5) takes place in the super-heater. In the analysis conducted, it has been assumed

that the steam quality at point 6_{is} is equal to x_{limit}=0.82 [10], which ensures that problems associated with steam condensation at the late stages of the steam turbine are avoided.

The pump supplies the working fluid to the heat exchanger, where the working fluid is heated and vaporized removing heat from the exhaust gases. The working fluid leaves the heat exchanger in saturated or superheated state (in order to fulfill the criterion which has been set for the steam quality after the expansion in the steam turbine). The high enthalpy steam is then expanded in the expander (turbine), which provides additional power to the vessel (electric or propulsion). After the expander, the working fluid enters the condenser where it condensates (using another heat exchanger, utilizing the sea water as the medium to absorb the latent heat of water/steam condensation). Having this in mind, the condenser pressure has been set constant and equal to P_{cond}=10,1 kPa for all cases examined, so that a safe temperature difference between the working medium (water/steam) and the sea-water is ensured.

The mathematical model of the simple Rankine Cycle uses the thermodynamic energy conservation equations. The model considers a steady state operation with negligible kinetic and potential energy effects.

The pump power is given by the following equation:

$$Wp = \dot{m}_c * \left(h_2 - h_1\right) \tag{12}$$

The heat absorbed by the working fluid (steam) from the exhaust gases in the HRSG is given by:

$$\dot{Q}_{HRSG} = \dot{m}_c * (h_5 - h_2) \tag{13}$$

The turbine power is calculated using the following equation:

$$\dot{W}_{turbine} = \dot{m}_c * \left(h_5 - h_6\right) \tag{14}$$

while the isentropic coefficient of the steam turbine is assumed to be equal to $n_{t,is}$=0.80 and is defined as:

$$n_{t,is} = \frac{h_5 - h_6}{h_5 - h_{6,is}} \tag{15}$$

The total heat transfer rate from the exhaust gases to the Rankine working medium (water / steam), inside the HRSG is evaluated using the following equation:

$$\dot{Q}_{GT,gas} = \dot{m}_h * c_{p,gas} * \left(T_{h,in} - T_{h,out}\right) \tag{16}$$

Assuming that no heat losses occur at the HRSG, all the heat absorbed by the hot exhaust gas, is transferred to the water/steam, thus:

$$\dot{Q}_{HRSG} = \dot{Q}_{GT,gas} \tag{17}$$

Analogous expressions can be written for each part of the HRSG i.e. economizer, boiler and super-heater, through which the exhaust gas temperature at each part of the HRSG can be derived:

$$\dot{Q}_{ECON} = \dot{m}_c * (h_3 - h_2) = \dot{m}_h * c_{p,gas} * (T_{h,3} - T_{h,out}) \tag{18}$$

$$\dot{Q}_{BOILER} = \dot{m}_c * (h_4 - h_3) = \dot{m}_h * c_{p,gas} * (T_{h,2} - T_{h,3}) \tag{19}$$

$$\dot{Q}_{SUPERHTR} = \dot{m}_c * (h_5 - h_4) = \dot{m}_h * c_{p,gas} * (T_{h,in} - T_{h,2}) \tag{20}$$

The temperature ($T_{h,in}$) of the exhaust gas at the inlet of the HRSG, is an input parameter at each operating point examined, and is obtained using the adapted gas turbine performance model. In the following table 3, the properties of the exhaust gas at the HRSG's inlet are shown at the examined engine loads.

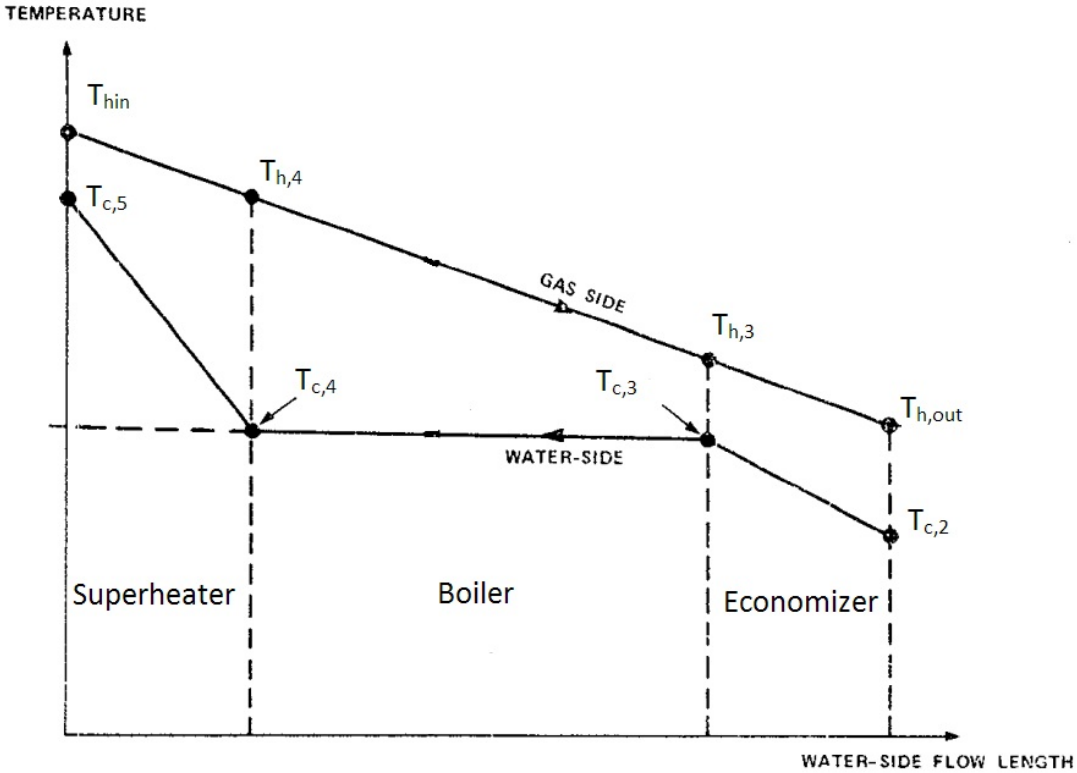

FIGURE 11. Temperature profile of the exhaust gas and water/steam inside the HRSG

As far as the outlet temperature ($T_{h,out}$) of the exhaust gas from the HRSG, a lower limit has been set to avoid gas condensation and the relevant problems due to the sulfur content of the fuel. In the present study the lowest acceptable temperature for the $T_{h,out}$ is set equal to 135 ^{o}C [10, 18] and is determined by solving the system of the equations already presented.

Finally, a minimum temperature difference has been assumed between the inlet gas temperature and the outlet steam temperature, which is equal to $(T_{hin}-T_{c,5})\geq 20\ ^{o}C$ [9], for all the operating conditions examined. Therefore the temperatures of the exhaust gas and water/steam at each part of the HRSG are predicted and the temperature profile of both streams is shown in fig.11. The last criterion used in the present study in order to solve the system of the aforementioned equations is related to the mass flow rate which passes through the steam turbine. It is known from the gas dynamics that a steam turbine behaves in a manner similar to a nozzle, which means that for a pressure ratio across the nozzle greater than approximately two (which is the case in the present study), the mass flow rate maximizes, the turbine is assumed chocked and the corrected mass flow $\frac{\dot{m}_c * \sqrt{T_0}}{P_0}$ takes a constant value, as shown in Fig.12 [19]. More specifically the turbine's mass flow rate is also influenced by the wheel-speed Mach number which is presented by: $N/\sqrt{T_0}$, thus a similar flow rate / pressure ratio relationship is experienced as shown in fig. 13, where, $\vartheta = T_0/T_{ref}$ and $\delta = P_0/P_{ref}$. Since the effect of the corrected rotational speed is relatively small and there are no extractions it can be assumed that the steam turbine operates at a specific corrected mass flow for the whole operation envelope.

TABLE 3. Exhaust gas properties at the inlet of the HRSG

Gas Turbine Power (kW)	Exhaust gas mass flow rate (kg/s)	Exhaust gas Temperature (oC)	Gas Turbine Efficiency (%)
1000,00	12,00	346,90	18,50
1333,33	13,06	360,80	21,08
1666,67	14,03	374,40	22,97
2000,00	14,80	390,00	24,40
2333,33	15,57	405,40	25,60
2666,67	16,24	419,70	26,63
3000,00	16,80	435,60	27,50
3333,33	17,33	451,10	28,17
3666,67	17,87	465,70	28,84
4000,00	18,30	479,80	29,40

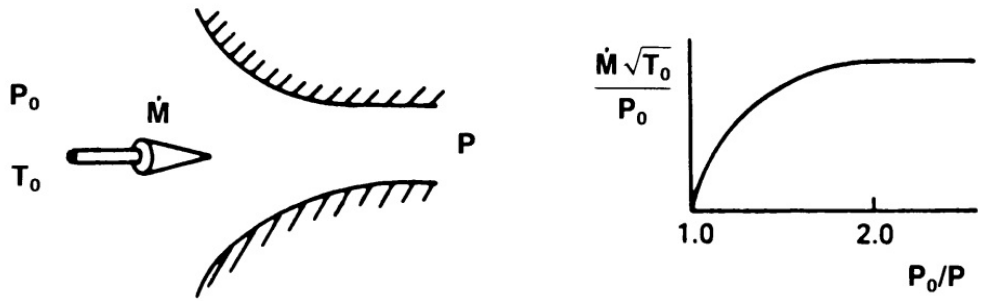

FIGURE 12. Variation of the mass flow rate through a nozzle as a function of the pressure ratio [19]

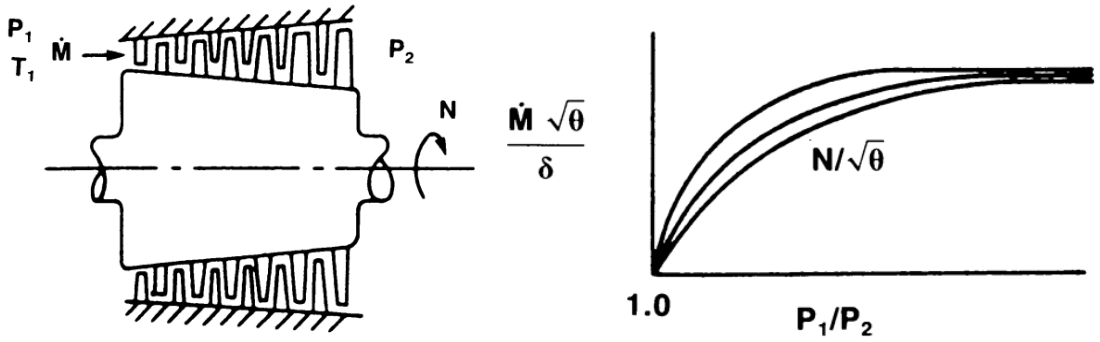

FIGURE 13. Variation of the mass flow rate through a steam turbine as a function of the pressure ratio and the wheel speed N [19].

In this study it has been assumed that the steam turbine used in the Rankine cycle would operate with a similar corrected mass flow as the one used in the reference study [10]. This assumption is required to justify that the predicted values of the steam/water mass flow rates and the pressure ratios are valid and correspond to the ones used in real-life applications.

Results and Discussion

As already mentioned, the purpose of the present work is to investigate in which extend it would be possible to recover the heat from the exhaust gases produced by a gas turbine used for the propulsion (at low and cruising speeds) of a combatant ship of the Hellenic Navy. To this scope the simulated exhaust gas temperatures and mass flow rates are used as input data (Table 3) into the simulation model developed for the Rankine cycle and the potential of heat recovery is examined over the whole operating range of the specific engine (i.e. from 1000 kW to 4000 kW). Following the same computational procedure for each engine load examined, the following parameters are determined:

- Mass flow rate of the Rankine cycle working medium: $\dot{m}_c$
- The saturation pressure of the water / steam in the HRSG: $P_2=P_3=P_4=P_5$
- The temperature of the water / steam at the entrance and exit of the HRSG: T_2 and T_5
- The outlet temperature of the exhaust gas from the HRSG: $T_{h,out}$
- The power produced by the steam turbine: $\dot{W}_{turbine}$
- The power absorbed by the pump which circulates the water/steam: $\dot{W}_p$
- The efficiency of the Rankine cycle defined as:

$$n_{st} = \frac{\dot{W}_{turbine} - \dot{W}_p}{\dot{Q}_{HRSG}} \tag{21}$$

- The overall efficiency of the combined cycle (Gas turbine ./ Rankine Cycle) defined as:

$$n_{CC,real} = \frac{\left(\dot{W}_{turbine} - \dot{W}_p\right) + P_{GT}}{P_{GT} / n_{GT}} \quad (22)$$

where P_{GT} is the power produced by the gas turbine and n_{GT} is the gas turbine efficiency, both given as input to the model developed. It should be noticed that the combined efficiency $n_{CC,real}$ calculated from the equation above differs from the theoretical one n_{CC} as defined in equation (7). This is attributed to the fact that in the definition of the n_{cc} (theoretical efficiency) it has been assumed that all the heat rejected by the gas turbine, is absorbed by the bottoming cycle, which is not the case in real life applications due to the space limitations as far as the HRSG is concerned and the low temperature limit imposed to avoid condensation of the exhaust gas.

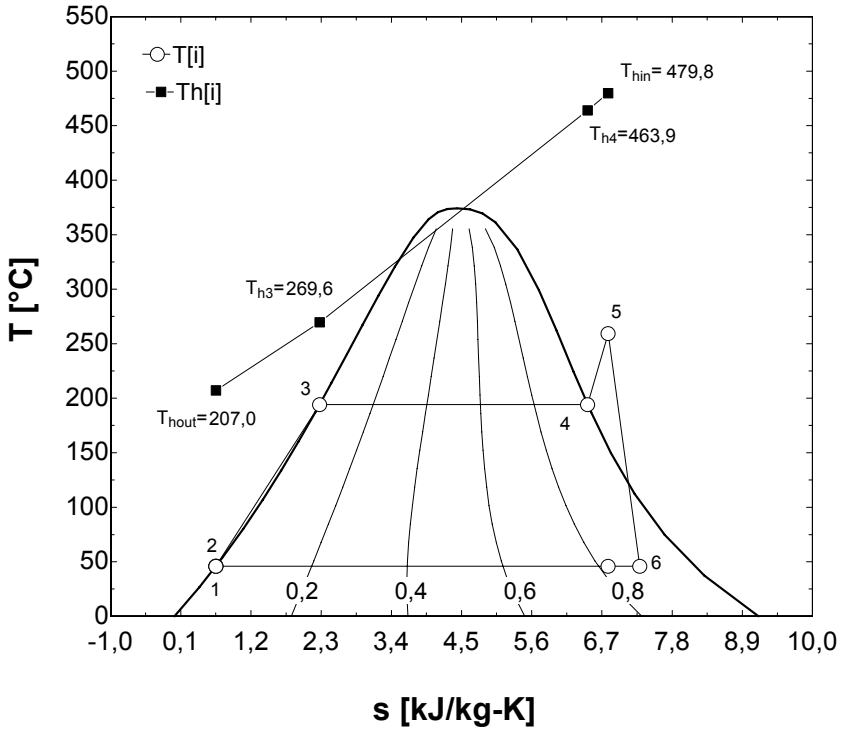

FIGURE 14. T-s process diagram of the Rankine Cycle – Temperature profile of the exhaust gas inside the HRSG, for the case of high gas turbine load (4000 kW)

By solving the above system of equations, the thermodynamic properties of the working medium (steam/water) and the corresponding temperature of the exhaust gas at each stage of the HRSG is estimated, as shown in fig 14. This case corresponds to a gas turbine power equal to 4000 kW (max. engine power). As observed, the main portion of the exhaust gas heat is absorbed in the HRSG to heat up the water (in the economizer) and evaporate it (in the boiler), while a small amount is absorbed for superheating. At the exit of the steam turbine, the steam quality is assumed to be higher than x=0,82, which ensures that the operation of the steam turbine (late stages) is not affected by the condensed steam. In fig. 15 is shown schematically, the corresponding temperature profile of the exhaust gas stream as it passes through the HRSG and the thermodynamic properties of the water/steam following the bottom Rankine cycle, when the gas turbine power is equal to 1000 kW (low load case). In this case it is obvious that the temperature difference between the two fluids (gas and water/steam) in the HRSG is

significantly lower compared with the full engine load case, and the portion of the heat recovered from the exhaust gases which is used for steam superheating is negligible. However, even in these cases the temperature of the exhaust gas at the exit of the HRSG is higher than the limit value which in this study has been set equal to 135 ^{o}C.

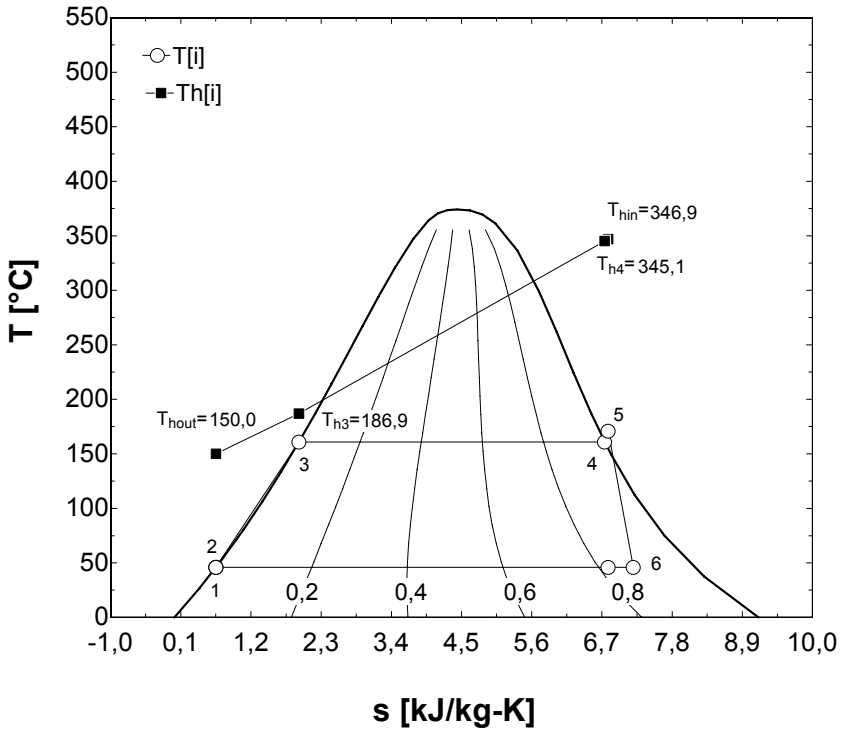

FIGURE 15. T-s process diagram of the Rankine Cycle – Temperature profile of the exhaust gas inside the HRSG, for the case of low gas turbine load (1000 kW)

Effect of Gas Turbine Engine Load on the Combined Cycle Parameters

In fig.16 is shown how the exhaust gas temperature varies as it enters and exits from the HRSG (T_{hin} and T_{hout} respectively). At the same figure, the superheated steam temperature before entering the steam turbine is shown (T_5). It is observed, that as the gas turbine load increases that exhaust gas temperature increases and the corresponding steam temperature increases too. Moreover, the exhaust gas temperature at the exit of the HRSG at all cases examined is kept higher than 135 ^{o}C which is the limit set to avoid gas condensation.

The heat recovered by the exhaust gas is used to raise the temperature and pressure of the working fluid, keeping the flow number of the steam turbine constant. The mass flow rate of the water/steam used as the working medium in the Rankine cycle, together with the saturated steam pressure are shown in fig. 17, as a function of the gas turbine power. It is observed, that both these parameters increase as the gas turbine power increases, as expected, since the available heat in the exhaust gases increases. Moreover, the saturated steam pressure is limited to relative low values (max. 14 bar), which makes the requirements regarding the strength of the materials used for the installation to be moderate. The power produced in the steam turbine also increases as the gas turbine power increases, as shown in fig. 18. At the same figure the power consumed by the circulating pump is plotted and as observed, this is only a small portion of the available steam turbine power (due to the high density of the pumped saturated water).

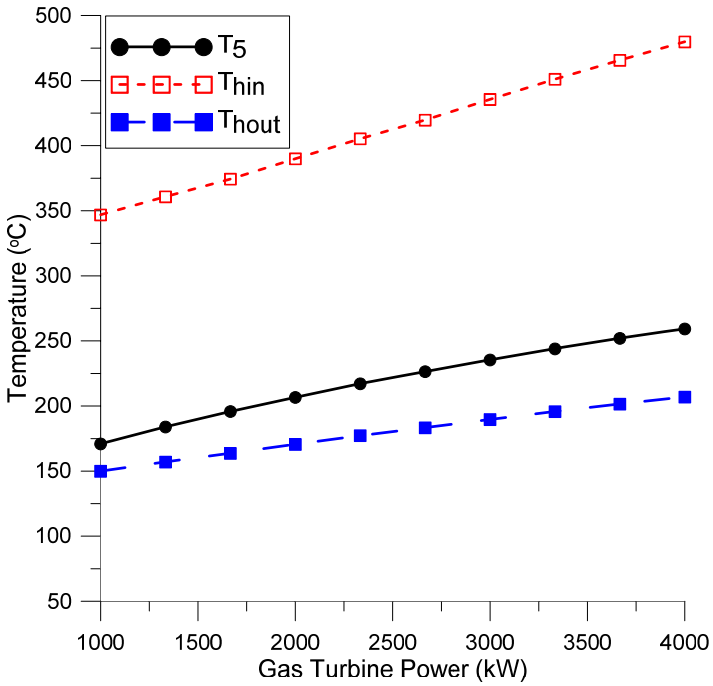

FIGURE 16. Effect of gas turbine power on the exhaust gas temperature before and after the HRSG and on the super-heated steam temperature before the steam turbine (T_5).

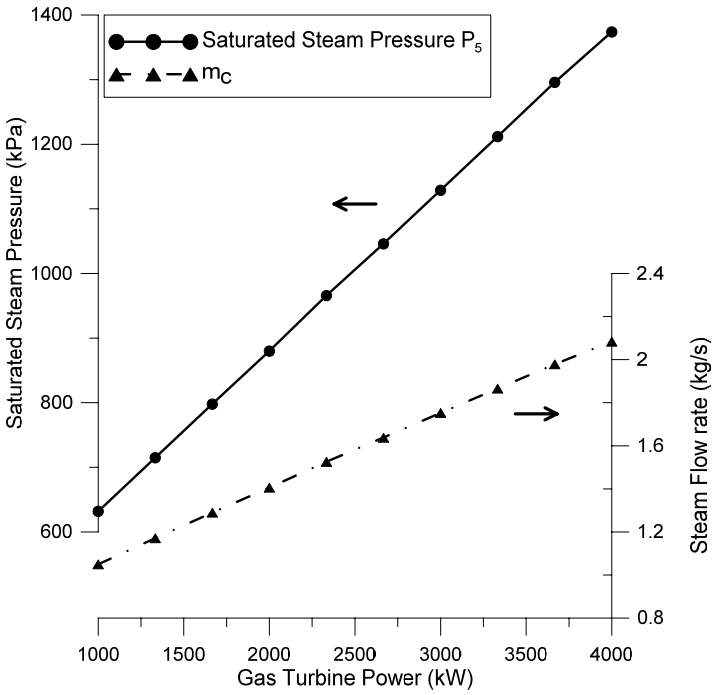

FIGURE 17. Effect of gas turbine power on the saturated steam pressure (P_5) and the steam mass flow rate ($\dot{m}_c$)

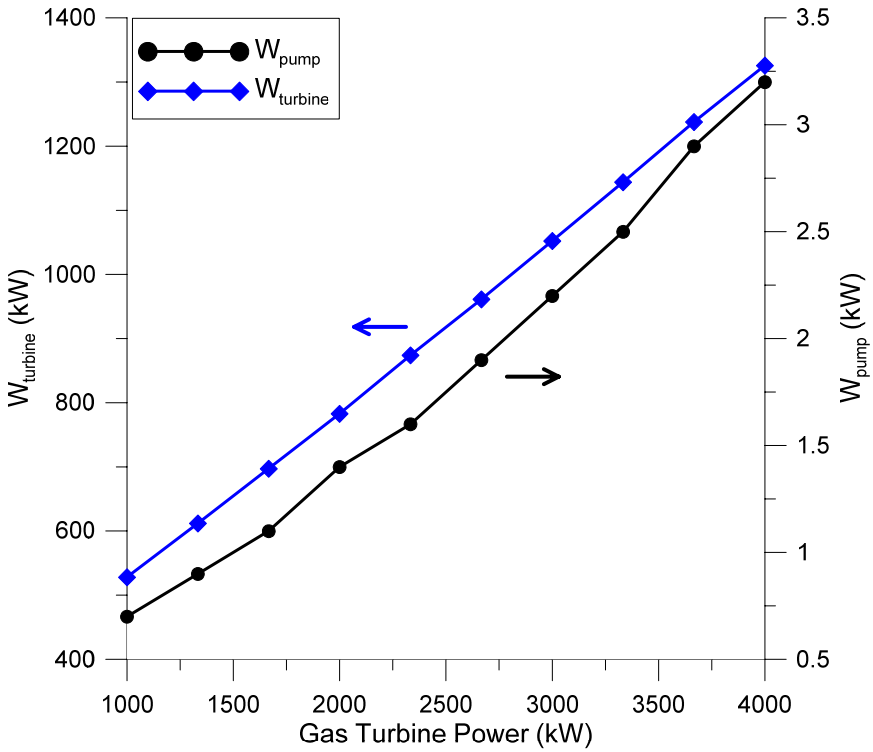

FIGURE 18. Variation of the produced steam turbine power and the circulation pump power demand, as a function of the gas turbine power.

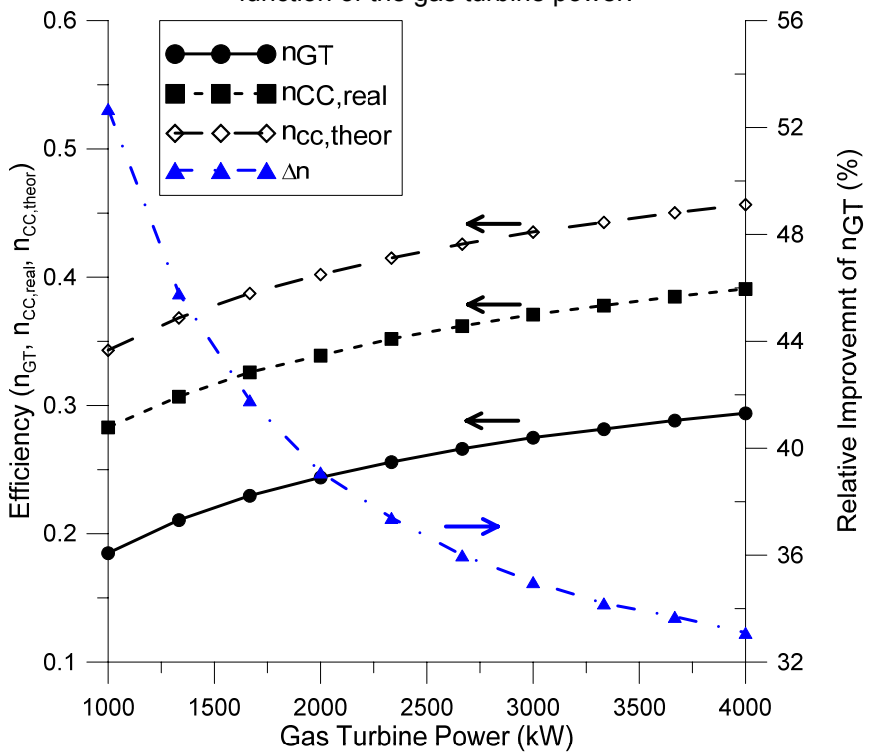

FIGURE 19. Variation of the gas turbine efficiency n_{GT}, the combine cycle efficiency $n_{CC,real}$, the theoretical combined cycle efficiency $n_{CC,theor}$ and the relative improvement of the combined cycle efficiency compared to the simple gas turbine power plant efficiency as a function of the gas turbine power.

In fig. 19 it is shown a comparison between the initial gas turbine efficiency n_{GT} and the one obtained using the proposed combined cycle configuration $_{nCC,real}$ at all the range of operating conditions examined (Gas turbine power from 1000 kW to 4000 kW). As observed, the combined cycle efficiency is significantly higher than the one of the simple gas turbine, ranging from 28%÷39%, while being higher at high engine loads. At the same figure, the theoretical efficiency of the combined cycle $n_{CC,theor}$ is shown, as being calculated using equation (7). It is observed that if there were no restrictions regarding the size of the heat exchangers and the outlet temperature of the exhaust gases, it would be (theoretically) possible to further increase the benefit obtained using the combined cycle, and the combined cycle efficiency could range from 34%÷46%. However, even with the conservative configuration of the combined cycle which has been examined, the relative improvement on the gas turbine thermal efficiency ranges from 53% at low load to 33% at high load (as shown in fig. 19), which is very challenging. It is noticed that the greater improvement is observed at low load conditions where the thermal efficiency of the gas turbine is lower. This is very important for the marine applications since a significant portion of the vessel's duty is spent at low load conditions.

CONLUSIONS

In the present work, a parametric investigation has been conducted, to investigate the possible improvement on the combined cycle efficiency and the corresponding net power production, which can be obtained by adding a bottoming Rankine cycle with a steam turbine on an existing gas turbine engine which is used for propulsion on a combatant vessel of the Hellenic Navy. To this scope a simple model has been developed based on the conservation of energy, for the Rankine cycle simulation and the HRSG. From this preliminary study, it has been concluded that such a combined cycle configuration, could offer significant improvement on the combined cycle engine efficiency, while at the same time, it is accompanied with a significant increase on the net available power and a corresponding decrease on the exhaust gas temperature. These findings are challenging and indicative of the potential benefit (economic and tactical) which could be obtained for the Hellenic Navy by adopting such techniques. However, a more detailed investigation should be conducted, regarding mainly the heat transfer processes at the HRSG and the condenser, to ensure that the required volume and weight of this installation is affordable based on the specific needs of the vessel.

REFERENCES

1. Horlock JH. Combined power plants, including combined cycle gas turbine (CCGT) plants. Malabar, Florida: Krieger Publishing Company; 2002
2.Fredrik Haglind, "A review on the use of gas and steam turbine combined cycles as prime movers for large ships. Part I: Background and design", Energy Conversion and Management 49 (2008) 3458–3467
3. Kehlhofer RH, Warner J, Nielsen H, Bachmann R. Combined-cycle gas and steam turbine power plants. 2nd ed. Tulsa, Oklahoma: PennWell; 1999
4. Merz CA, Pakula TJ. The design and operational characteristics of a combined cycle marine power plant. ASME paper 72-GT-90, 1972
5. Mills RG. Greater ship capability and energy saving with combined-cycle machinery. Nav Eng J 1977;89:17–25
6. MAN B&W Diesel A/S.:Waste Heat Recovery Systems. Copenhagen Denmark, 2007
7. WARTSILA Diesel A/S.:Energy savings and environmental benefits via Exhaust Gas Heat Recovery
8. V. Ganapathy , "Heat-Recovery Steam Generators: Understand the Basics", CHEMICAL ENGINEERING, August 1996
9. Katsanos CO, Hountalas DT, Pariotis EG. Thermodynamic analysis of a Rankine cycle applied on a diesel truck engine using steam and organic medium. Energy Convers Manage 2012;60:68–76.

10. Muench,R. K. ; Knauss,D. T. ; Purnell,J. G., “A study of waste-heat-boiler size and performance of a conceptual marine cogas system”, David W Taylor Naval Ship Research and Development Center Bethesda Md, Feb 1980
11. Fredrik Haglind, “A review on the use of gas and steam turbine combined cycles as prime movers for large ships. Part I: Background and design”, Energy Conversion and Management, Volume 49, Issue 12, December 2008, Pages 3458-3467, ISSN 0196-8904, 10.1016/j.enconman.2008.08.005
12. Roumeliotis I., Mathioudakis K., Aretakis N. “Performance analysis of twin-spool water injected gas turbines using adaptive modeling”, ASME paper No. GT2003-38516.
13. Stamatis A., Kamboukos Ph., Aretakis N., Mathioudakis K., 2002, “On Board Adaptive Models: A General Framework and Implementation Aspects,” ASME Paper No. GT-2002 -30622.
14. Stamatis A., Mathioudakis K., Papailiou D.K., 1990, “Adaptive Simulation of Gas Turbine Performance,” ASME J Eng Gas Turbines Power, 112(2), pp. 168-175
15. Tsalavoutas A., S. Pothos, Mathioudakis K., Stamatis A., 1999, “Monitoring the performance of a twin-spool ship propulsion turbine by means of adaptive modeling,” RTO Symposium on Gas Turbine Operation and Technology for Land, Sea and Air Propulsion and Power Systems, Ottawa, Canada, 18-21 October 1999.
16. Petry, B. R., "Acid Dew-Point Determination for Gas Turbine, Waste Heat Recovery Units," DTNSRDC Report PAS-77-29, Mar 1978
17. Kays, W. M- and A. L. London, “Compact Heat Exchangers”, McGraw-Hill, 1964
18. Petry, B. R., "Acid Dew-Point Determination for Gas Turbine, Waste Heat Recovery Units," DTNSRDC Report PAS-77-29, Mar 1978
19. William G. Steltz , Book chapter “26. STEAM TURBINES”, Mechanical Engineers’ Handbook: Energy and Power, Volume 4, Third Edition, Edited by Myer Kutz, by John Wiley & Sons, Inc

ISSN: 1791-4469 Copyright © 2012 Hellenic Naval Academy

The Design and Development of a Mechanical Faults Simulation Test Rig for Educational Purposes

Doumouras G.[a], Aretakis N.[a], Roumeliotis I.[b], Mathioudakis K.[a]

[a] *Laboratory of Thermal Turbomachines*
National Technical University of Athens, Athens, Greece
[b] *Section of Naval Architecture & Marine Engineering*
Hellenic Naval Academy, Piraeus, Greece

Abstract. The paper describes the process of designing and developing a mechanical faults simulation test rig to support courses on gas turbine diagnostic methods. In this context the test rig is designed to reinforce students understanding in rotor dynamics, instrumentation and measurements analysis, acquiring at the same time experience on mechanical faults symptoms and diagnosis. The design was undertaken by a student, as part of fulfilling the requirements for obtaining a Mechanical Engineering Degree. The design requirements for fulfilling the defined educational objectives are discussed, as are the construction details of the test rig. The instrumentation and the data acquisition system characteristics are also presented, along with sample results of simulated representative faults that have significant value for educational purposes. Finally the benefits accruing from the use of the test rig as part of an educational procedure are discussed, as are the educational benefits for the student that has undertaken the project.

Keywords: Educational experimental apparatus, Vibration measurements, Gas turbine diagnosis
PACS: 0.1.50.My, 46.40.-f

INTRODUCTION

Vibration measurements are a vital part of the gas turbine condition monitoring systems and of the preventive maintenance technique. Vibration level is representative of the engine mechanical condition and each system has a specific healthy vibration range, depending on the manufacturing tolerances. Mechanical faults or engine degradation are usually connected to increased vibration level, thus diagnostic information can be acquired by proper analysis of vibration measurements. According to Boyce [1] vibration analysis coupled with engine performance analysis is an unbeatable tool as a total diagnostic system leading to maximum power plant utilization and significant cost savings.

In order to fully exploit the diagnostic data available in vibration measurements the engineers should have a clear understanding of rotor dynamics, instrumentation characteristics, statistical techniques used in vibration analysis and if possible some hands on experience of the typical faults that occur in rotating turbomachinery components. A method to convey to students the needed knowledge and experience is by using a suitable experimental test rig to support the

theory of vibration analysis and fault identification. Although such test rigs can be found in the market [2], an approach that can be followed is to build such a facility.

The decision of designing and building the test rig was based on a number of benefits that this approach offers. An obvious benefit is that the construction can be tailored made, to suit the educational vision of the teacher and the courses objectives. This approach also allows the cost to be kept well below the market price of similar commercial test rigs. The main drive however is the fact that the design and development process can itself contribute to the education. The first aspect is that the student responsible for the design of the test rig is involved on an integrated project that deals with many disciplined of his studies, while at the same time it provides the satisfaction of seeing something calculated and drawn on “paper” to be actually materialized. A second very important aspect is that having the outcome of a student project on display and usage to future generations give them confidence on their knowledge and motivate them to pursue similar integrated projects. Based on this reasoning the work was offered as a student diploma project and materialized by a final year student in cooperation with the Laboratory of Thermal Turbomachines of National Technical University of Athens (LTT/NTUA) staff [3].

The present paper describes the design and development of the test rig, which is capable to simulate mechanical failures that occur in turbomachines, in a controlled environment and is fitted with typical instrumentation found in the field. The instrumentation and the data acquisition system characteristics are presented, along with sample results of simulated representative faults that have significant value for educational purposes. Finally the benefits accruing from the use of the test rig as part of an educational procedure are discussed, as are the educational benefits for the student that has undertaken the project.

DESIGN OF THE TEST RIG

Malfunctions in turbomachines are categorized both by their causes and their effects in operation. Two of the most common and most frequently appeared malfunctions in turbomachines are unbalance and misalignment.

Unbalance is a situation in which some asymmetry exists in the geometry of a rotating part of a machine with respect to the axis of rotation which has the result that the axis of inertia of the rotating part is different from its axis of rotation. There are four different types of unbalance, as seen in Figure 1.

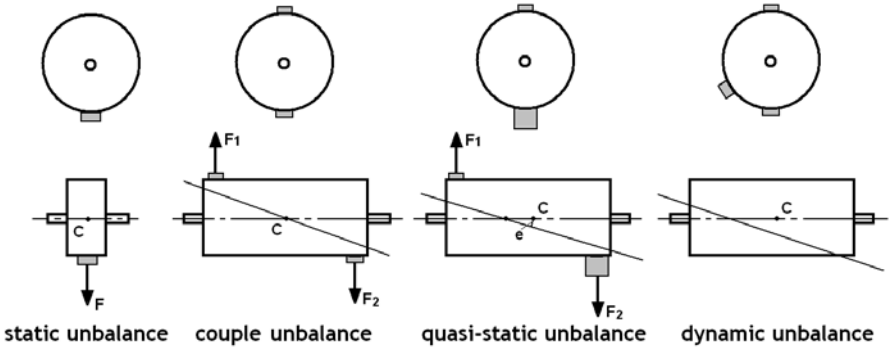

FIGURE 3. Types of Unbalance

Static unbalance appears when the centre of gravity lies off the rotation axis, while the axis of inertia is parallel to the axis of rotation. In this case the vibrations of both shaft ends will be in phase. Couple unbalance is defined as the condition of unbalance where the inertia axis crosses the axis of rotation on the gravity centre. Even though the shaft is statically balanced, it tends to vibrate about its center when it is rotated, while the vibrations of the shaft ends are in

opposite phase (180 deg difference). Quasi-static unbalance is made up of a static unbalance and a couple unbalance. Quasi-static unbalance is the condition of unbalance where the inertia axis crosses the axis of rotation at a point different from gravity centre. The vibrations of shaft ends have unequal amplitudes but in phase. The fourth type of unbalance is dynamic unbalance and it is the most common type encountered in machinery. Dynamic unbalance is defined as unbalance where the axis of inertia and the axis of rotation do not intersect and they are not parallel. Dynamic unbalance often exhibits different amplitudes of vibration at each end of the shaft. In addition most often it exhibits phase angles that are neither in phase nor directly opposite from one another. Couple unbalance, quasi-static unbalance and dynamic unbalance cannot be corrected in a single plane but require corrections to be made in two or more planes.

Misalignment in couplings can appear in three basic types, as seen in Figure 2. The first is a parallel offset. In this type of misalignment, the two shafts can be offset vertically, horizontally or in a combination of both. The second type is angular misalignment. In this type of alignment, the angularity again can be in the vertical plane, the horizontal plane or in both planes. In most cases misalignment in couplings occur as a combination of both types.

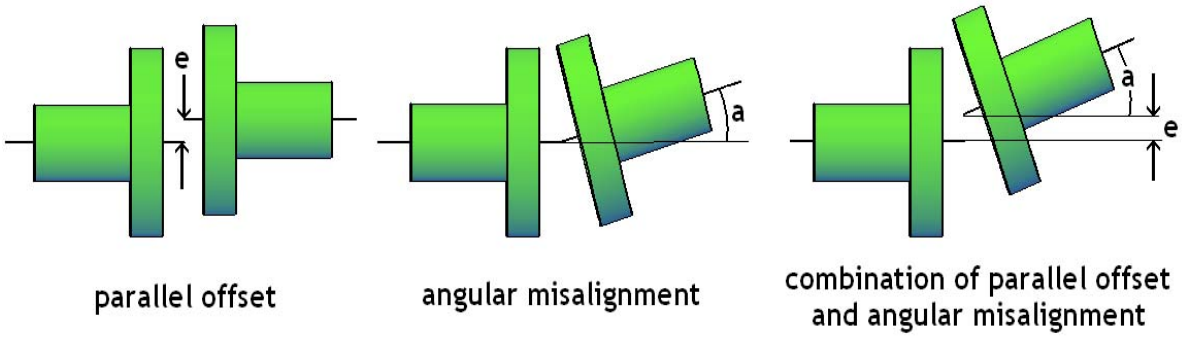

FIGURE 4. Types of Misalignment

Since misalignment and unbalance are the most common faults encountered in practice it was decided to design the test rig in order to simulate these two faults. An unbalanced shaft can easily be simulated by placing additional masses to specific positions to a properly balanced shaft. In order to simulate misalignment a coupling is needed in order to have the ability to move the shaft relative to the coupling. According to these rough guidelines the test rig should consist of a shaft with drilled holes at specific positions (unbalance), two bearing houses for the shaft, a motor, a suitable coupling, and a mechanism that will allow the movement of the shaft ends relative to the coupling (misalignment).

The test rig is tailored for supporting courses on gas turbine diagnosis, thus the shaft selected should be relevant to the topic, but also of relatively small dimensions.

Concerning the needed measurements the vibrations, in the form of velocity, or acceleration should be measured at the bearing positions. The use of proximity sensors could be problematic since the sensor must be close to the shaft, thus it wouldn't be possible to simulate cases of extreme misalignment without risking the probe integrity. Also rotational speed should be measured with good accuracy in order to characterize vibration frequency components.

Finally in order to increase the impact and the interactivity of the laboratory exercise, the results, in the form of faults signatures should be promptly available to the students. For this purpose a program that can analyze the vibration measurements in real time and produce power spectra in a graphical environment should be used.

DEVELOPMENT OF THE TEST RIG

The main part of the test rig is the rotating shaft. As discussed it should be relevant to the topic of turbomachinery. A small turbocharger shaft including the compressor and the turbine is ideal for this purpose, since it contains the turbomachinery components, giving a “real life” experience to the students. The selected shaft, which is a small turbocharger shaft, can be seen in Figure 3. The turbine rotor consists of 50 vanes and the compressor rotor consists of 20 blades. The total length of the shaft is 486 mm and its total weight is 6.9kg.

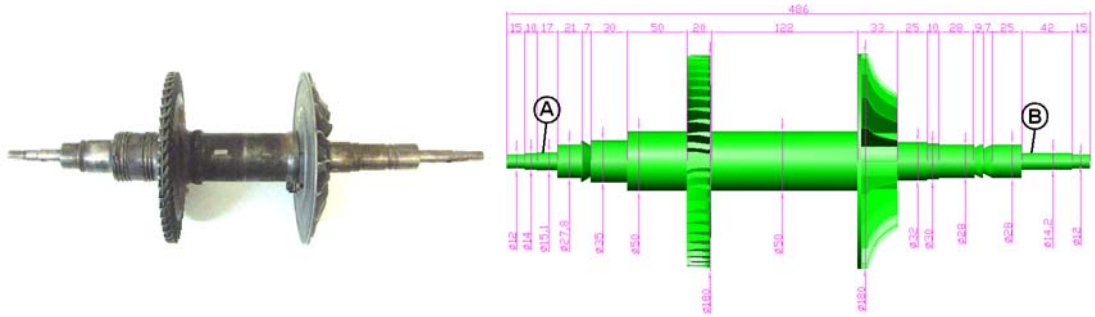

FIGURE 3. The selected shaft, its dimensions and seating positions (A, B)

The shaft was decided to be seated at two points (points A and B, Figure 3). The bearings used are deep groove ball bearings with an inner diameter of 15mm. The bearings can accept strong radial forces but can also accept axial forces. For their adaption to the shaft a ring was used.

In order to have the ability to balance the shaft, but also to simulate unbalance the addition or removal of masses from specific places around the rotating axis should be possible. In order to achieve this holes are drilled at the turbine and the compressor planes. At each plane 8 holes are drilled. Their radial position is 53.75mm for the turbine plane and 46mm for the compressor plane. The angle between two holes is constant and equal to 45 degrees for both planes. Added masses are small screws of different length.

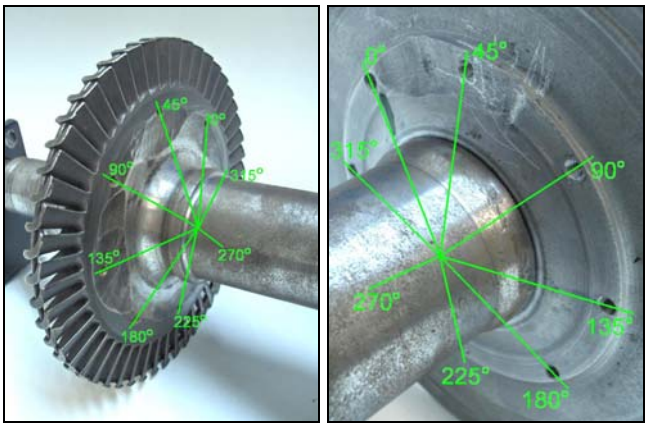

FIGURE 4. Places for balancing masses at turbine and compressor plane

In order to simulate misalignment the two shaft seatings should be capable of vertical movement. An appropriate mechanism identical for the two seatings has been constructed and can be seen in Figure 5. The main seating part is L shaped (item 1) which is also part of the

bearing house. Side to side holes have been drilled in order to allow the pins (items 2) to slide inside item 1. Item 1 is risen by a screw rod (item 3). A clockwise turn of the rod results to the tightening of item 1 to the seating assembly. A counterclockwise turn of the rod results to the vertical rise of item 1. Since both shaft ends should be capable of vertical movement for the purpose of misalignment simulation the coupling of the shaft to the motor couldn't be a commercial one. This is due to the fact that commercial couplings use elastic rings in order to minimize misalignment effects. A non elastic coupling was designed and constructed. The coupling consists of two separate parts, one fitted to the shaft and one fitted to the motor. The electromotor shaft and the rotating shaft have been properly formed in order to make possible the conjunction of coupling parts to them with screws. Conjunction of coupling parts to each other uses M6 screws placed in side to side drilled Ø6 holes (6 holes drilled symmetrically to rotating axis). The constructed coupling can be seen in Figure 6.

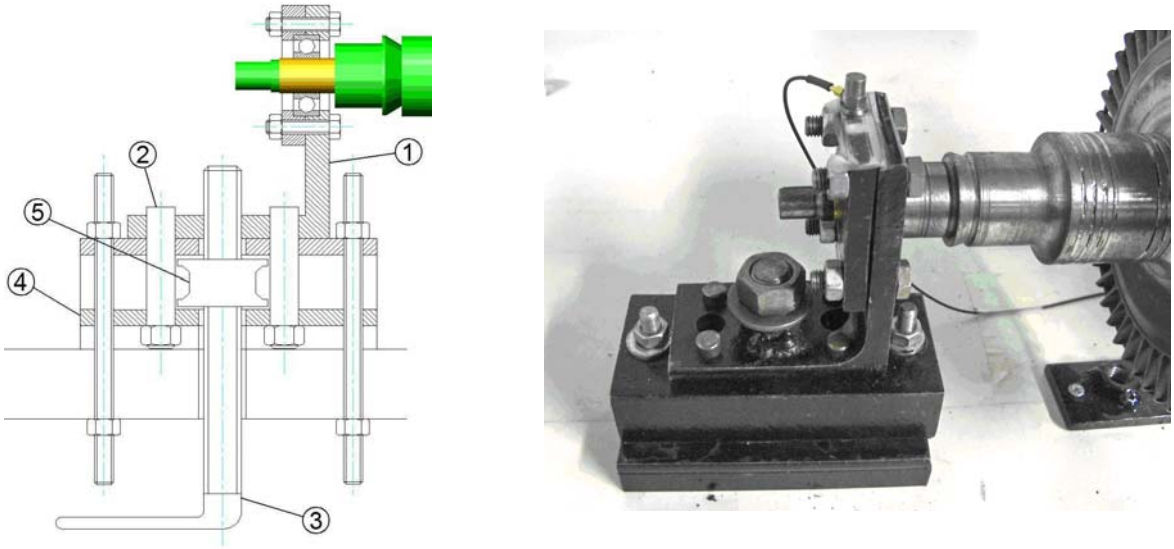

FIGURE 5. The seating assembly

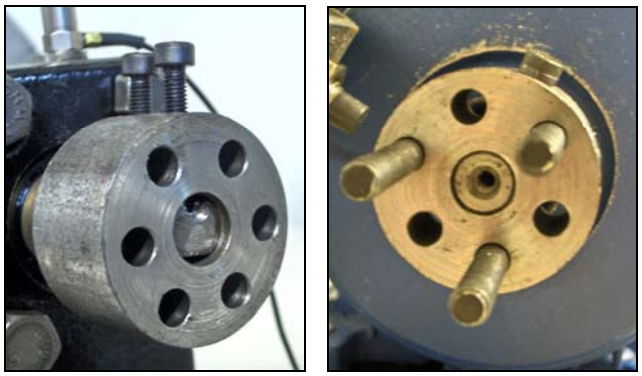

FIGURE 6. Coupling parts

The motor selected is a 3-phase induction electromotor. The electromotor has a rated power value of 0.18kW, it is connected with a 220V supply power, and the value of the field current is 0.9A with a frequency of 50Hz. Power factor value is cosφ=0.8. The rated speed is 2890rpm and the slide value is about s=5%. The electromotor is driven by an inverter, allowing the control of the shaft's angular velocity. The inverter has a frequency width of 5 to 50 Hz. An inductive

sensor is used for the angular velocity measurement and is placed close to the coupling as seen Figure 7. The sensor signal is led to a frequency voltage converter and the angular velocity is presented in a LED display either in rpm or Hz units.

FIGURE 7. Coupling and inductive sensor

In order to measure vibration level, two accelerometers are used, one for each bearing. The accelerometer placed at A position (Figure 3) measures the vibrations for the turbine plane and the accelerometer placed at B position measures the vibrations for the compressor plane. Each accelerometer is mounted on top of the bearing housing using an appropriate magnetic disk, while it is insulated in order to prevent the current's frequency value to pass through the accelerometers and to the vibration signals. Accelerometers' sensitivity is 0.313 pC/ms^{-2}. Each accelerometer is connected with a charge amplifier. The amplifier use low-pass filters in order to cut off high frequencies and consequently to avoid "aliasing" frequencies appearance during the signal processing. Upper and lower frequency cut off limits, as well as the accelerometers' sensitivities are the basic amplifier parameters and can easily be determined by the operator via switches at amplifier's front side. Signal output uses a BNC port at amplifier's back side.

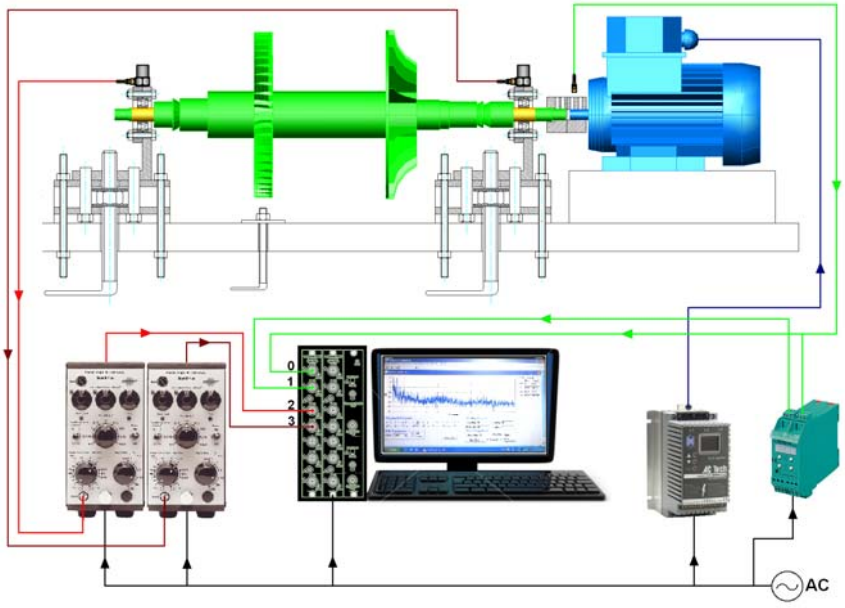

FIGURE 8. Test Rig Measuring Chain and Signals flow diagram

Measurements signals are led to the processing unit. The unit consists of a laptop, equipped with a data acquisition card having maximum total sampling frequency of 500 kHz and 12-bit accuracy. BNC ports are used as the card's interface with the signals. The signals acquired and analyzed are the angular velocity, inductive sensor pulse signal and the amplified vibration signals of the two accelerometers. The data processing is materialized using in-house software, which allows the analysis of acquired vibration signals using Fast Fourier Transformation (FFT) while the results in the form of power spectra and of power spectra differences from a reference condition are presented through a graphic interface environment. The parameters of the measurements analysis, such as the number of samples for FFT are set by the user, as is the range, gain and slope values for each channel. The measuring chain and the flow diagram of the measurements are presented in Figure 8.

Rotating parts of the test rig can be dangerous both for the operator and the students. So it was decided to place a plexiglas-made cover over the rotating parts. The cover is properly designed to allow the observation of the rotating shaft during operation, while a switch guarantees that the test rig wouldn't operate when the hood is open. The cover consists of an aluminum frame which upholds three 5mm plexiglas sheets. The finished test rig can be seen in Figure 9.

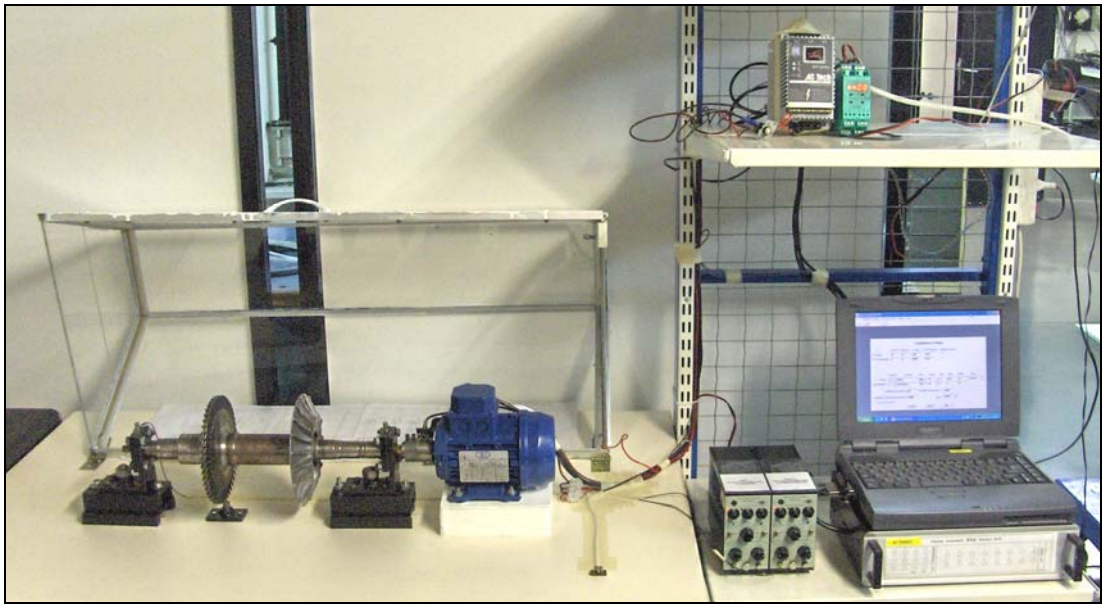

FIGURE 9. The test rig

PROCEDURE AND RESULTS OF THE LABORATORY EXERCISE

A typical laboratory exercise routine, along with sample results is presented in order to verify that the test rig operates as expected and to highlight some of the educational objectives that can be accomplished. The primary objective of the laboratory exercise is for the students to understand the basic principles of diagnosis and to acquire knowledge and experience on the instrumentation, the measuring chain needed to perform vibration measurements and the analysis needed in order to gain diagnostic information. Also the importance of faults signatures should be clear, as should be the actual pattern of the simulated faults signatures. At the same time the students should understand the concept of balancing and its importance.

Prior to starting the laboratory exercise the measuring chain is presented and analyzed, while elements of rotor dynamics theory and vibration measurements, already covered during lectures, are discussed. Following, the “healthy” power spectra at the two planes (compressor and turbine) for a specific rotational speed are established. These power spectra are set as the reference condition in order to calculate power spectra differences when the faults will be implanted. This step highlights the basic principle of diagnosis: “A change on the condition of a mechanical system changes the physical quantities and parameters that describe the system’s operation. Measuring the physical quantities change relative to their reference (healthy) values can lead to the finding of the root causes of the system’s condition change”. During the data acquisition the adjustments of the amplifier are examined, the students can directly see the effect of changing the settings to the power spectra and understand the logic and experience behind the selected setting.

Having established the reference power spectra, the next step is the simulation of unbalance. Prior to fault simulation the teacher discusses with the students elements of rotor dynamics theory and describes mechanical and turbomachinery components faults that may result to unbalance. Such kinds of faults are fouling or erode during operation, foreign object damage and thermal effects, shaft sag, and rotor stator rubs [4].

Following the theoretical discussion, unbalance of the turbine and of the compressor is simulated. Firstly a mass of 24 gr is added at the compressor plane, at the position of 135^{o} counterclockwise and the power spectra difference from the reference ones for the two accelerometers are acquired. The power spectra differences, as seen in the GUI of the data acquisition program are presented in Figure 10.

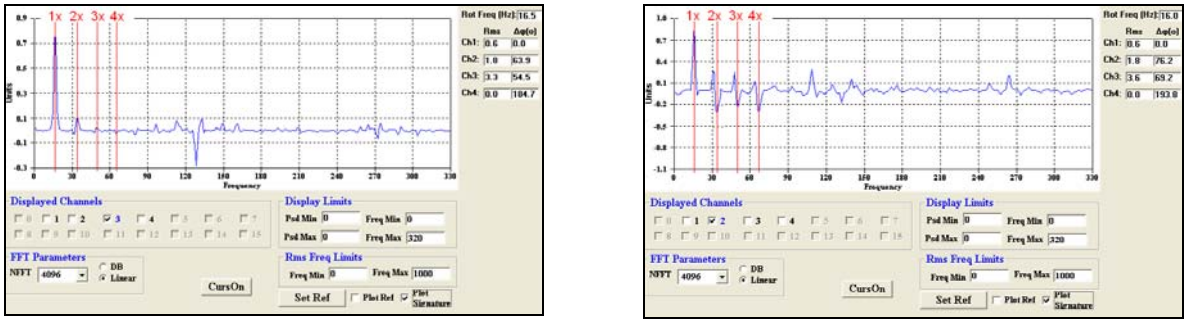

(a) (b)

FIGURE 10. Power spectra differences (fault signature) for compressor unbalance calculated from (a) the compressor plane accelerometer and (b) the turbine plane accelerometer

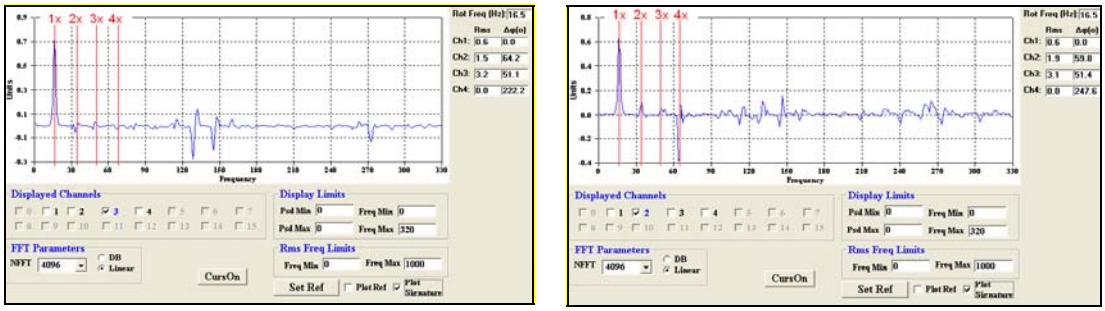

(a) (b)

FIGURE 11. Power spectra differences (fault signature) for turbine unbalance calculated from (a) the compressor plane accelerometer and (b) the turbine plane accelerometer

The same routine (addition of a 24 gr mass at the position of 135^{o} counterclockwise) is repeated for simulating turbine unbalance and the corresponding power spectra differences are acquired (Figure 11).

From the results presented it is evident that the expected signature of unbalance is produced by the test rig. Specifically according to the literature [1,5] unbalance produce an increase of the vibration level at 1x of the shaft rotational speed frequency. In this way the students verify the theoretical knowledge through observation.

The test rig is stopped and the simulation of misalignment starts. Using the test rig as an example the teacher discuss about real word cases of misalignment and the operational problems that may arise such as excessive vibrations which will trip the engine and bearing failures. Also the most probable causes for misalignment such as improper mounting and expansion of the gear housing in case of power production gas turbines [1] are discussed, along with the parameters that define the misalignment tolerance, such as coupling length and type of bearings.

In order to simulate misalignment the shaft end connected to the motor via the coupling is moved vertically via the seating's mechanism described. The power spectra and the faults signatures are acquired and promptly analyzed. The results can be seen in Figure 12.

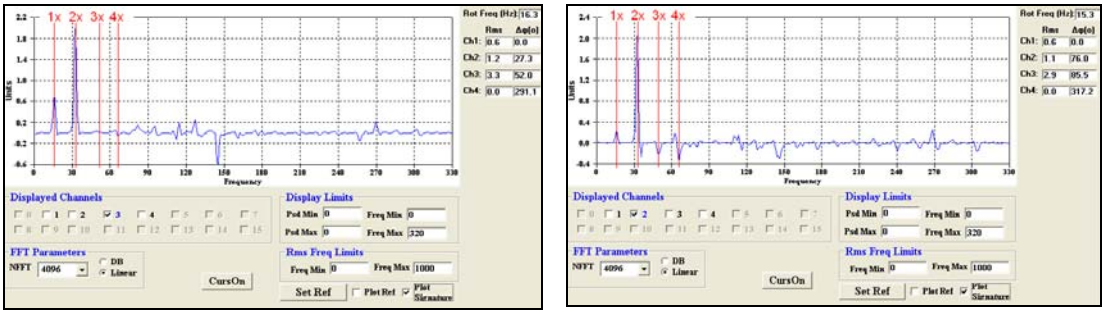

(a) (b)

FIGURE 12. Power spectra differences (fault signature) for misalignment calculated from (a) the compressor plane accelerometer and (b) the turbine plane accelerometer

From the results presented it is evident that the expected signature of misalignment is produced by the test rig. Specifically according to the literature [1,5] misalignment produce an increase of the vibration level at 2x of the shaft rotational speed frequency. In this way the students verify the theoretical knowledge through observation.

In order to further increase the insight of the students, homework is assigned based on the measurements taken during the unbalance simulation. The objective of the homework is to find the balancing masses and their radial position that should to be added at the compressor and turbine plane in order to balance the shaft. The method that has to be implemented is the standard two-plane influence coefficient method [6].

EDUCATIONAL ASPECTS

The test rig developed during a diploma thesis by an Engineering student is currently used for supporting courses on gas turbine diagnostic methods. In this context it has educational value for both the student that designed and constructed the test rig and for the students that use it.

As a laboratory exercise, as discussed above, it teaches in an experiential way the basic principle of diagnosis. It enhances the understanding of concepts, such as vibration level, power spectrum and faults signature, which are of paramount importance for applying diagnostic

methods. At the same time the students learn how to set up a measuring chain for monitoring vibrations of a rotating system and they use the knowledge gained to answer to a real life problem (shaft balancing). Another important aspect of the exercise is the verification of the theoretical knowledge through observation in real time and in a controllable environment.

Concerning the student that designed and participated in the construction of the test rig, the procedure has several educational aspects. Execution of a project of this type requires the continual avocation with the subject and the student works within the Laboratory facilities cooperating with technicians and with the supervisor, thus emulating real working environment conditions. The student worked in the workshop and used the lab infrastructure, including tools, materials, electronic equipment and instrumentation, thus gaining experience in many engineering disciplines. The student was encouraged to take initiatives for solving the engineering problems that arose during the project, while he was responsible for contacting vendors and manufacturers, gaining experience to the field of project planning and enhancing his decision making abilities.

The fact that the test rig has been developed by a diploma thesis project has its unique merit in the educational process. Specifically it gives students confidence for their knowledge and motivate them to pursuit similar multidisciplinary projects, as for example the building of a contra-rotating compressor facility that has been assigned to two students the years following this project and was concluded by them [7,8] .

SUMMARY

The process for designing and setting up a mechanical fault simulation test rig has been described. The design process has been described, starting with the initial requirements and going through specific choices for the final layout. The way choices were made was presented, on the basis of serving in the best way the educational purpose that the test rig is mainly destined for. The test procedure and sample results have been presented, verifying the successful operation of the test rig and confirming the effectiveness of the design choices. The education aspects and expected benefits, for either students involved projects for setting up an installation, or students using the test rig as a support to the diagnostic related courses were highlighted.

REFERENCES

1. M. P. Boyce, “Gas Turbine Engineering Handbook”, Gulf Professional Publishing, 3rd edition, ISBN 0-88415-732-6, (2006)
2. Kasarda M., “A Rotating Machinery Course at Virginia Tech Developed with Industry Support”, ASME paper GT-2002-30154, (2006)
3. Doumouras G., “Modal Testing for Vibration Diagnosis and Development of a Mechanical Faults Simulation Test Rig”, NTUA, Diploma Thesis (2007)
4. Norfield D., “Practical Balancing of Rotating Machinery”, Elsevier, ISBN 10: 1-85-617465-4, (2006)
5. Girdhar P., Scheffer C., “Practical Machinery Vibration Analysis and Predictive Maintenance”, Elsevier, ISBN: 978-0-7506-6275-8, (2004)
6. Dimarogonas, A., “Vibration for Engineers”. Prentice Hall, ISBN 978-0134562292, (1996)
7. Katsikis G., “Design and Development of a Test Rig for Counter-Rotating Blade Rows”, NTUA, Diploma Thesis (2008)
8. Ampatis C., “Components Design and Construction, First operation and Measurements on Counter Rotating Blade Rows Test Rig”, NTUA, Diploma Thesis (2010)

ISSN: 1791-4469 Copyright © 2012 Hellenic Naval Academy

Forensic engineering methodology to assess the Maintenance, Repair and Overhaul (MRO) procedures for Gas Generator Turbine Cooling Plates

D.G.Karalis[a] and N.E.Melanitis[a]

[a]*Hellenic Navy, Hellenic Naval Academy, Mechanics & Materials Division, Marine Materials Laboratory, Hazjikyriakou Avenue, Piraeus 185 39, Greece*

Abstract. Investigation was carried out on a set of cooling plates obtained from a gas generator turbine (GGT). The need for the assessment of the durability and remaining operational life of the gas generator turbine component was identified, following a recommendation by the manufacturer for the early replacement of the cooling plates. The current study applied a forensic engineering and failure analysis methodology to assess the Maintenance, Repair and Overhaul (MRO) procedures of high reliability components. From the results of the current investigation it was finally deduced that, in spite the fact that the plates seemed to be macroscopically in good condition, certain metallurgical observations sustained the claim for early component replacement.

Keywords: Gas generator turbine, cooling plate, coated nickel superalloy, failure analysis, forensic engineering methodology.

INTRODUCTION

A set of eight cooling plates from a gas generator turbine were delivered to the Marine Materials Laboratory following a recommendation by the manufacturer for earlier replacement due to changes to the specifications. The eight cooling plates were obtained from an engine that is depicted schematically in figure 1.

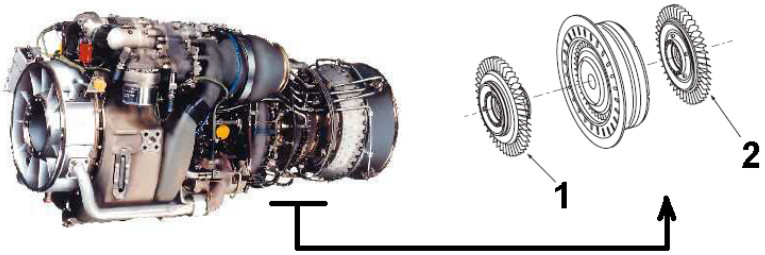

FIGURE 1. General view of the engine (left) and part of the gas generator turbine (right).

The engine consists of the compressor (cold section), the gas generator turbine (hot section) and the power turbine (power turbine section). The gas generator turbine contains the stage 1 gas generator turbine rotor (item 1 in figure 1), the stage 2 gas generator turbine rotor (item 2 in figure 1) and the gas generator stator (shown between the items 1 and 2 in figure 1). The gas

generator turbine rotors are bolted to the compression section of the engine and as the exhaust gases turn the gas generator turbine rotor, the compressor also turns. This makes the system self-sustaining. The gas turbine and the compressor rotate at 44700 RPM whereas the power turbine rotates at 20900 RPM. The items 1 and 2 that are presented in figure 1 consist of the cooling plates, the disk and the blades. These are depicted in large scale in figure 2.

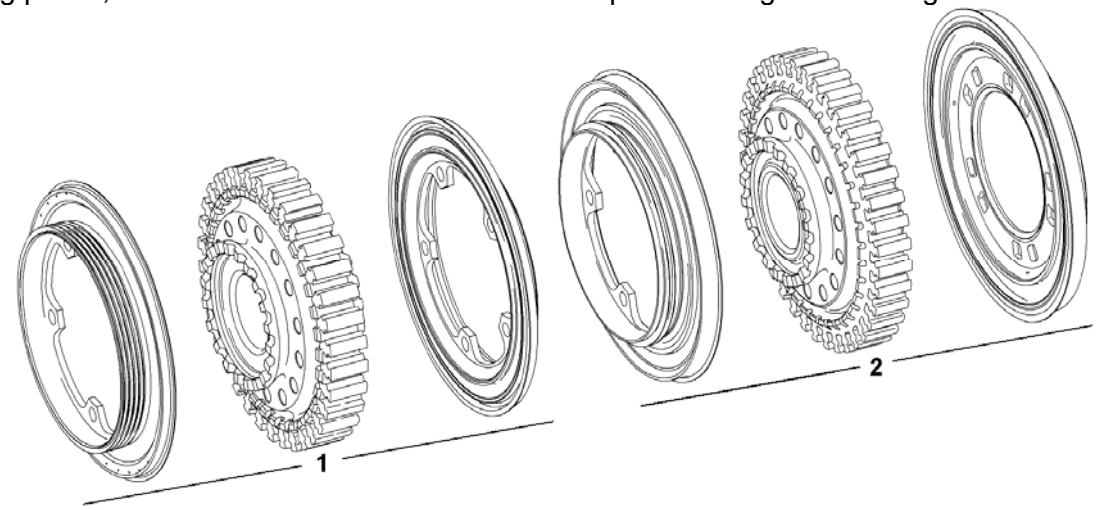

FIGURE 2. Gas generator turbine rotor parts. From left to right: stage 1 forward cooling plate, stage 1 disk (blades not shown), stage 1 aft cooling plate, stage 2 forward cooling plate, stage 2 disk (blades not shown), stage 2 aft cooling plate.

As seen from figure 2, these thin machined cooling plates are mounted on both sides of each disc in order to constrain cooling air to follow the most effective path. The plates consist of a short cylindrical body of 20 mm height and a circular flange of 148 mm diameter. The stage 1 forward cooling plate contains continuous circumferential projections along the short cylindrical body similar to a thread. The full stage 1 gas generator turbine is depicted in figure 3 (item 1 in figure 1).

FIGURE 3. The gas generator turbine rotor with the blades positioned around the rotor disk. The cooling plates are fixed with five bolts on the rotor disk. Notice the sand-color of the blades.

The aim of the current paper is to investigate whether the manufacturer recommendation for early replacement of the cooling plates was an apt advice. This will be carried out by investigating the potential existence of wear, cracking or any other evidence of structural degradation of the plates. Thus the validity of the manufacturer recommendation will be assessed and the owner of the gas generator will be consulted accordingly. In addition to the above the current study seeks to establish a set of failure analysis tools and criteria as an assessment methodology for the usability of non-failed critical engine components.

EXPERIMENTAL PROCEDURE

Macroscopic investigation was realized optically, by naked eye and by using a SSM stereomicroscope. **Microstructural analysis** was realized in mounted cross-sections of the material obtained from the flange of the disk. Manual grinding was performed using MetaServ grinding devices and successive abrasive papers up to #2400 grid followed by fine polishing using diamond and silica suspensions. Cleaning was performed using ethanol followed by hot air stream drying. Etching was performed using 7.5 mL HF, 2.5 mL HNO_3, 200 mL CH_3OH etchant. Etching time was 5 minutes. **Metallographic observation** was carried out using an AusJena metallurgical microscope. **Hardness testing** was performed employing a calibrated Indentec Rockwell A Hardness tester applying 60 kg of force. **Fractographic observation** was conducted to cleaned specimens employing a JEOL Scanning Electron Microscope. Locations for optical and electronic observation were also assisted by **Finite Element Analysis** results. Energy Dispersive X-ray Spectroscopy was used for **local chemical analysis** whereas X-ray Fluorescence was employed for **global chemical analysis** of the coating using Seiko SII, SEA 1200 VX analyzers. **Non-destructive fluorescent penetrant inspection** (Type I, Method B, Level 4) was also carried out on the cooling plates.

INVESTIGATION

Data Relevant to Cooling Plates History

The engine manufacturer recommendation for early replacement of the cooling plates was provided on the basis of advanced life-estimation numerical models results that have been recently developed by the manufacturer, as a part of its Maintenance, Repair and Overhaul (MRO) procedures. It is well understood that any premature replacement strongly influences the overall cost of the engine maintenance, whereas disregarding of the recommendation may influence the reliability of the rotor parts, the safety of the engine and crew.

Macroscopic observation

All delivered plates were in visually good condition, a fact that made the manufacturer recommendation to look excessive. Macroscopic observation carried out by naked eye on the delivered eight cooling plates did not reveal any signs of global plastic deformation or permanent global distortion. The three most strained plates (with respect to total hours in operation) had some sand deposited on their surface which is attributed to the coastal environment where the specific gas generator was operating (see the color of the whole set in

figure 3). After cleaning of the specimens it was revealed that they were deposited with a protective coating. As depicted in figure 4, in four out of the eight plates, the protective coating was worn (lost) or fractured exposing the substrate of the plate to the surrounding combustion gasses.

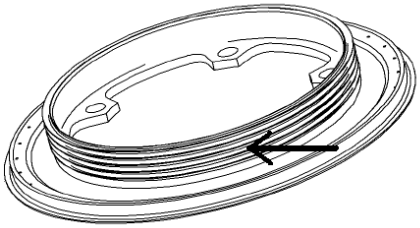

(a)

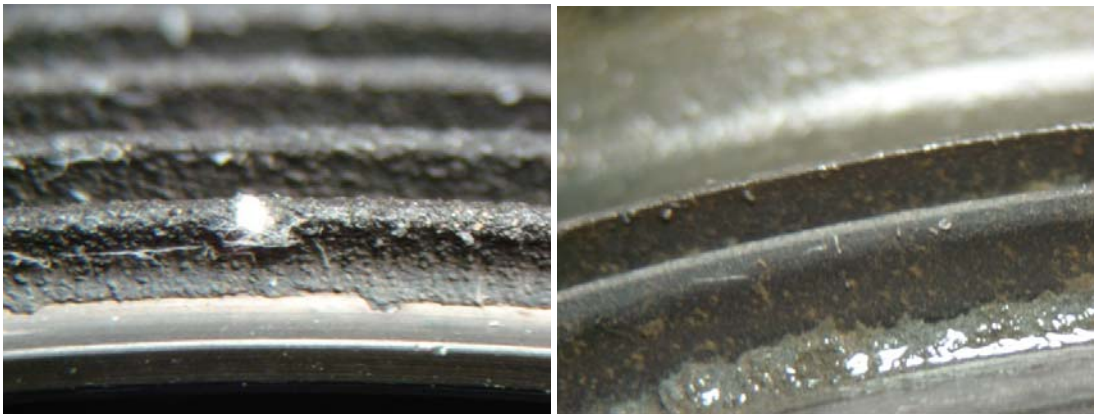

(b) (c)

(d) (e)

FIGURE 4. (a) Observation of the thread. (b)-(d) Existence of worn coating (lost) in three different plates. (e) In one plate the coating has been fractured.

Fracture and local plastic deformation of a structural element contained in one cooling plate was also identified as depicted in figure 5. Further detailed observation of the surface of the eight plates did not reveal any cracked areas. The latter was also confirmed by the non-destructive fluorescent penetrant inspection.

SEM Microfractography, SEM/EDS and XRF analysis

In order to further examine the plates for potential cracks and wear, Scanning Electron Microscopy was used. For this reason specimens from the most strained plate (stage 1 forward cooling plate) were prepared. Chemical analysis of a cross section of the flange (coating excluded) using SEM/EDS presented the chemical composition shown in table 1 and figure 6b.

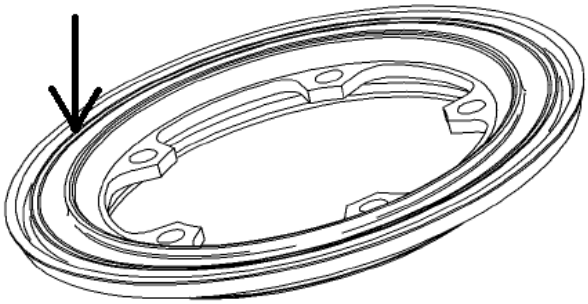

(a)

(b)

(c)

FIGURE 5. (a) Observation of the flange of one plate. (b) Fractured structural element. (c) Plastically deformed structural element.

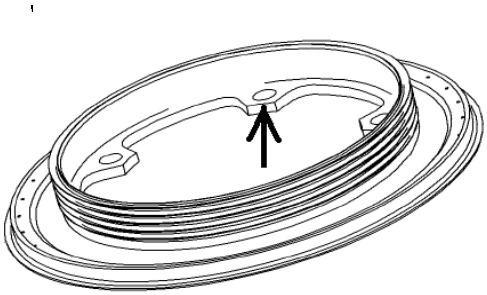

(a)

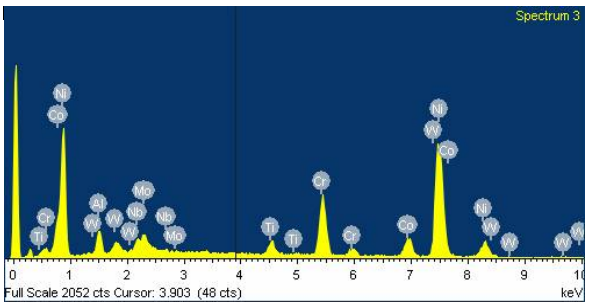

(b)

FIGURE 6. (a) Specimen location for the SEM/EDS chemical analysis. (b) Results of SEM/EDS chemical analysis

TABLE 1. Chemical composition of a cross section of the flange (coating excluded)

Element	Al	Ti	Cr	Co	Ni	Nb	Mo	W

%w/w	4	3	13.5	7.5	bal	5.9	4	4

Detailed examination of the specimens revealed the existence of worn surfaces on the plate's coating. More specifically, three different zones of non-uniform wear of the coating were identified on the flange of the plate as shown in figure 7.

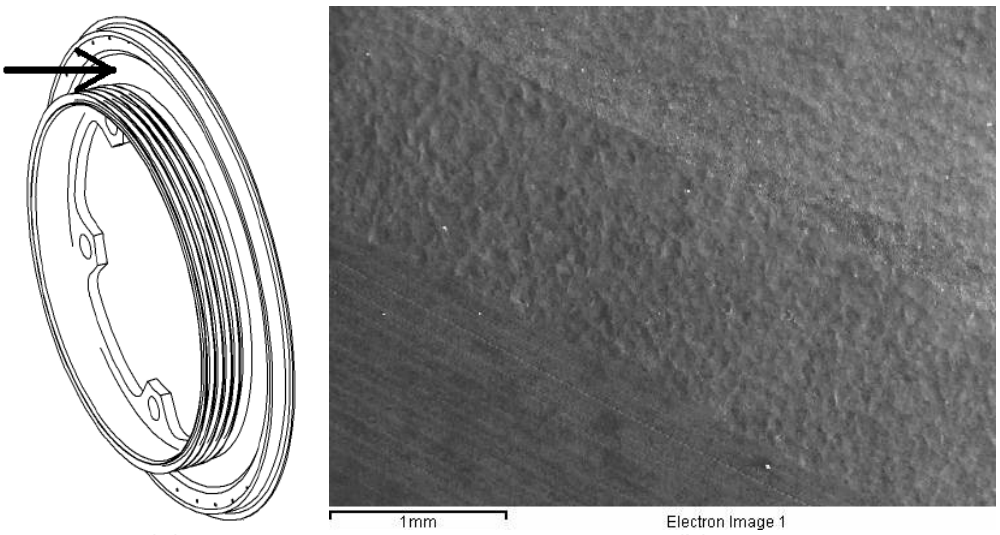

(a) (b)

FIGURE 7. (a) Observation of the flange. (b) Existence of three different zones of non-uniform wear of the coating.

Qualitative local chemical analysis of the worn coated surface using both SEM/EDS and XRF revealed the existence of the elements shown in Table 1 plus some small amounts of Fe as shown in figure 8.

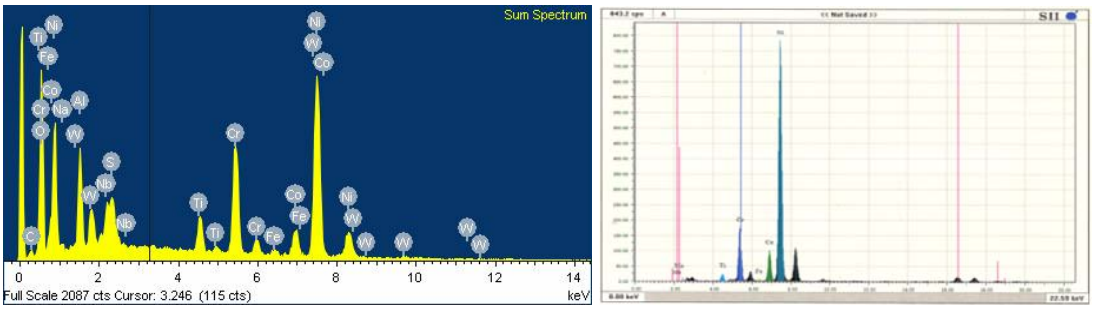

FIGURE 8. Local qualitative chemical analysis of worn coating (a) SEM/EDS results. (b) XRF results

Non uniform wear and extensive cracking was identified on the thread of the plate. More specifically, at the bottom of the thread, which is less exposed to the gasses, good coherence between the coating's matrix and the reinforcing grains was identified. Furthermore no signs of wear or cracking were existent on the coated surface. On the other hand, at the tip of the thread that is more exposed to the surrounding environment, extensive cracking, erosive wear and grain removal from the coating's matrix were identified. The results are depicted in figure 9.

The SEM/EDS chemical analysis results of the coating at the worn tip of the thread are presented in Table 2 and figure 10. No cracking was identified at any other location of the plate.

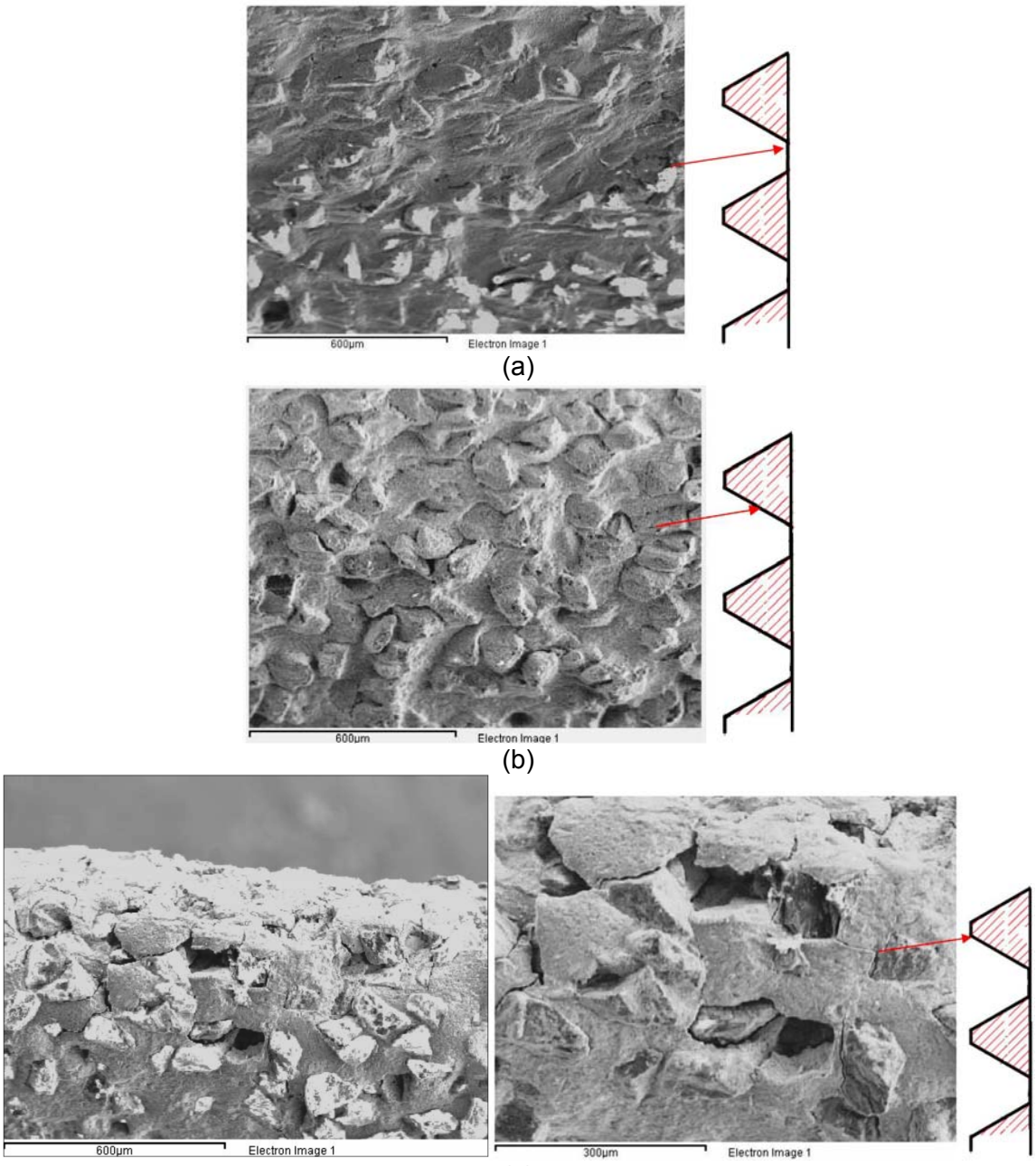

FIGURE 9. (a) Almost intact coating at the bottom of the thread. (b) The intermediate area of the thread presenting erosive wear, partial cracking and partial grain removal. (c) Tip of the thread presenting extensive cracking, erosive wear and grain removal from the coating's matrix.

TABLE 2. Chemical composition of the worn coating at the tip of the thread

Element	Al	W	Si	Fe	Ni
%w/w	11	7	23	2	bal

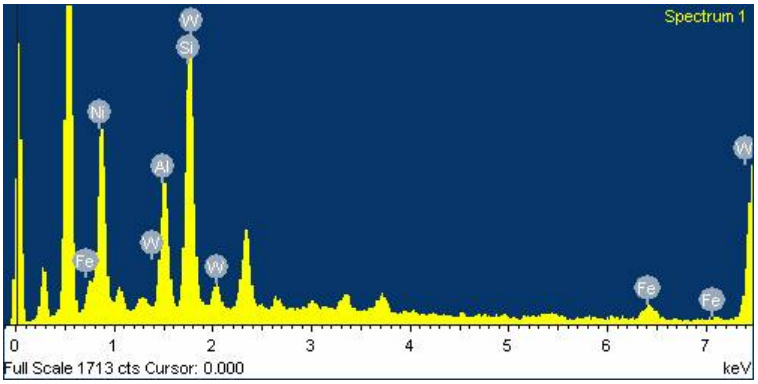

FIGURE 10. Local chemical analysis results by SEM/EDS of the worn coating at the tip of the thread

Microstructural Analysis

Specimens for microstructural analysis were prepared from a cross section of the thread of the plate in order to investigate whether the identified cracks of the coating (depicted in figure 9) have penetrated the substrate material. The investigation did not identify any cracks propagating through the substrate nickel superalloy. Strongly eroded coating and removal of the reinforcing grains from the coating's matrix were identified. The maximum thickness of the coating was measured equal to 110 μm whereas the minimum thickness was 20 μm at some locations. The analysis also revealed that the microstructure of the nickel matrix contained resolved precipitates. No blocky carbides were identified. The hardness of the plate was measured equal to 73 HRA (450 HV). The microstructural analysis results are depicted in figure 11.

Calculations and Finite Element Analysis

In order to identify the critical locations with respect to maximum stress a three dimensional linear thermo-mechanical finite element model of the most strained plate (stage 1 forward cooling plate) was set up using ALGOR® commercial code. The model contained in total 3163 flat shells (plates) and beam elements that were used to model the thread. The model was assigned with the mechanical properties of a typical Ni annealed alloy (density 8.22 gr/cm^3, modulus of elasticity 207 GPa, Poisson ratio 0.31, thermal coefficient of expansion 13.1x10^{-6} K^{-1} and shear modulus of elasticity 76 GPa). Coating, gas pressure, friction, rabbet loads, bolt clamp loads and manufacturing process were not included in the analysis. The nodes of the model at the holes of the flange where fixation with the disk takes place were totally fixed. The stress free reference temperature of the model was set equal to 298 K (25 ^{o}C). Two different load cases were analyzed. In load case 1 (LC1), the centrifugal loads due to rotation at nominal speed of 44700 RPM were taken into account whereas thermal strains were totally ignored. In load case 2 (LC2), the uniform temperature of the plate was set equal +100 K above the stress free reference temperature in order to let the thermal strains develop on the model, whereas the centrifugal loads were not accounted for in the analysis. The results of the FE analysis are shown in figure 12. The common 10-color contour legend refers to maximum and minimum displacement or stress: the maximum displacement of the legend refers to 0.2 mm whereas the minimum to 0 mm. The maximum stress of the legend refers to 1158 MPa whereas the minimum to -1158 MPa.

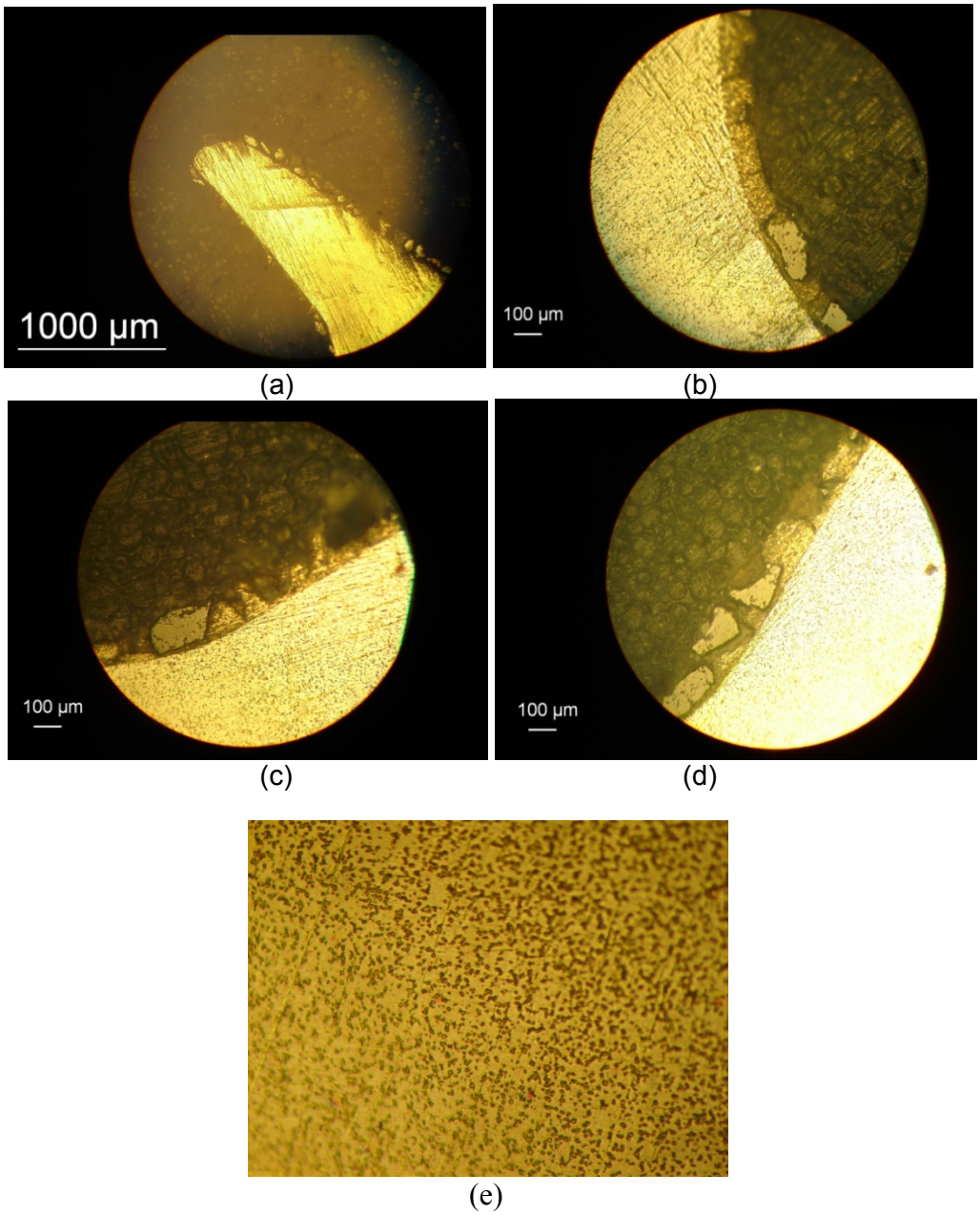

FIGURE 11. (a) Part of the thread with the worn coating. (b) Almost intact coating. (c)-(d) Coating showing grain removal and erosive wear. No cracks penetrating the substrate material were identified. (e) Microstructure of the substrate containing resolved precipitates (x250).

Here it has to be emphasized, that in real world the forward cooling plate, the rotor disk and the aft cooling plate although being fixed together, are allowed to expand due to temperature increase at bigger degree compared to the case simulated previously (total fixation); thus the thermal stress results presented in figure 12 represent a conservative solution. From the FEA results it is deduced that the critical sites for optical observation are located at the vicinity of holes of the flange where the fixations with the bolts exist, at the intersection of the flange and the thread and the thread as well. Notice, that the FEA results presented herein provide only a

global indication of some of the critical areas with respect to failure and are presented as supplementary information to the laboratory investigation results.

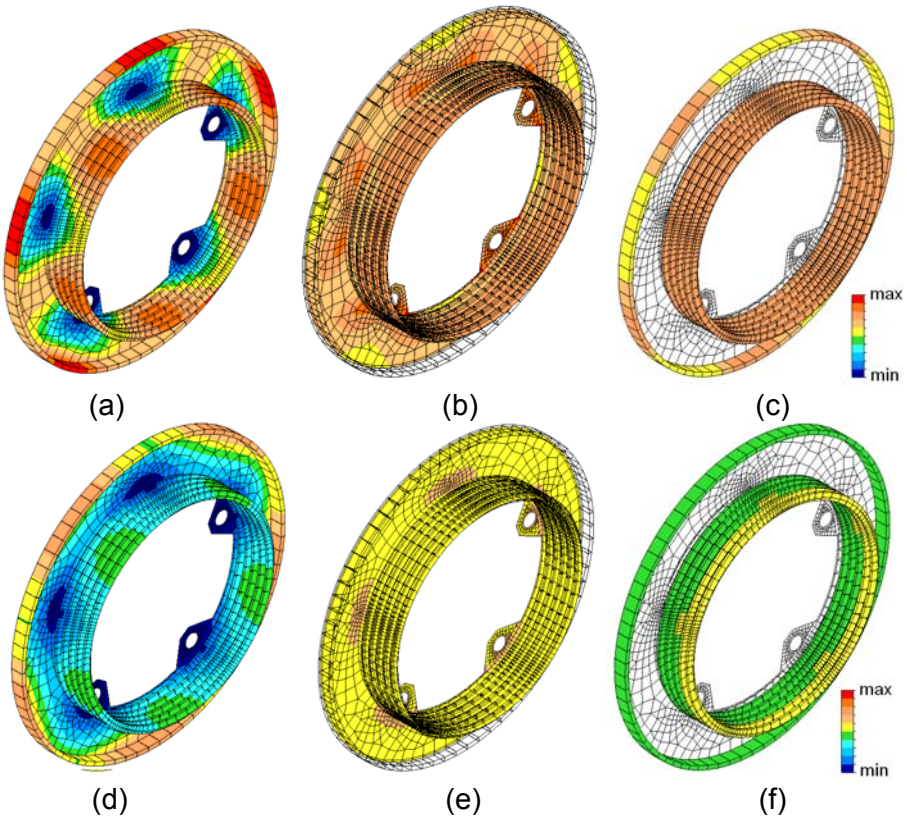

FIGURE 12. (a) LC1: Magnitude of displacements due to rotation. (b) LC1: Von Mises centrifugal stress on flat shells. (c) LC1: Worst centrifugal stress on beams. (d) LC2: Magnitude of displacements due to temperature increase. (e) LC2: Von Mises thermal stress on flat shells. (f) LC1: Worst thermal stress on beams.

DISCUSSION, CONCLUSION AND RECOMMENDED ACTIONS

From the findings of the current investigation the following are deduced:

a. The plates are made from a coated high strength nickel superalloy [1, 2].
b. The microstructure of the nickel matrix contained resolved precipitates.
a. On the coating of the plates, nickel as long as aluminum, tungsten, silicon and iron were detected.
b. Four out of eight plates exhibited worn coating at the thread (eroded or lost coating).
c. One out of eight plates presented fractured coating at the thread (coating loss).
d. One out of eight plates exhibited local plastic deformation and fracture of its structural elements.
e. None of the eight cooling plates presented any cracking in macro scale that could be identified by naked eye or by using a typical laboratory stereo-microscope.
f. Nondestructive testing did not reveal the existence of any crack in macro scale in any of the plates.

g. Localized observation at all locations of the most strained plate using Scanning Electron Microscopy did not reveal any micro crack propagating through the substrate material of the plates.
h. The most strained plate (stage 1 forward cooling plate) presented non-uniform wear of the coating on its flange. The latter is probably attributed to the contact with the joining machinery (see also figure 1). Erosive wear of its coating at the thread was identified. Extensive cracking of the eroded coating and coating loss was also observed.
i. Microstructural analysis from a sample of the most strained plate (stage 1 forward cooling plate) confirmed the existence of severely worn, eroded, cracked and lost coating but did not identify any cracks penetrating through the substrate material. The thickness decrease of the coating at some areas was equal to 80%.

Nickel alloys are used for a wide variety of applications, the majority of which are designed to take advantage of the corrosion resistance and/or heat resistance properties of these alloys. Nickel superalloys are used in turbine compressor blades and discs, shafts, spacers, fasteners, miscellaneous jet engine hardware; space shuttle turbo pump seals, afterburner components, combustion chamber liners, nozzles, vanes, rings, turbine exhaust weldments, structural parts, etc [1, 2, 3]. Nickel is a versatile element and will alloy with most metals. Complete solid solubility exists between nickel and copper; wide solubility ranges between iron, chromium, and nickel make possible many alloy combinations. The face centered cubic structure of the nickel matrix (γ) can be strengthened by solid-solution hardening, carbide precipitation, or precipitation hardening. Cobalt, chromium, molybdenum, tungsten, titanium, and aluminum are all solid-solution hardeners in nickel. Aluminum, titanium and niobium are strong γ'-Ni_3(Al,Ti) and γ"-N_3Nb precipitate formers, which when present in a high nickel matrix provide significant strengthening of the material. Tungsten, titanium, niobium, molybdenum and chromium act as carbide formers. Aluminum and chromium provide oxidation resistance [1-3]. Because high temperature failures normally initiate at the grain-boundary interfaces, it is a common practice to reduce the grain boundary interfaces or completely eliminate them [4].

The temperature at the entrance of the turbine can be considerably high. Therefore to keep the structural parts from degradation, both complex cooling schemes and coatings are often used. High temperature coatings are designed to increase the life of the underlying alloy during service. In general, nickel-based alloy coatings show good high-temperature wear and corrosion resistance. They have good wear resistance after adding tungsten and molybdenum elements to the alloy. Nickel based coatings are used in applications when wear resistance combined with oxidation or hot corrosion resistance is required [5-13]. Two generic coating types are used for similar applications: diffusion coatings and overlay coatings. Both types of coatings result in a surface layer enriched in oxide-forming elements to promote formation of a protective oxide layer. In general, the use of protective coatings can greatly increase the lives of nickel base superalloys for operating conditions in which the oxidation or hot corrosion resistance of the base material is unacceptable. However, the protective coatings themselves are subject to degradation under engine operating conditions and thus have limited lives. Degradation of the protective coating can affect the integrity of the substrate material leading to its failure [4-13].

From the results presented above it is finally deduced that the protective coating of the plates was degraded, eroded and lost in several areas, exposing the substrate material to the aggressive gas environment. It is thus concluded that, in spite of the fact that the plates seemed to be macroscopically in good condition, the identified wear may substantially contribute to onset of failure, as literature indicates [1,4-13].

The test protocol that was applied in current expert report has included Macroscopic investigation in combination with Non-destructive Inspection for identification of global distortion or defects, Microstructural analysis combined with Metallographic observation, Hardness testing and global Chemical Analysis for material characterization, Fractographic observation and local Chemical Analysis for identification of fractographic mechanisms realized in micro scale and finally Finite Element Analysis for better understanding of operational response. The results of the aforementioned tests and analyses that have been often employed in failure analyses can be used in order to assess the maintenance, repair and overhaul procedure of high reliability components.

ACKNOWLEDGMENTS

The authors would like to thank the military and civil personnel of the Telecommunication and Electronics Media Factory of the Hellenic Military Aviation for their help in conduction of the nondestructive testing and SEM/EDS analysis. Authors also acknowledge that current work was made possible by the assistance of the military personnel of the Hellenic Helicopter Naval Base.

REFERENCES

1. ASM handbook, Vol. 5, Surface Engineering; 1994.
2. ASM handbook, Vol. 2, Properties and Selection: Nonferrous Alloys and Special-Purpose Materials; 1990.
3. ASM handbook, Vol. 9, Metallography and Microstructures; 2004.
4. ASM handbook, Vol. 11, Failure Analysis and Prevention; 2002.
5. T.S. Sidhu, S. Prakash, R. D. Agrawal, Hot corrosion and performance of nickel-based coatings, Current Science 90 (2006) 41-47.
6. R. Sivakumar, B.L. Mordike, High temperature coatings for gas turbine blades: A review, Surface and Coatings Technology 37 (1989) 139-160.
7. AS. Osyka, AI. Rybnikov, S.A Leontiev, N.V. Nikitin, I.S. Malashenko, Experience with metal/ceramic coating in stationary gas turbines, Surface and Coatings Technology 76-77 (1995) 86-94.
8. G.W. Goward, Progress in coatings for gas turbine airfoils, Surface and Coatings Technology 108–109 (1998) 73–79.
9. N. Eliaz, G. Shemesh, R.M. Latanison, Hot corrosion in gas turbine components, Engineering Failure Analysis 9 (2002) 31-43.
10. M.J. Pomeroy, Coatings for gas turbine materials and long term stability issues, Materials and Design 26 (2005) 223–231.
11. I. Gurrappa, A. Sambasiva Rao, Thermal barrier coatings for enhanced efficiency of gas turbine engines, Surface & Coatings Technology 201 (2006) 3016–3029.
12. R. Rajendran, M.D. Ganeshachar, Jivankumar, T. Mohana Rao, Condition assessment of gas turbine blades and coatings, Engineering Failure Analysis 18 (2011) 2104–2110.
13. R. Rajendran, Gas turbine coatings – An overview, Engineering Failure Analysis 26 (2012) 355–369.